ESTCP 199902

Demo #2 GPR UXO Classification Results for The Blossom Point Site

Final Report

Matthew .B. Higgins[1], Chi-Chih Chen1, and Kevin O'Neill[2]

[1]Ohio State University, Electroscience Laboratory
1320 Kinnear Rd., Columbus, OH 43212

[2]US Army Corps of Engineers
Engineer Research and Development Center (ERDC/ CRREL)
72 Lyme Rd, Hanover, NH 03755

August 2005

Report Documentation Page		*Form Approved* *OMB No. 0704-0188*

Public reporting burden for the collection of information is estimated to average 1 hour per response, including the time for reviewing instructions, searching existing data sources, gathering and maintaining the data needed, and completing and reviewing the collection of information. Send comments regarding this burden estimate or any other aspect of this collection of information, including suggestions for reducing this burden, to Washington Headquarters Services, Directorate for Information Operations and Reports, 1215 Jefferson Davis Highway, Suite 1204, Arlington VA 22202-4302. Respondents should be aware that notwithstanding any other provision of law, no person shall be subject to a penalty for failing to comply with a collection of information if it does not display a currently valid OMB control number.

1. REPORT DATE **AUG 2005**	2. REPORT TYPE	3. DATES COVERED **00-00-2005 to 00-00-2005**
4. TITLE AND SUBTITLE **Demo #2 GPR UXO Classification Results for The Blossom Point Site**		5a. CONTRACT NUMBER
		5b. GRANT NUMBER
		5c. PROGRAM ELEMENT NUMBER
6. AUTHOR(S)		5d. PROJECT NUMBER
		5e. TASK NUMBER
		5f. WORK UNIT NUMBER
7. PERFORMING ORGANIZATION NAME(S) AND ADDRESS(ES) **Ohio State University,Electroscience Laboratory,1320 Kinnear Rd,Columbus,OH,43212**		8. PERFORMING ORGANIZATION REPORT NUMBER
9. SPONSORING/MONITORING AGENCY NAME(S) AND ADDRESS(ES)		10. SPONSOR/MONITOR'S ACRONYM(S)
		11. SPONSOR/MONITOR'S REPORT NUMBER(S)

12. DISTRIBUTION/AVAILABILITY STATEMENT
Approved for public release; distribution unlimited

13. SUPPLEMENTARY NOTES

14. ABSTRACT

15. SUBJECT TERMS

16. SECURITY CLASSIFICATION OF:			17. LIMITATION OF ABSTRACT	18. NUMBER OF PAGES	19a. NAME OF RESPONSIBLE PERSON
a. REPORT **unclassified**	b. ABSTRACT **unclassified**	c. THIS PAGE **unclassified**	**Same as Report (SAR)**	**122**	

Standard Form 298 (Rev. 8-98)
Prescribed by ANSI Std Z39-18

Table of Contents

List of Figures

List of Tables

Chapter 1   Introduction

An ultra-wide bandwidth, full-polarimetric ground penetrating radar (GPR) system operating from 10 MHz to 810 MHz has been applied to the classification of unexploded ordnance (UXO). Late-time radar signatures such as natural resonance and polarization were utilized to separate false alarm objects from UXO-like items with elongated bodies with length-to-diameter ratios greater than three. Additional features such as length, depth and orientation were also extracted from the data. Good classification performance was obtained from the previous Tyndall Test [1] for UXO-like items with inclination angles less than 45 degrees [2], where inclination is measured relative to the approximately horizontal ground surface. That particular test utilized only features extracted from a single radar position, approximately directly above the target. It was later found that this single-position approach contributed to many false alarms and the incapability of classifying UXO's with large inclination angles, such as vertical UXO's. Subsequently, new measurement approaches and additional radar features were developed to reduce the false alarm rate and missed-UXO's.

A second field test ("Demo #2), conducted at the Blossom Point UXO Site [3,4], is the subject of this report. An improved system configuration and measurement approach was used to collect GPR data at multiple positions by moving the antenna along a straight line centered at the target spot. Other than 14 known targets, there were 78 blind target positions marked, where either UXO's or clutter items had been emplaced without the test team knowing the target identities. Multiple passes were performed along different orientations through each target position. The new approach provides spatial distributions of scattering response, including both early-time behavior as well as late-time UXO signatures. The combination of these features improves the classification of UXO's with large inclination angles due to the additional oblique observation angle with respect to the target. False alarm items caused by offset shallow objects can now be discriminated using the additional time-position scattering characteristics. Overall, the current improved approach should increase the success rate of UXO classification and

decrease the false alarm rate. The new approach also eliminates the problem of position uncertainty along the scan direction because it inherently samples over a structured variety of positions and measurement pass orientations.

This report summarizes the new processing and classification algorithm, and presents the classification results for all the targets measured at the Blossom Point site.

1.1 Radar System Description

The same radar system used in the Tyndall Demonstration was used again at the Blossom Point site except that the new frequency range was from 10 MHz to 410 MHz at 2 MHz increments. Notice that the upper frequency and the increment have been changed from 810 MHz and 1 MHz, respectively, used in the earlier Demo. This is because the Blossom Point soil was quite wet, with high dielectric constant. Such conditions render the higher frequencies useless because they are absorbed by the moist soil; further, under these conditions the resonance phenomena of greatest interest appear in a lower frequency range. The larger frequency increments were used to speed up data collection. The radar includes a commercial RF vector network analyzer (HP8712ET) using a dielectric loaded horn-fed bow-tie (HFB) antenna. It is set up for collecting both co-polarized and cross polarized returns. Relative to the previously used configuration, the antenna orientation was rotated 45 degrees such that the two dipole-elements are parallel and transverse to the direction of scan as shown in Figure 1. The co-polarized returns are S_{11} (transmission and reflection polarization along the vehicle path), S_{22} (polarization perpendicular to the vehicle path), and S_{12} and S_{21} are the two cross-polarizations. Assuming that the target positioning information is approximately correct, the new antenna orientation ensures the target remains in the principal plane, which has purer radiation polarization during the position scan. The antenna was towed behind an ATV such that it could be lifted off the ground when necessary.

The radar control and data collection was done from a laptop computer via special purpose software developed during this project. Both frequency-domain and time-domain data are

displayed in real time so that the operator can monitor the status of the operation. Although on-site processing can be performed immediately after each pass, the actual processing was performed overnight to maximize the data collection rate.
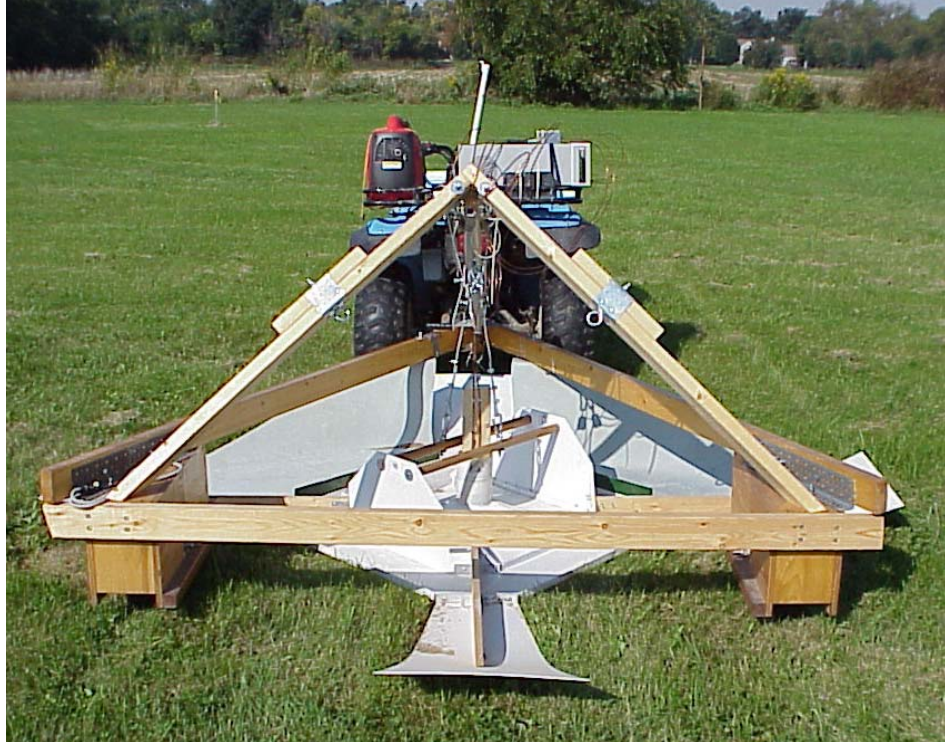
Figure 1 Towed antenna oriented parallel/transverse to the motion direction.

1.2 Measurement Approach

The focus of this project is on discrimination, not detection.   That is, we assume that an earlier pass with a magnetometer or metal detector has produced position information for anomalies which we will investigate further to produce a UXO-like vs non-UXO classification. Our initial pass through each designated target spot was conducted at an arbitrarily chosen direction unless available magnetic sensor data provided a strong suggestion of the orientation of the target. Each pass length was about 10 feet long with a sample spacing of 3 inches. At each sampling location, full-polarimetric data (both amplitude and phase, in two co-polar and one cross polar orientation) was collected from the two orthogonal antenna elements from 10 MHz to 410 MHz at a 2 MHz increment. This information can be manipulated mathematically to produce equivalent co- and cross-polarized returns that would be expected from any other

3

polarization orientation. This full-polarimetric ultra-wideband measurement, not available in any other GPR systems we know of, offers a unique capability for deriving signal parameters which allow the inference that an elongated target is present. Further, the length of the target may be estimated as well, based on a concomitant estimation of soil dielectric properties.

The data from a days surveying is easily stored on devices attached to the rig; it is then processed overnight rather than in real time, in order to speed up the data collection rate. After an initial pass for each target, a *single* additional pass orthogonal to the initial pass was taken for any target that showed poor resonance and preferred polarimetric orientation. A preferred polarization that produces late-time resonance suggests the orientation of an elongated target. Absence of resonance offers no preferred orientation to guide subsequent passes, and further suggests that the object is not UXO-like. For targets that showed significant resonance and linearity features from the overnight processing, *two* additional passes were made in the directions parallel and transverse to the estimated target orientation extracted from the initial-pass data. The idea was of these latter two pass orientations was to get views of the target with polarization optimally aligned with its principal directions, rather than having to infer data in those directions. Figure 2 indicates all the passes performed at the Blossom Point site. To test for the effects of positional uncertainty, additional passes were performed for several calibration targets (Rows 13~15) with the introduction of 10-inch and 20-inch position offsets along the 225-degree direction.

Direction of Scans for Blossom Point Measurements
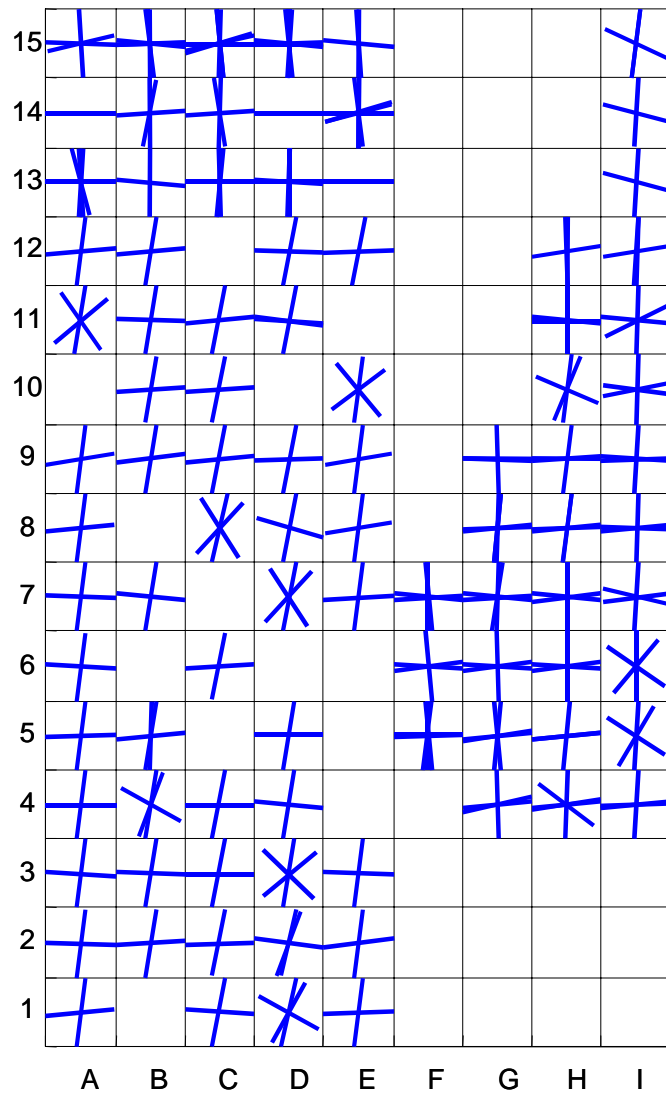
Figure 2 **Measurement passes performed at the Blossom Point Site.**

Chapter 2 Improved Processing Techniques

This chapter discusses several new data processing techniques developed to significantly improve the accuracy of the extracted features.

2.1 Improved Depth and Late-Time Region Estimation

The full-polarimetric, broadband GPR data collected from different positions and passes for each target was processed in a similar technique used in the Demo I for each position. A background response for each channel for each pass was generated from the ensemble average of all positions in that pass. For background removal (e.g. layering) this data was then subtracted from data at each antenna position, before the feature extraction procedure.

During the Demo I, the target portion of response was based on a single time waveform collected at a single, hopefully optimal position. The optimal position was often not so clear. This can occur when the necessary signal level is not much greater than the clutter level, as in the cases of deep target where the target response is weak, or for a shallow small target where surface clutter is significant. An improved method of selecting the onset of the late-time response associated with the target is made possible by the multiple position data. With additional position scans, the target produces a hyperbolic arc, as appears in most conventional GPR data plots showing signal magnitude through time (vertical axis) vs antenna position (horizontal axis). We designate this as a time-position plot. The inhomogeneous layers do not have this temporal-spatial feature as demonstrated in Figure 3 for a UXO buried at 75cm depth. Observing the signal travel time to the peak of the arc also improves the accuracy of depth estimation, relative to using data from a single position.

Arcs such as that in the figure appear because, as the antenna moves further away from the position directly above the target, the signal travel time to and from the target becomes longer. Thus for offset antenna positions the target response appears later in time. The relatively clear arc in the figure is an early-time response, resulting from the first reflection of the signal from the target. While they are not easily visible without further processing (see next section), this initial arc is followed by a succession of later, weaker arcs, representing reverberations of a sort, i.e. late time resonance. Using a graphically interactive routine, the user of the data analysis program simply designates a window on the time position plot, delimiting a region clearly below the first response represented by the hyperbolic arc. The exact boundaries of this window are not crucial, because more detailed processing of the signals within this window indicates where resonance occurs.
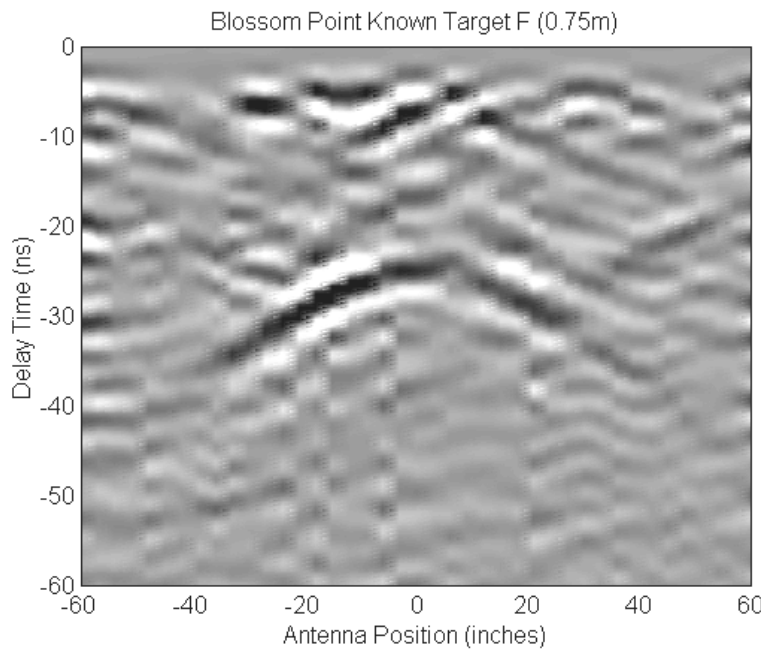
Figure 3   Time- position plot of GPR data, with background removed, before application of adaptive data smoothing.

2.2 Adaptive Data Smoothing for Clutter Suppression

7

A new special algorithm that performs data smoothing along these arcs has been implemented to greatly improve the signal-to-clutter ratio. In addition to the arcs associated with the desired target, there are also other arcs with different intensities and curvatures resulting from surface and subsurface clutter. This phenomenon can be clearly observed in Figure 3. These undesirable arcs interfere with the target responses and cause errors and instability in feature extraction. By applying a smoothing window that runs along the target-arc curves in the whole data region, such interference can be reduced. This is demonstrated by comparing the smoothed data, Figure 4, with the data before smoothing, Figure 3. The arc shape for processing is generated based on a few points selected by the operator. Again, precise selection of the points is not crucial. Figure 4 shows that, after the smoothing, clutter has been reduced effectively and late time arcs are now visible, approximately parallel to the original early time signal. Another example is given for a vertically buried UXO (Blossom Target C, Figure 5), which characteristically produces a weaker peak and stronger sides in the arc. Note the improved data quality in the late-time region below the initial arc. A group of arcs associated with the trench is also observed near the surface (-7 ns position).
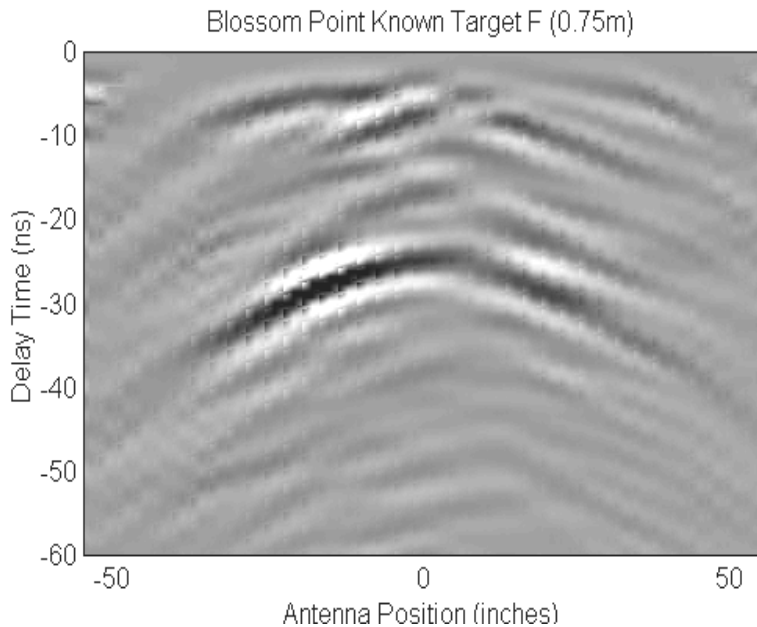
Figure 4 The background-removed GPR data after application of adaptive data smoothing

a)

b)
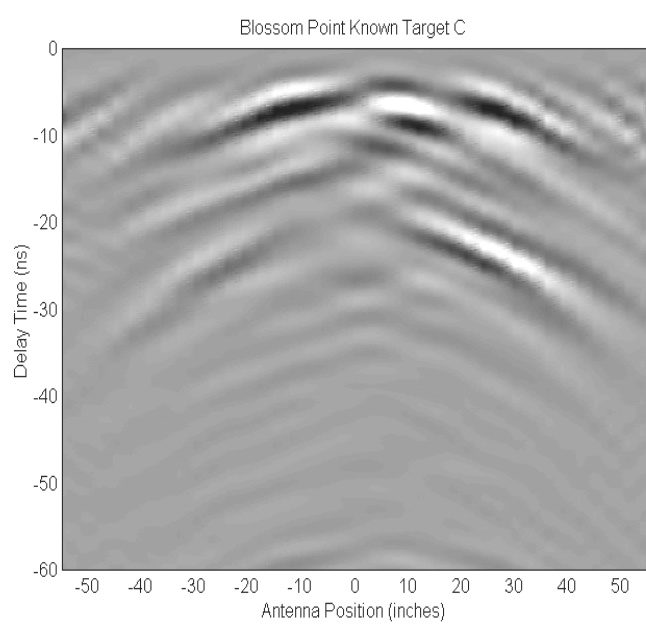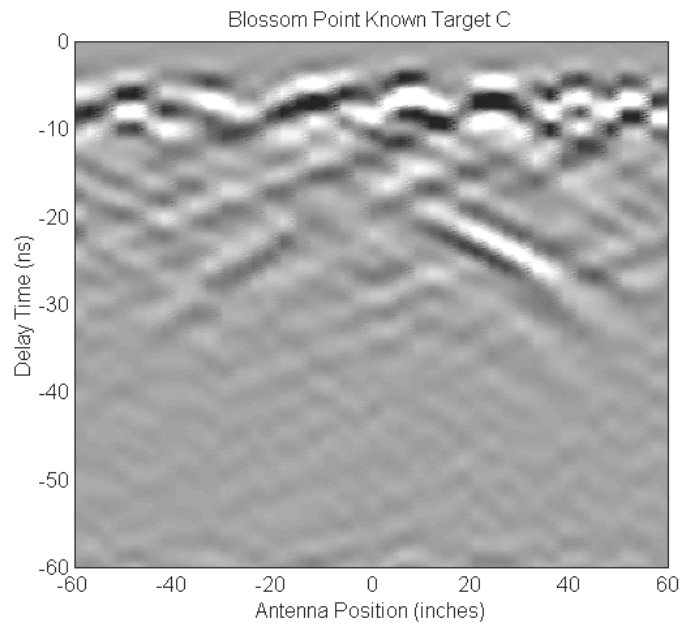
Figure 5   Comparison of GPR data before (a) and after (b) adaptive data smoothing. The target is a vertical UXO (Blossom Point Known Target C).

2.3 Adaptive Filter To Enhance Target Resonance

An adaptive bandpass filter using the Kaiser window function is applied to the late-time spectrum to select the resonant peak. This filter is adaptive because its center frequency and bandwidth are determined according to the target's resonant spectrum. The Kaiser window was chosen because it produces low sidelobe levels in the time domain, when the frequency domain data is inverted. Using a convenient graphical software interface to select the dominant spectral peak and its approximate width, the operator determines the filter's center frequency and relative bandwidth.   This is normally obtained from the late-time spectrum from a channel that produced the strongest target responses.

2.4 Improved ELF Estimation Using Prony Coefficients

Our recent studies show that improved accuracy of the ELF estimation under the influence of random noise could be obtained by utilizing the autocorrelation process and Prony model coefficients. Previous processing extracts the ELF and other linear feature parameters from each temporal position in the selected late-time response. Then a single parameter was obtained by averaging over the selected late-time region to suppress the noise effect. First, the new processing calculates the autocorrelation responses of the selected late-time responses. The Prony model is applied to fit the autocorrelation response of each channel (***at some point identify these with "channels" S_{11}, S_{21} and S_{22}) with complex exponentials. The magnitude of the late-time response in each channel is now represented by a single dominant Prony coefficient. The two eigenvalues and eigenfunctions are then calculated from the Matrix form by the Prony coefficients from the three channels. Recall that these eigenvalues and eigenfunctions are used for ELF and ETO estimation. Notice that the eigenvalues and eigenfunctions only have to be solved once for one waveform. The previous approach required them to be solved from every time position in the late-time region. The final two eigenvalues and eigenfunctions were then

obtained from the temporally averaged values. The magnitudes of the dominant resonance components in each channel are then used to form a 2x2 scattering matrix from which ELF, ETO and DEN are estimated. It should be noted that, in the previous processing, Prony processing was applied only to the strongest response channel for extracting the resonance information. This new approach is more effective than the previous averaging approach in suppressing random noise. Figure 6 compares the extracted ELF in the presence of different noise levels from the previous approach to that obtained from the new. The noise level is expressed as SNR, i.e. signal to noise ratio, usually measured in dB. More precise definitions and analyses of SNR and signal to clutter ratio (SCR) are to found below in Chapter 6, where effects of those two types of signal contamination on extracted parameters are pursued. Here the signal is assumed to be a linearly polarized damped resonance characterized by $\cos(0.3t)\exp^{-0.05t}$ with Gaussian distributed random noise added. These results were obtained using 500 noise realizations. The improvement of the new Prony approach is quite significant for SNR greater than 10 dB. For SNR less than 10 dB, almost all processing methods will have difficulty in obtaining the correct ELF, i.e. 1.
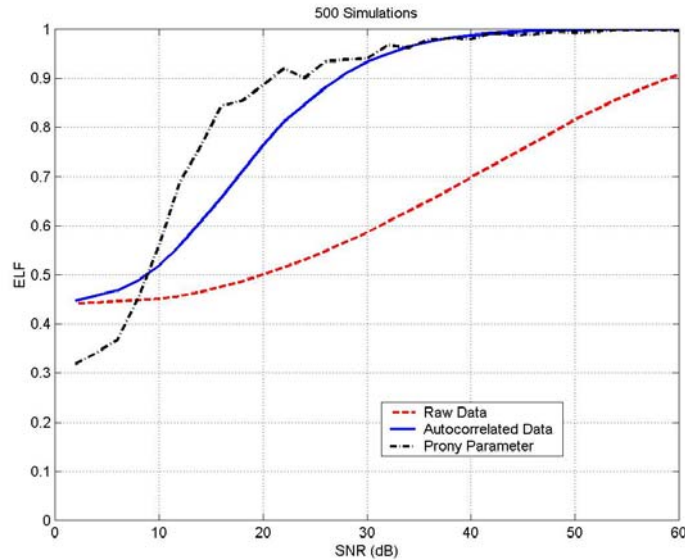
Figure 6   Comparison of different method of extracting ELF feature in the presence of different noise level.

11

2.5 Block Diagram of New Feature Extraction Procedure

Figure 7 shows the block diagram of the improved processing procedure. The details of the feature extraction block are similar to those used in Demo I and can be found in [1,2]. The final output contains the extracted ELF, DEN, ETO and CNR features as a function of antenna position. Several new processing blocks (shadowed) have been discussed in the previous paragraph and are introduced to improve the accuracy in the presence of noise and clutter.
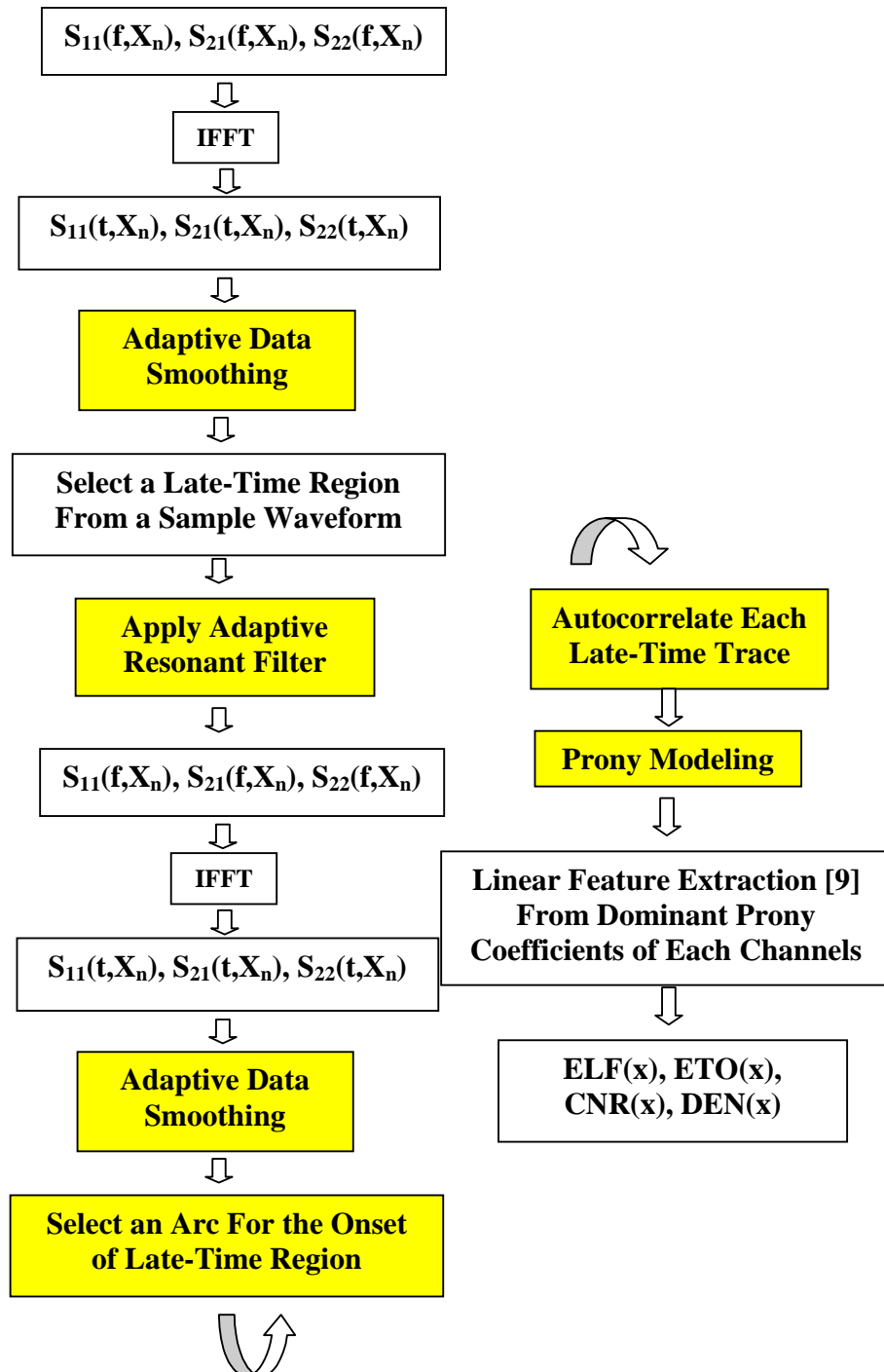
Figure 7   **Block diagram of the improved UXO feature extraction algorithm.**

Chapter 3 Improved UXO Classification Using Spatial Feature and Scattering Pattern

3.1 Previous Classification Problem

Many false alarms were caused by unbalanced excitation due to the target offset near the fully-polarimetric antenna as shown in Figure 8(a) and (b). This causes the extracted polarization feature to resemble that obtained from a truly linear object, i.e. an object like a UXO, as shown in Figure 8(c). Utilizing the spatial distribution of features obtained from multiple-position data, the non-linear object shows low linearity as the antenna is moved close to the top of the target. This makes it easy to be separated from a UXO-like target with a small inclination angle. However, from this feature alone, one still could not discriminate the non-linear object from a steeply inclined UXO as illustrated in Figure 8(d). A similar null of linearity will be observed from this type of UXO although the good linearity observed at offset positions may result from oblique excitations. Additional early-time scattering features due to the two scattering mechanisms associated with the nose and tail of the UXO can sometimes be used to separate it from a small non-linear object that contains only one scattering point. Sometimes a large horizontal plate also has multiple scattering edges, its strong reflection from the flat surface makes it easy to distinguish from a vertical UXO. These will be demonstrated by actual measurement examples.
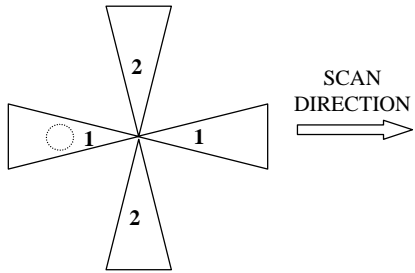
(a) top view w/ a non-linear target beneath the antenna
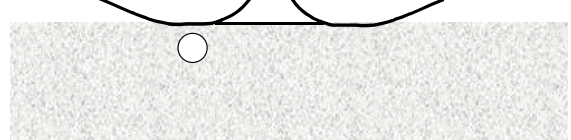
(b) a non-linear target beneath the antenna
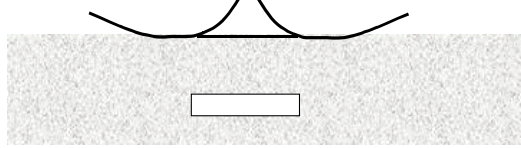
(c) a horizontal linear target beneath the antenna
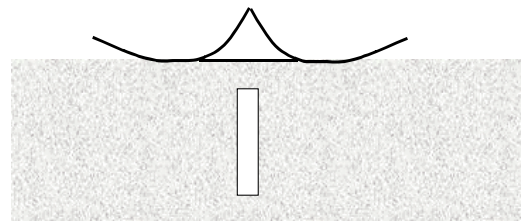
(d) a vertical linear target beneath the antenna

Figure 8 Different scenarios of linear and non-linear objects beneath the HFB antenna.

3.2 Examples from Known Targets

A set of known targets was available for tuning the system and processing. The pictures and descriptions of these targets are shown in Figure 9 and Table 1, respectively. Table 2 also shows their locations, depths and orientations.
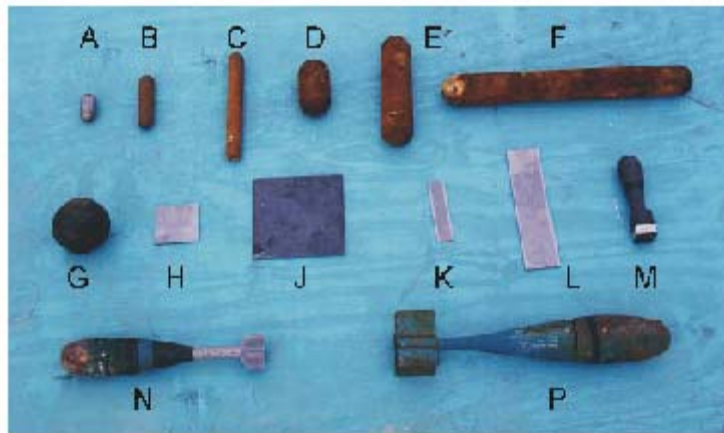
Figure 9   Pictures of known targets at Blossom Point site.

Table 1 Descriptions of Known Targets

Item ID	Description	Item ID	Description
A	1½" x 3" solid steel cylinder	G	16 lb steel shotput
B	1½" x 6" solid steel cylinder	H	4" x 4" x ¼" steel plate
C	1½" x 12" solid steel cylinder	J	8" x 8" x ¼" steel plate
D	3" x 6" solid steel cylinder	K	1½" x 6" x ¼" steel plate
E	3" x 12" solid steel cylinder	L	3" x 12" x ¼" steel plate
F	3" x 24" solid steel cylinder	M	

Table 2 Locations, Depths and Orientations of Know Targets

Row/Column	A	B	C	D	E
15	16-lb shotput 25 cm	Item L 25 cm/ 0° / 0°	Item B 20 cm/ 0° / 0°	Item A 5 cm/ 0° / 0°	Item K 8 cm/ 0° / 90°
14	Item H 5 cm/ 45° / 0°	Item H 25 cm/ 0° / 90°	Item J 25 cm/ 45° / 0°	Item C 35 cm/ 0° / 90°	Item F 75 cm/ 0° / 0°
13	Item P 75 cm/ 0° / 90°	Item D 10 cm/ 0° / 90°	Item E 50 cm/ 0° / 90°	Item N 35 cm/ 0° / 90°	empty

The relative permittivity and conductivity of the soil at 60 MHz are shown in Appendix B as a function of depth. Figure 10 plot the delay time vs. antenna position plot of the energy of the measured fully-polarimetric data for a horizontal UXO-like Object (Target B). The grayscale indicates the amplitude of the scattered fields. Notice that S_{22} channel contains most significant response because antenna 2 is parallel to the UXO axis. Figure 11 shows the estimated linear factor (ELF) and orientation (ETO) as a function of position. The large ELF values when the antenna is near the target location clearly indicated a linear object, i.e. an UXO-like target. Accurate orientation estimations are also obtained.

Figure 12 and Figure 13 plot the measured and processed results for a buried vertical MK23 (Target M). Notice the low ELF region near the center because the UXO has a rotational symmetry when observed directly above. S_{11} shows the dominant responses and shows maximal response when the antenna is offset from the target. This is due to the stronger excitation of resonant modes of the UXO when incidence is from the side. In general, we will see insignificant scattering for an UXO when the direction of incidence is directly along the UXO axis, within our operational frequency range, except for an extremely large UXO. Two scattering arcs that have different curvatures are clearly observed between position 15 and 40 in Figure 12(a). These are generated from the nose and tail of the UXO. The smaller curvature one is generated form the bottom of the UXO and the larger curvature one is generated by the top of the UXO. The estimation orientations are aligned with the orientation of the antenna 1 .

Figure 14 and Figure 15 plot the measured and processed results for a shallow conducting sphere (Target G). The single arc pattern indicates only one scattering point. This is different from what observed in the previous vertical UXO case. Notice that the ELF peaks up in two regions offset from the center. These regions correspond to the portions of the antenna 1 that are closest to the ground surface as illustrated in Figure 8(a). It is not surprising to find that the estimation orientations are aligned with the orientation of the antenna 1 (90 degrees in this case). Similar results can be obtained from a small plate (Target H) as shown in Figure 16 and Figure 17.

Figure 18 and Figure 19 plot the measured and processed results for a large, horizontal conducting plate (Target J). Similar to the sphere case, the ELF peaks up in two regions offset

17

from the center. Notice the strong reflection observed in middle of both S_{11} and S_{22} channels. This is distinctive from a sphere or a vertical UXO except for a very large nose-down UXO that has a flat end.

(a) S_{11} data for Target B

(b) S_{21} data for Target B

(c) S_{22} data for Target B
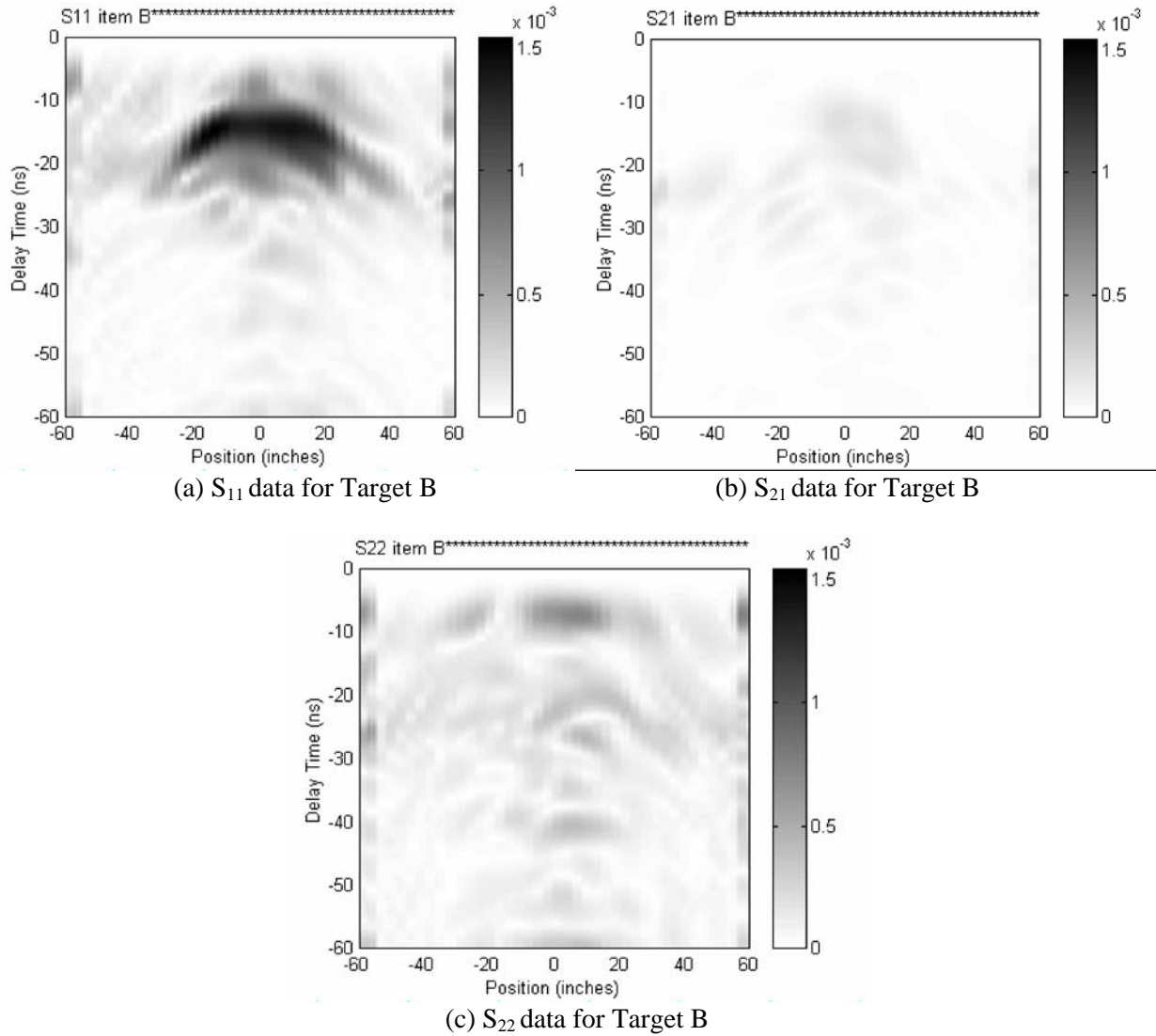
Figure 10   Preprocessed GPR data for Target B (horizontal solid steel cylinder, 1.5" x 6").
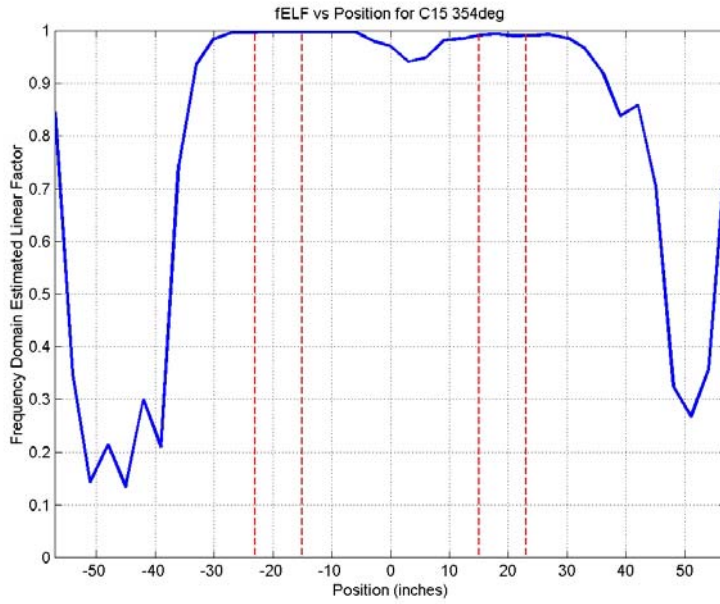
(a) ELF data for Target B
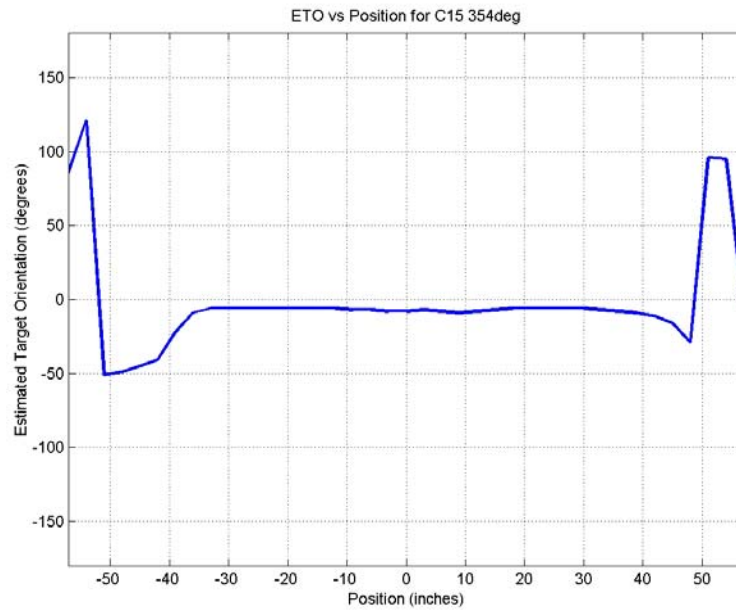
(b) ETO for Target H

Figure 11   Extracted ELF and ETO for Target B (horizontal solid steel cylinder, 1.5" x 6") as a function of antenna position.

(a) S_{11} data for Target M

(b) S_{22} data for Target M

(c) S_{22} data for Target M
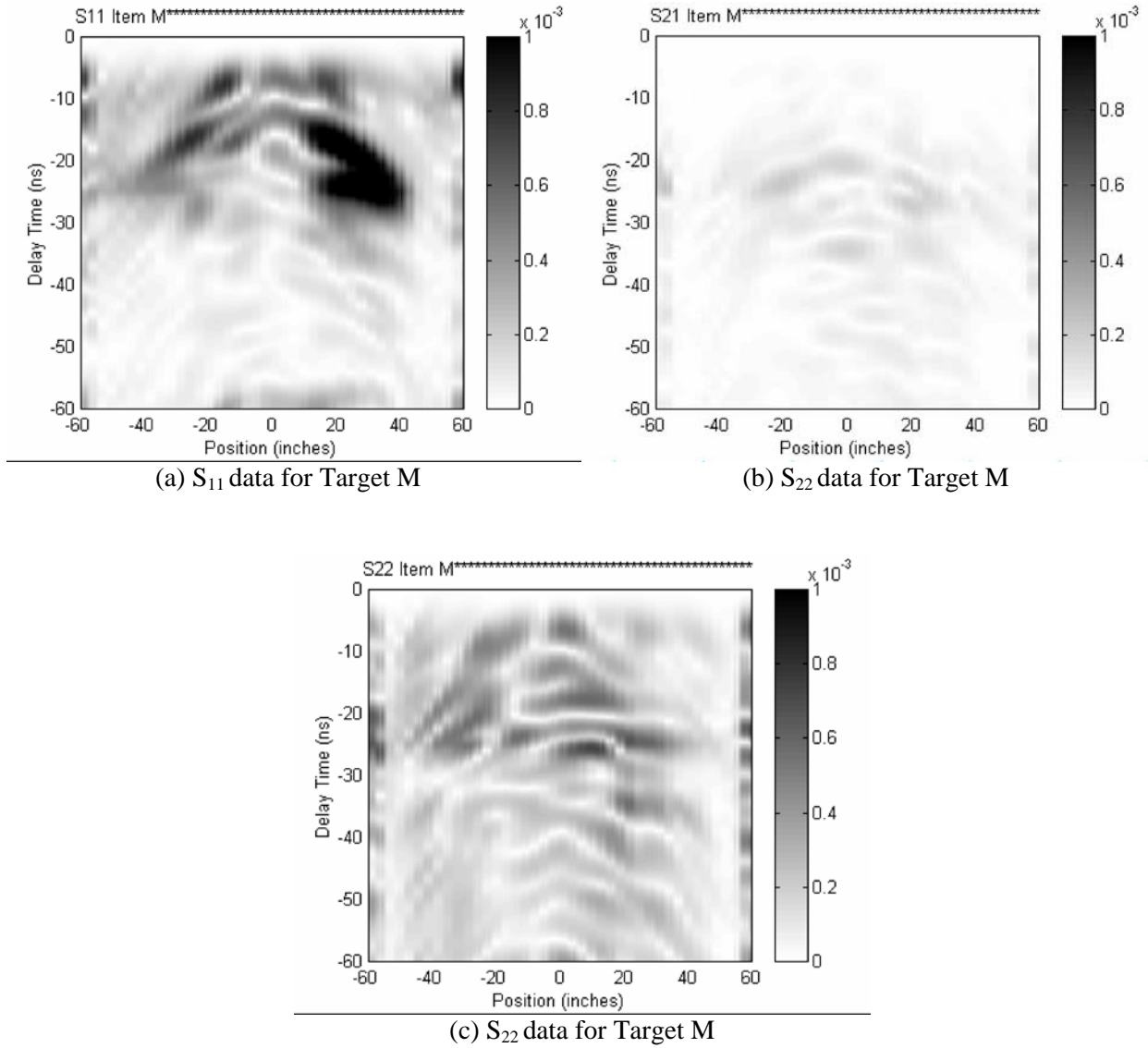
Figure 12.   Preprocessed GPR data for Target M (vertical MK23).
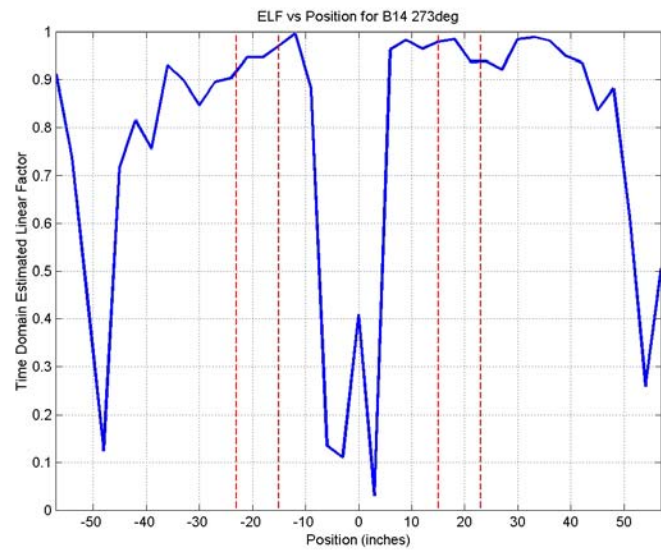
(a) ELF for Target M
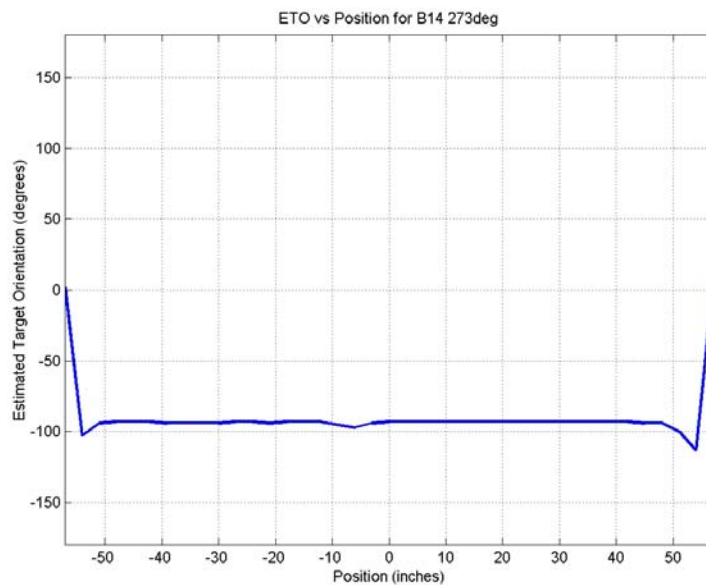
(b) ETO for Target M

Figure 13.   Extracted ELF and ETO for Target M (vertical MK23) as a function of antenna position.

(a) S_{11} data for Target G

(b) S_{21} data for Target G

(c) S_{22} data for Target G
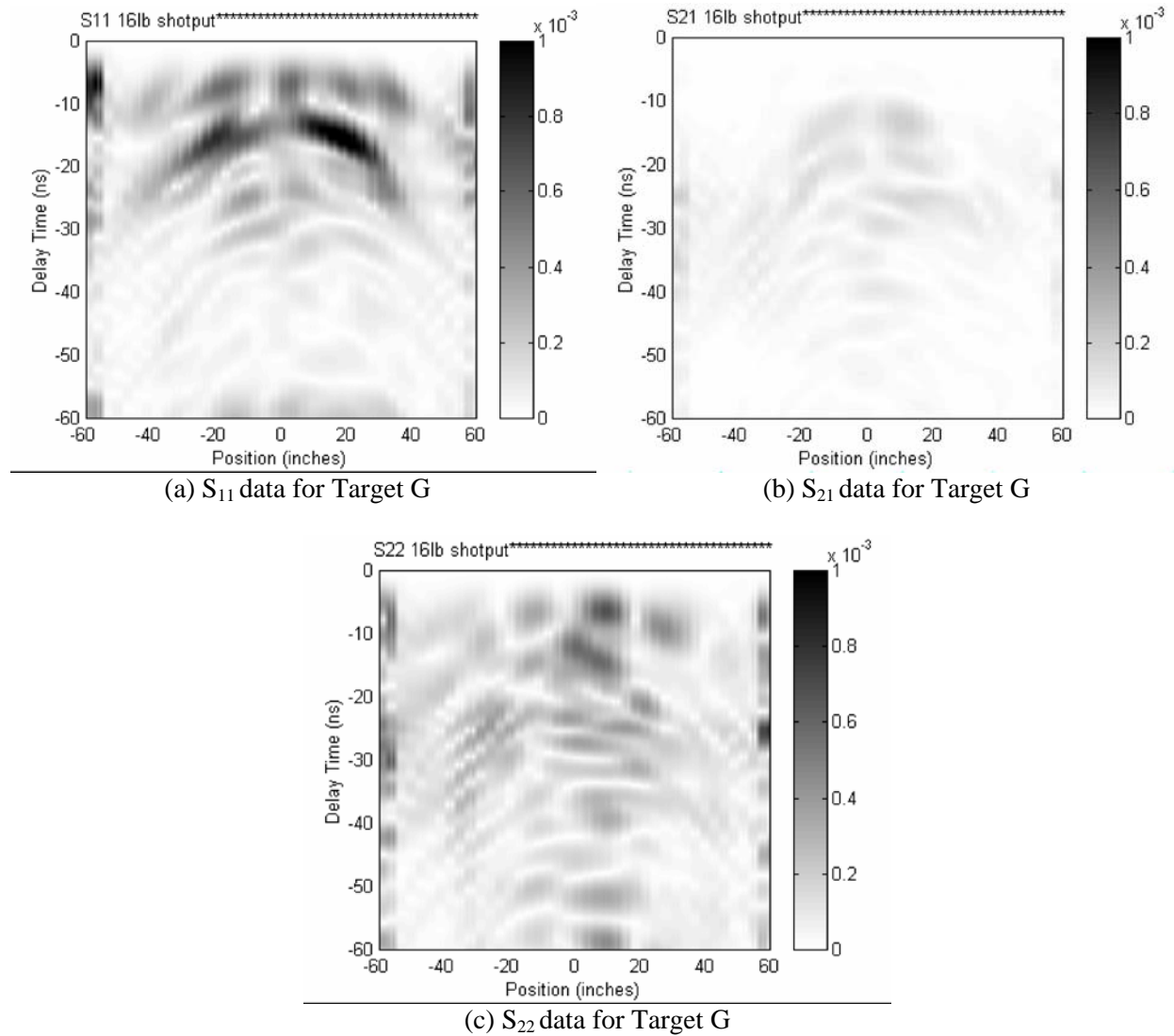
Figure 14   Preprocessed GPR data for Target G (16lb shotput).
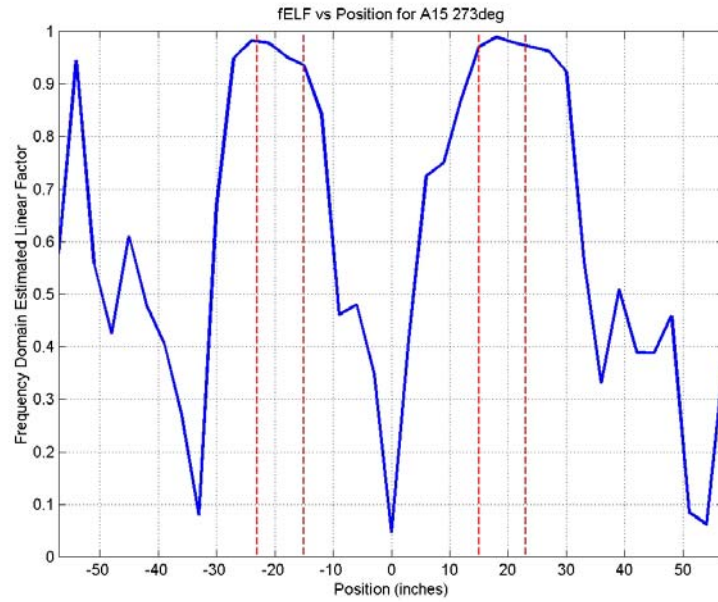
(a) ELF for Target G
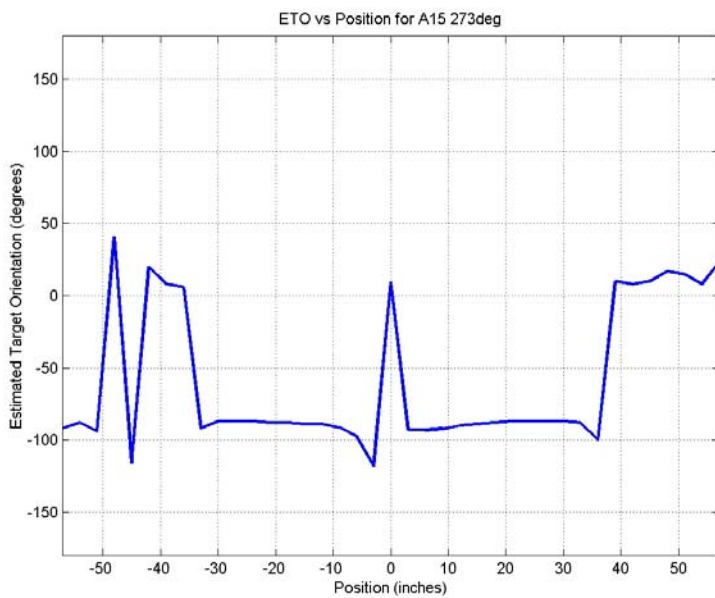
(b) ETO for Target G

Figure 15. Extracted ELF and ETO for Target G (16lb shotput) as a function of antenna position.

(a) S_{11} data for Target H

(b) S_{21} data for Target H

(c) S_{22} data for Target H
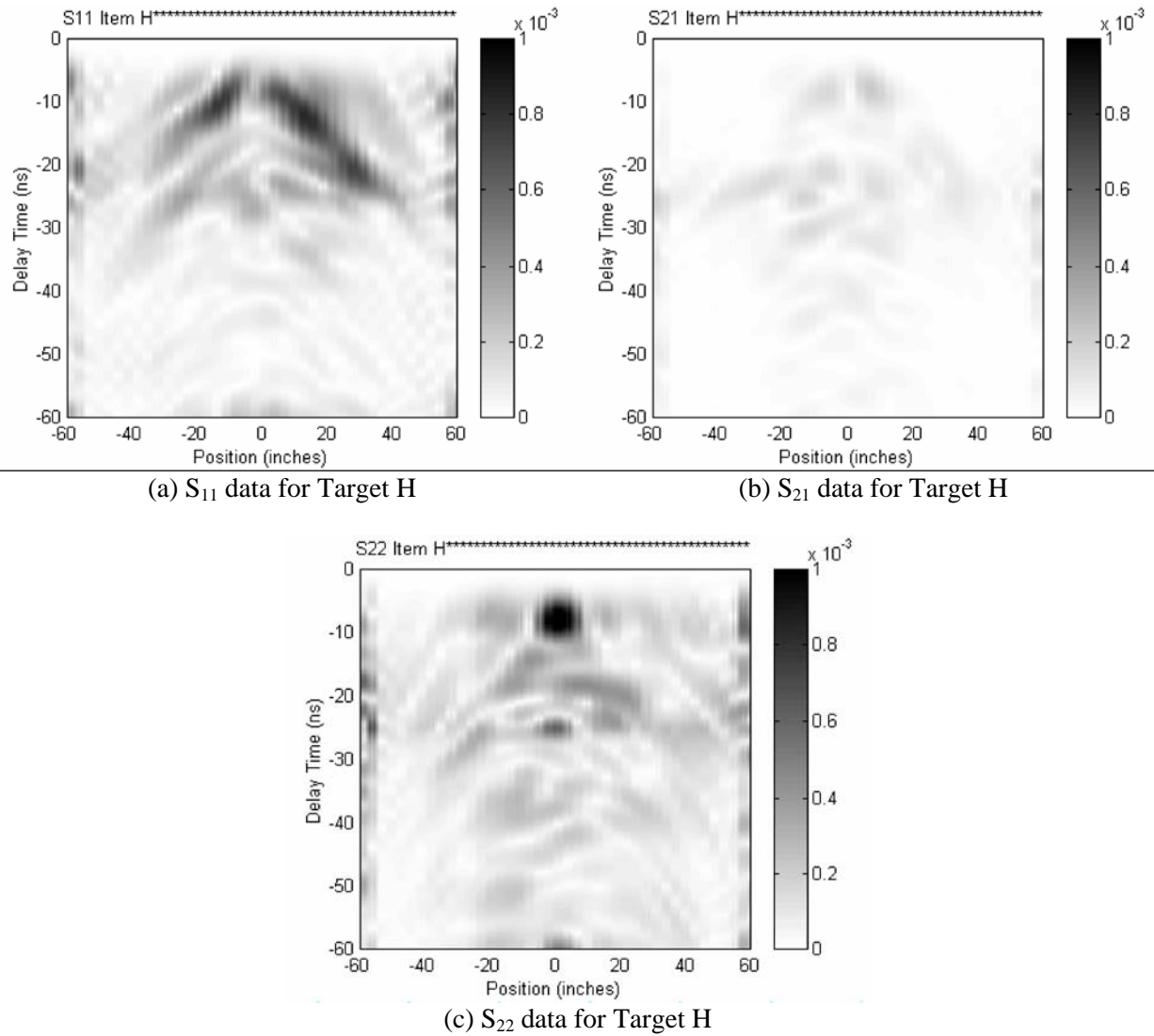
Figure 16   Preprocessed GPR data for Target H (horizontal plate, 4"x 4"x 0.25").

24
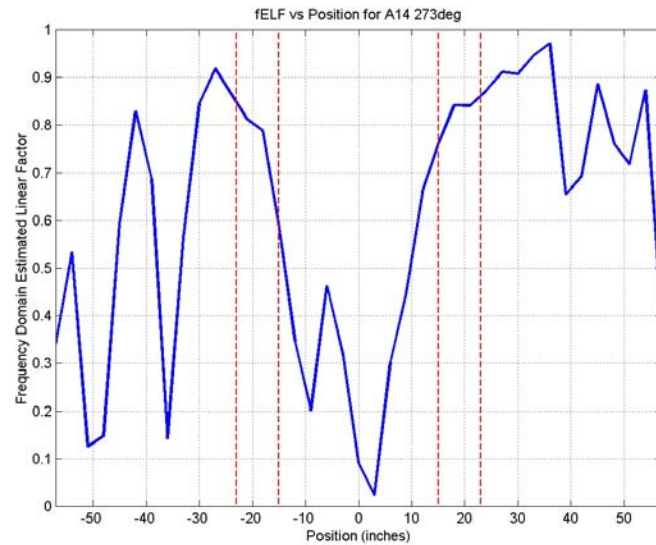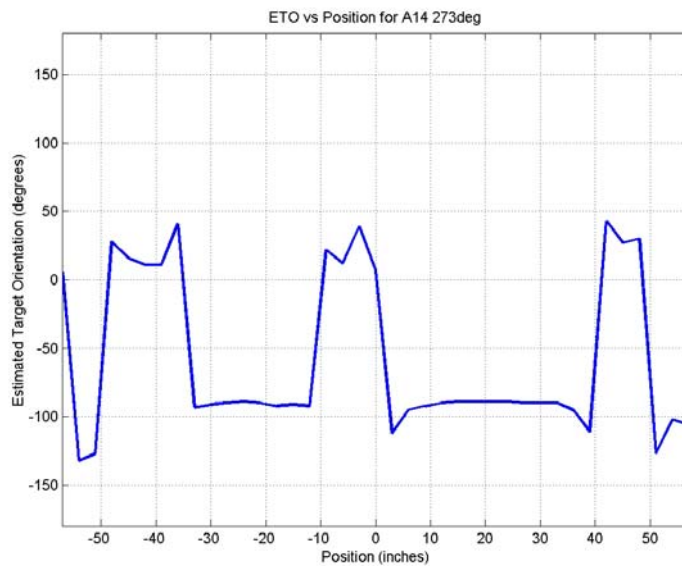
(a) ELF for Target H

(b) ETO for Target H

Figure 17   Extracted ELF and ETO for Target H (horizontal plate, 4''x 4'' x 0.25'') as a function of antenna position.
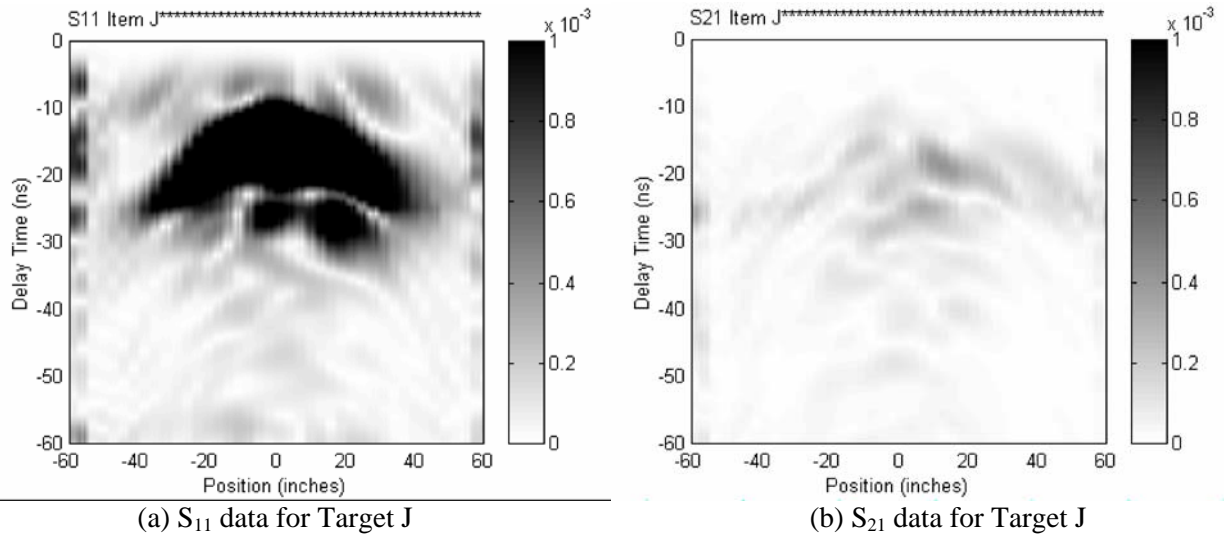
(a) S_{11} data for Target J (b) S_{21} data for Target J
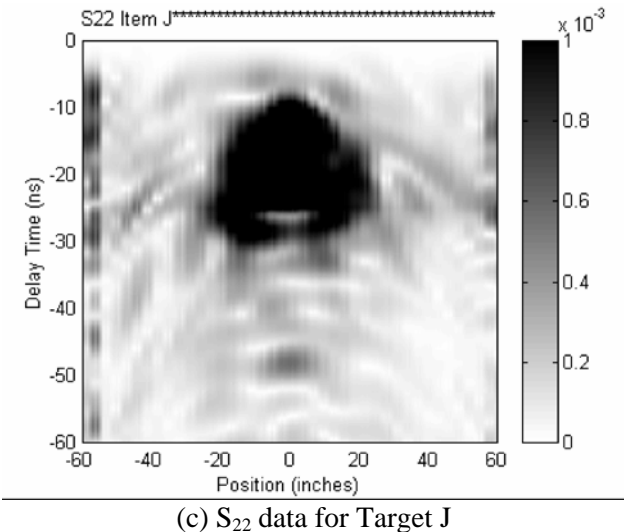
(c) S_{22} data for Target J

Figure 18.   Preprocessed GPR data for Target J (horizontal plate, 8"x 8" x 0.25").
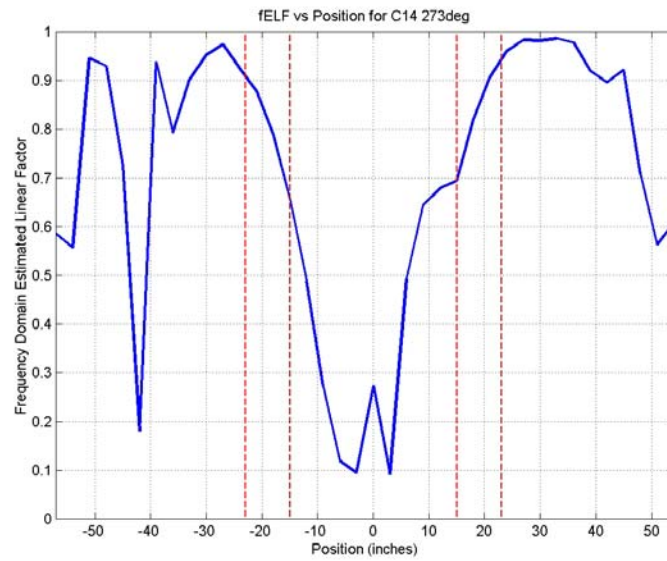
(a) ELF for Target J
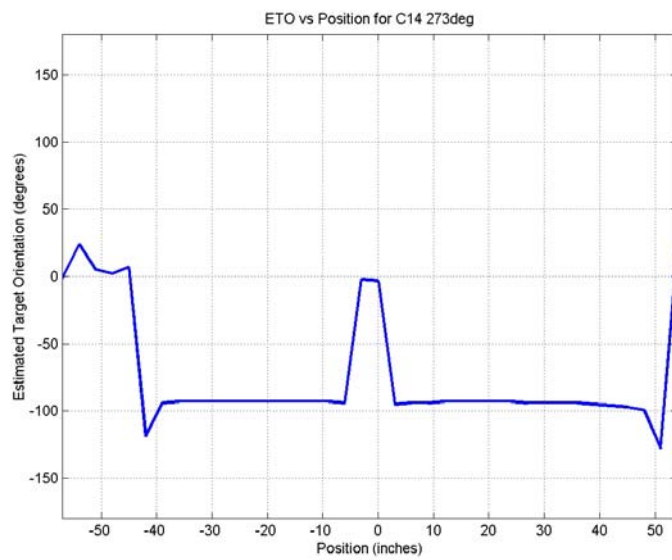
(b) ETO for Target J

Figure 19.   Extracted ELF and ETO for Target J (horizontal plate, 8''x 8'' x 0.25'') as a function of antenna position.

Chapter 4 Feature Extraction and UXO
Classification of Blossom Point Targets

4.1 Known Target Feature Extraction

The linearity (ELF), orientation (ETO) and length (ETL) features for all blind test targets are chosen from a position that is within the best linearity region, i.e. the highest ELF values among all the positions and all the passes associated with that particular target. This occurs unless the processing has excluded the apparent linearity as spurious, as in the case of a compact, near-surface target, which always excites the S_{11} response more strongly than S_{22}. For a UXO that does not have a large inclination angle, this choice gives the best orientation and length estimation (LEN). A relative permittivity of 20 was used in converting from the delay time to depth, and from the resonant frequency to length. This relative permittivity value was found to be approximately the average value of the actual probe data as shown in Appendix B.

The estimated depth (DEP), target length (ETL) and target orientation (ETO) for the known targets were found to agree well with their true values as shown in Table 3. It was found that, for some reason, target D and E seemed to be swapped based on the depth and length features. It should be noted that for a non-linear target such as a sphere, the estimated length is not directly related to its dimension and therefore has a larger discrepancy. Furthermore, the depth estimation for a UXO that has a large inclination angle is not entirely straightforward, as for example the vertical MK23 (Known Target M) shown in Figure 20 (same as Figure 12(a)). Figure 21 also plots the corresponding bipolar responses for comparison. Since the stronger responses can only be obtained from oblique angles, the middle portion of the hyperbolic arc is weak and usually not obvious. Since the target depth is estimated from the delay time measured from the peak of the hyperbolic arc, extrapolation was used as indicated by the small circles. Notice the two groups of arcs that do not have the same curvature as indicated by the blue and red dashed lines. The lower arc (red line) that has a smaller curvature is caused by the scattering

from the bottom nose of the MK23. The upper arc (blue line) that has a larger curvature is caused by the scattering from the top tail of the MK23. One cannot always see both scattering mechanisms clearly. This depends on the nose and tail geometry as well as the soil absorption and length of the target. The ground surface is located at about the -6 ns position. The scattering caused by disturbed soil is also visible near the surface. Notice that the above discussion has utilized the early-time scattering characteristics, which was not done in processing for our previous Demo. Figure 13(a) shows that the largest ELF values occur at offset positions for this vertical UXO. For other nonlinear targets or UXO-like targets with near vertical inclination angles, the ETO will be the same as the scan direction for the reason discussed in Section 3.2 and does not have much meaning.
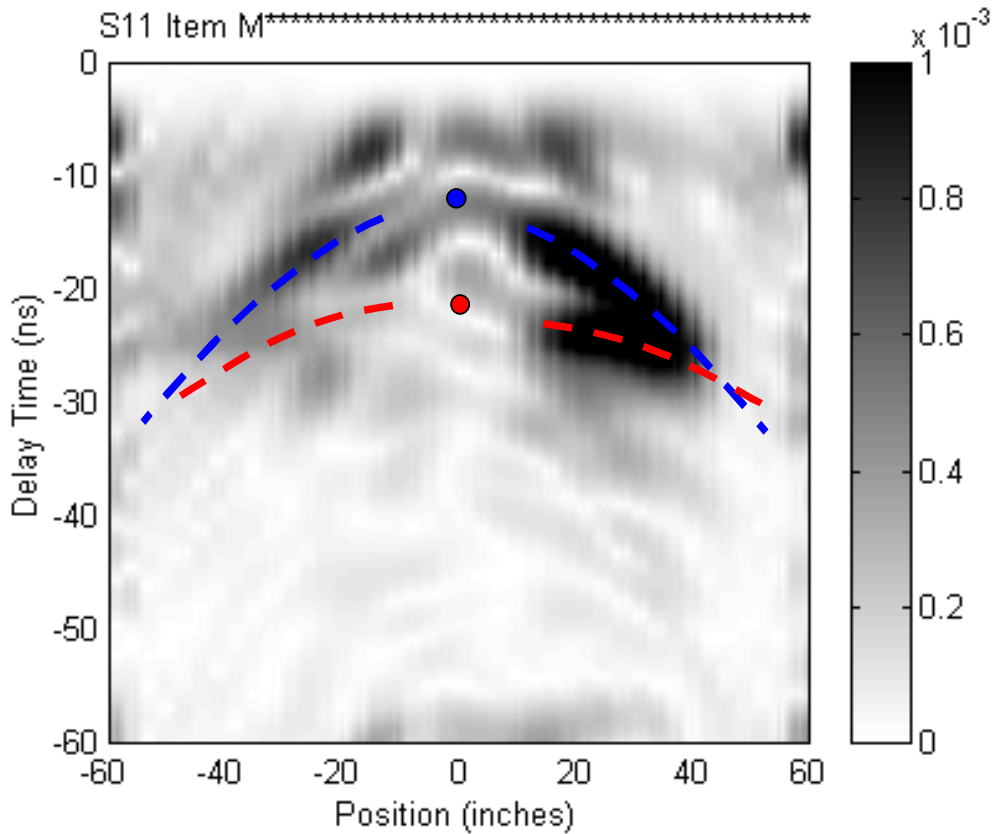
Figure 20. Energy plot of the measured S11 data for the vertical MK23 (Known Target M).
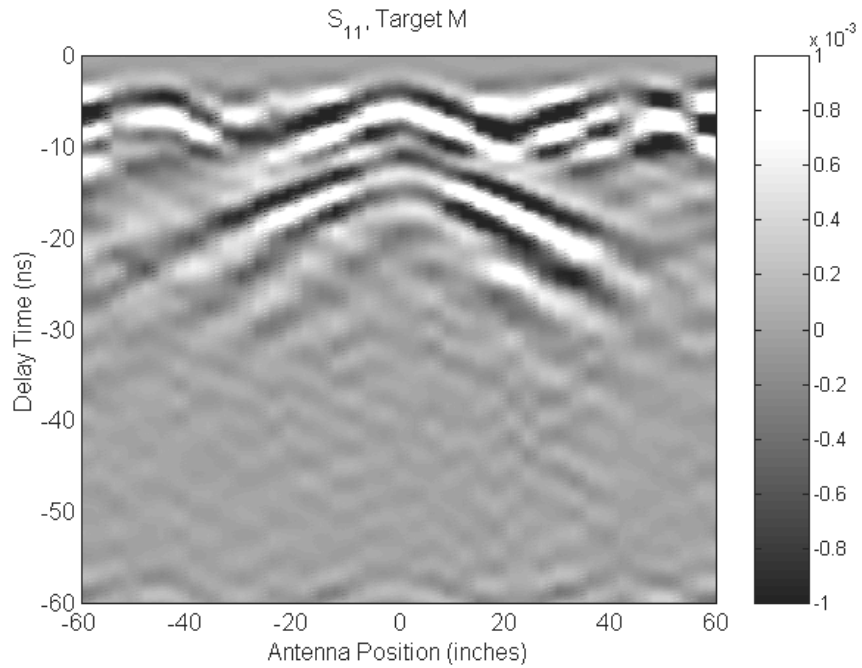
Figure 21 Bipolar plot of the measured S11 data for the vertical MK23 (Known Target M).

Table 3 Features Extracted for Known Targets

TAR#	UXO	Confidence	ETL (m)	True L	ETO	True Orient.	DEP (m)	True Dep.	ID
A13	Y	M	0.448	c	12	0	0.246	0.750	P
A14	N	H	0.196	*	-90	*	0.064	0.050	H
A15	N	H	0.131	*	-92	*	0.195	0.250	G
B13	Y	M	0.203	0.150	-84	*	0.137	0.100	D
B14	Y	H	0.197	*	-94	*	0.202	0.250	M
B15	Y	H	0.381	0.305	-8	0	0.289	0.250	L
C13	Y	L	0.137	0.305	-92	*	0.195	0.500	E
C14	N	H	0.239	*	-97	*	0.210	0.250	J
C15	Y	H	0.152	0.150	0	0	0.253	0.200	B
D13	Y	H	0.116	*	-87	*	0.340	0.350	N
D14	Y	L	0.303	0.305	-91	*	0.202	0.350	C
D15	N	L	0.153	0.076	89	*	0.042	0.050	A
E14	Y	H	0.430	0.610	-9	0	0.631	0.750	F
E15	Y	L	0.243	0.150	-89	*	0.246	0.080	K

Graphically, we show Table 3 table in histogram form below in Figure 22. In the case of target length only the cases are shown for which length determination applies. Cases are sorted in either length or depth magnitude order, not by target number or letter. These plots illustrate that the system for determination of length and depth parameters is basically sound.

Comparison of known target lengths to estimated length (LEN)

Comparison of known target depths to estimated depth (DEP)
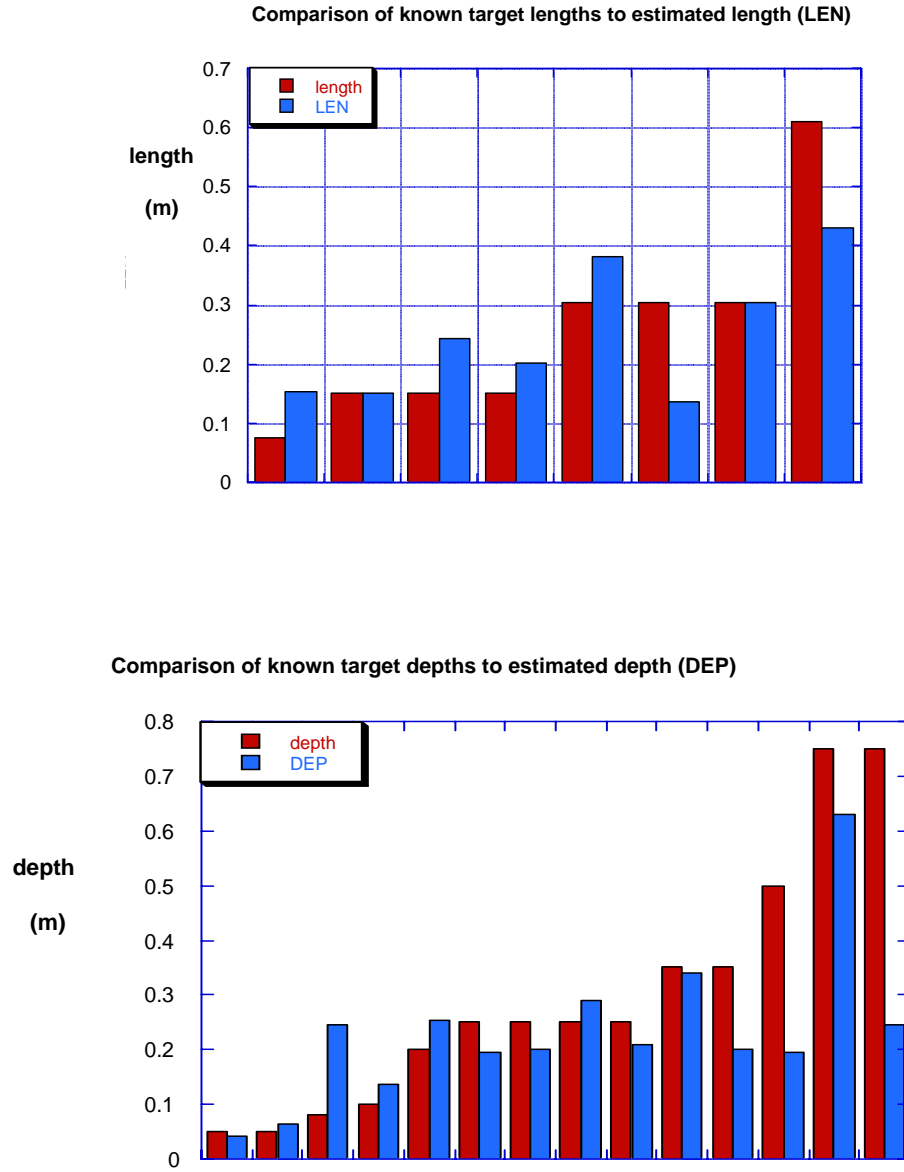
Figure 22.   Comparisons of true and estimated known targets lengths (top) and depths (bottom), sorted by magnitude order.

4.2 Offset Tests for Effects of Positional Uncertainty

Additional data were taken for the known target set with scan center offset from the target location designated by NRL. Two different offsets, 10 inches and 20 inches, were taken to the west and to the south with respect to the designated target center. Figure 23 shows an example of 10-inch offset for target B15, a north-oriented steel strip (3"x12"x0.25") buried at a depth of 25cm (~ 10 inches). In terms of diagonal distance to the intersection of perpendicular survey lines, the two offsets correspond to about 14 and 28 inches. The question we ask here is whether the ability of our system to obtain key processing parameters, discussed above, is degraded by such offsets. In our parlance here, this strip is a UXO-like object in that it presents an aspect ratio of at least 3 to 1 in all orientations. The "good" performance for the offset survey lines would mean extracting signal parameters corresponding to a UXO-like classification. The extracted classification features and the responses for polarization parallel to the scan direction are shown in Figure 24. The transverse responses are much weaker compared to the parallel ones and are not shown. The classification features clearly indicated a UXO-like object, without degradation due to offset. The high ELF region is offset from the survey line midpoint, as expected. The same target was measured again with the offset increased to 20 inches (equivalent diagonal offset of 28 inches), as illustrated in Figure 25. Again, with a positional shift corresponding to the offset, the classification parameters still clearly show UXO-like features (see Figure 26). Therefore, for horizontal ordnance, it seems that position offsets up to 20 inches do not create a problem for classification using the existing features and criteria. This conclusion was also found to be valid for vertical ordnance as shown in Figure 27 and Figure 28. While the patterns of ELF and ETO in these plots may appear a bit ragged for those not accustomed to the typical variability of these signals, the general patterns contrast notably to cases lacking significant linearity, or failing to show coincidences of linearity and distinct orientation. Note that a given offset should cause less of a problem for deeper targets, assuming that increased signal absorption over depth does not obscure the data content. Overall, discounting attenuation effects over depth, we expect offset effects to be similar for cases when the ratio of offset to depth is similar. In the case of target B15, good results were obtained for offset (closest point on survey path to target location)equal to twice the target depth.
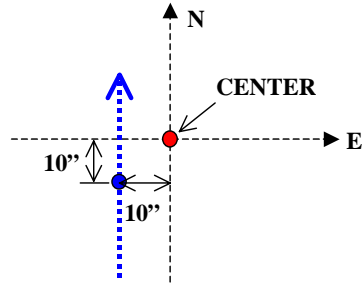
Figure 23. **A north-directed scan with its scan center offset from target center by 10 inches from both east and north direction.**
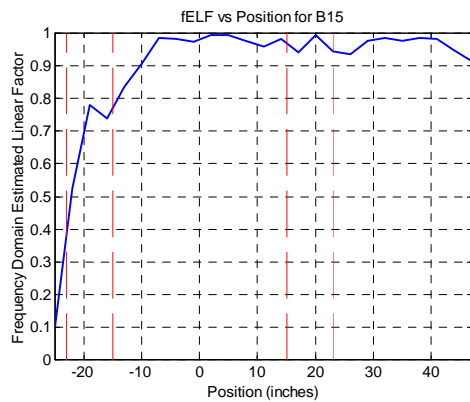
(a) Estimated linearity factor (ELF)
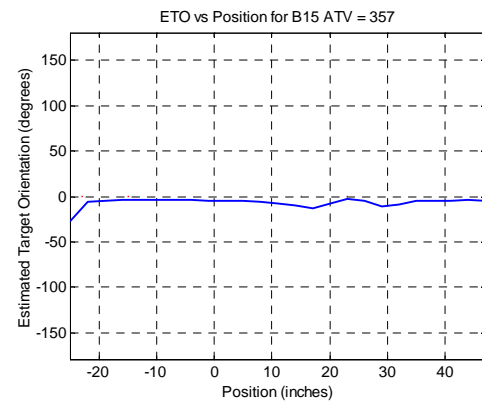
(b) Estimated target orientation (ETO) relative to North
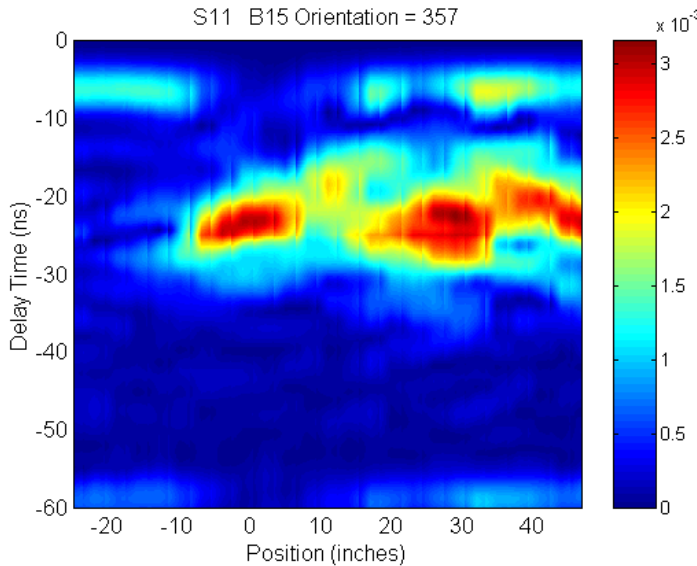
(c) S_{11} : Received signal in same polarization as transmitted field, parallel to the scan direction, as a function of antenna position. position.

Figure 24 **Classification features and position-time plot for target B15, obtained form the 10-inch (14 inch diagonal) offset survey path.**
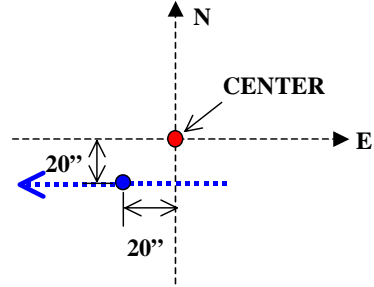
Figure 25   An East-West scan with its scan center offset from target center by 20 inches from both east and north direction.
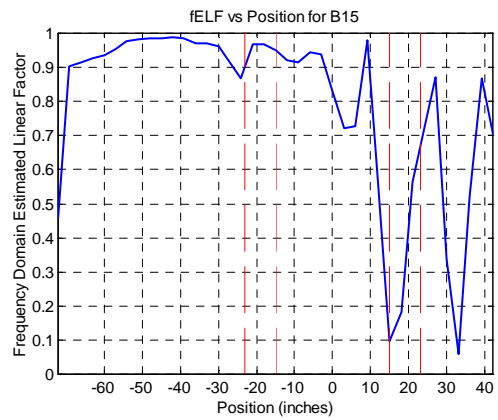
(a) Estimated linearity function ELF for target B15 with survey path offset 20 inches.
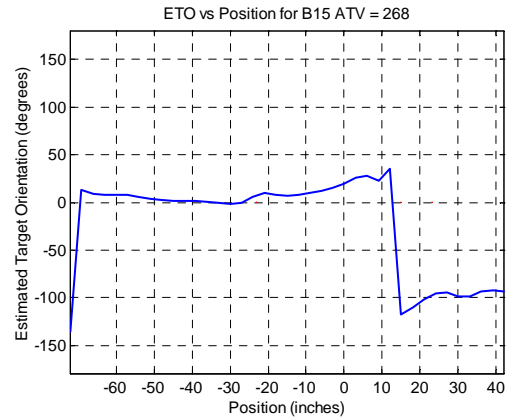
(b) Estimated target orientation ETO for target B15 with survey path offset 20 inches.
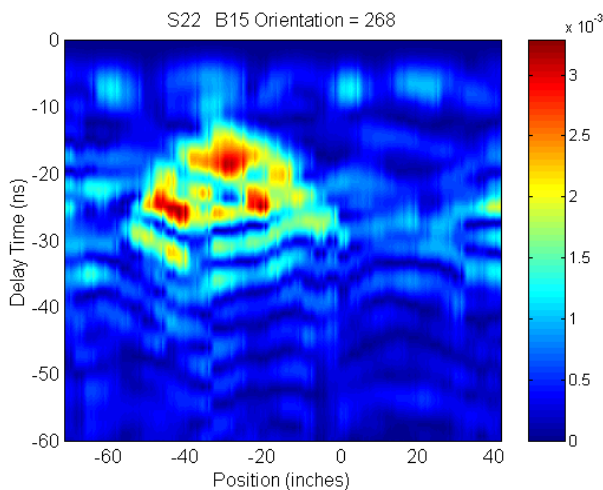
(c) S_{11} (transmitted and received signals both parallel to scan direction), as a function of antenna position.

Figure 26   Classification features and position-time signal plot, for target B15, obtained from the 20-inch offset survey path.
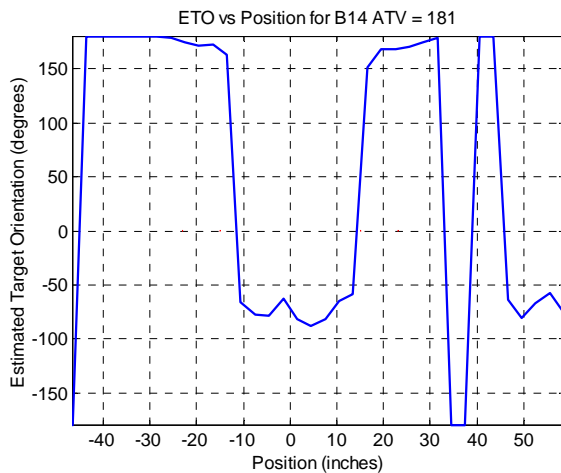
(a) Estimated linearity function ELF for vertical MK23 with survey path offset 10 inches.
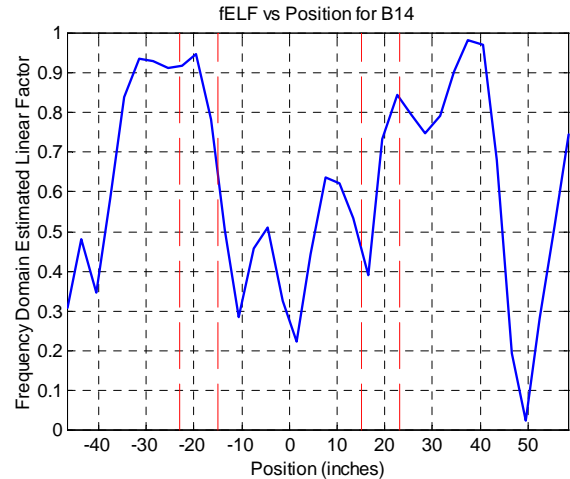
(b) Estimated target orientation ETO for vertical MK23 with survey path offset 10 inches
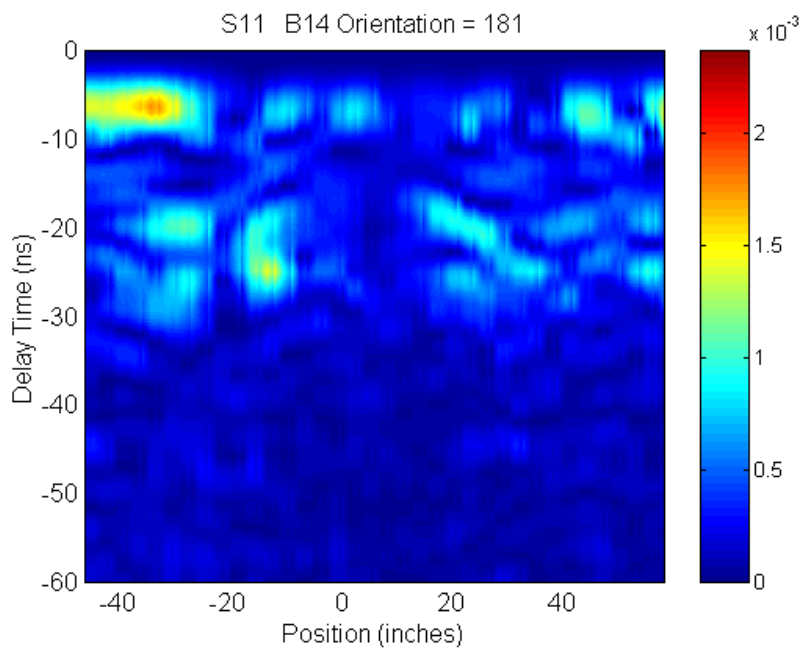
(c) S_{11} (transmitted and received signals both parallel to scan direction), as a function of antenna position.

Figure 27   Classification features for a vertical MK23 bomb obtained form the 10-inch offset configuration.
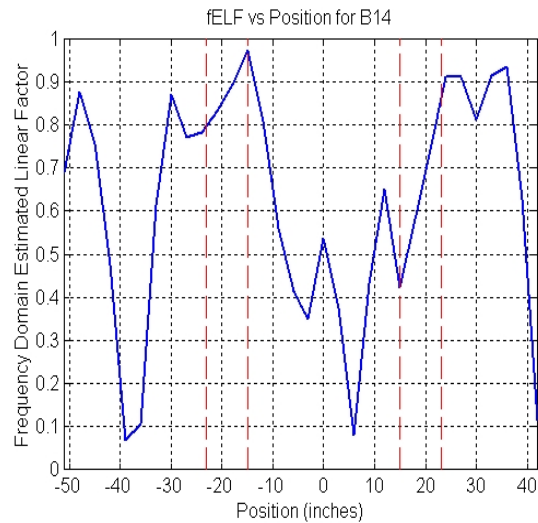
(a) Estimated linearity function ELF for vertical MK23 with survey path offset 20 inches.
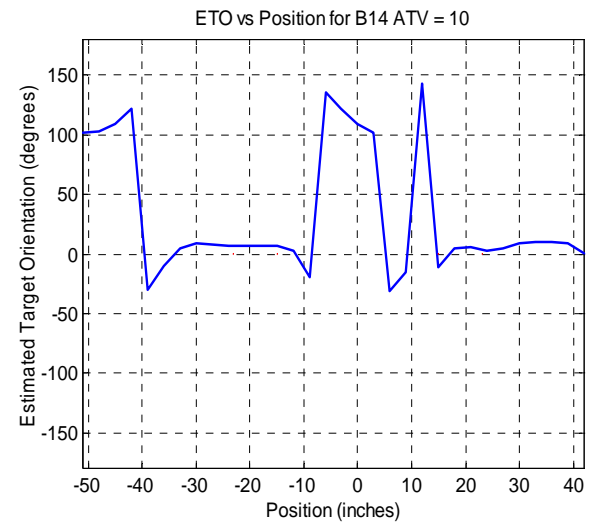
(b) Estimated target orientation ETO for vertical MK23 with survey path offset 10 inches
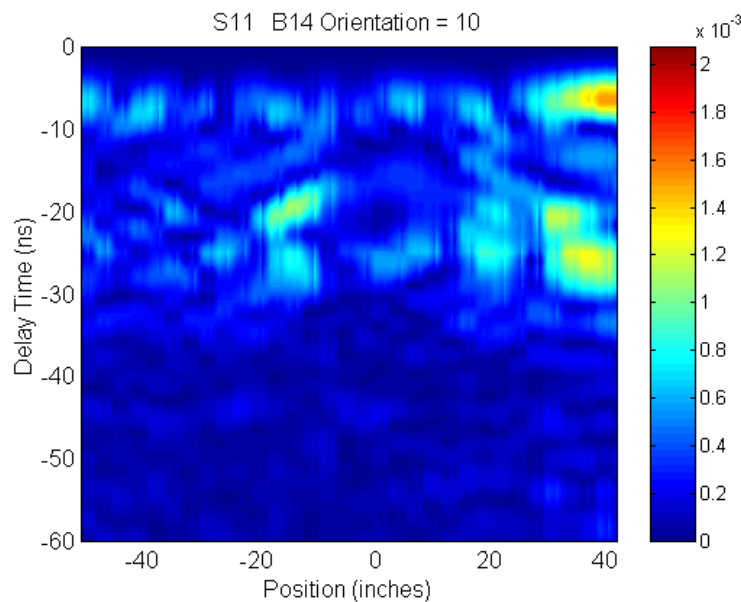
(c) S_{11} (transmitted and received signals both parallel to scan direction), as a function of antenna position, for 20 inch offset.

Figure 28   Classification features and position-time signal plot for a vertical MK23 bomb obtained from a 20-inch offset (28 inch diagonal) survey path.

4.3 UXO Classification Algorithm

The previous UXO classification algorithm utilized resonance and linearity features based on single position GPR data. Under such a criteria, the offset of shallow nonlinear objects caused false alarms. UXO's with large inclination angles were easily missed. This situation has been improved significantly after the introduction of spatial and scattering features obtained from multiple position data. Figure 29 shows the flow chart of the new UXO classification criteria.

The whole UXO classification procedure starts with an inspection of the spatial distributions of the extracted ELF, that is, of the ELF plotted as a function of antenna positions. If the ELF is low over most of the scan region (10 feet), it means the object is very likely a non-UXO object. If there are some regions of high ELF values, the next thing checked is whether high ELF values are observed in the middle region such as the one shown in Figure 11(a). If the answer is yes, then the object is very likely to be a UXO-like object with a small inclination angle. The corresponding ETO indicates the UXO orientation. If the ELF values in the middle region are low but high at offset regions (whether one side or two sides), the object could be a UXO with a larger inclination as shown in Figure 13(a) or a shallow non-linear, non-UXO object as shown in Figure 15(a), Figure 17 and Figure 19. The former could have a higher ELF due to oblique incidence. The latter produces a higher ELF because of coupling with the antenna arms. In either situation, ETO will indicate an orientation aligned with the scan direction in all passes as seen in Figure 13(b) and Figure 15(b) where the ETO's in both cases indicate an angle of – 90° that agrees with the scan direction, 273°.

A plate-like object, such as shrapnel, may show good resonance depending on its geometry and edges. However, the surface reflection from a horizontal plate-like object produces strong responses in both S_{11} and S_{22} channels, as demonstrated in Figure 18 above. On the other hand, a vertical UXO would have much weaker S_{22} responses as shown in Figure 12 because the field polarization is transverse to the UXO axis. This quite different S_{22} channel behavior allows one to discriminate a plate-like object from a vertical one without too much difficulty. It was also observed that the scattering

pattern in time-position plot under the initial arcs also shows a more complicated structure compared to a vertical UXO. This could be related to the different creeping waves propagating behind the plate.

A compact non-linear object such as a sphere is not a good resonator and can be discriminated by the large damping factor extracted from the natural resonance. This type of object also does not have the two arcs with different curvature as observed in Figure 20.

The classification criteria discussed above were found to be very effective in discriminating UXO-like targets for the lanes with known targets. Each of these criteria may be developed into automatic classification procedures using pattern recognition, image correlation or neural network training techniques. However, at present, Figure 29 is implemented by training an operator using a training set. The operator is then asked to make a classification decision by following the flow chart.
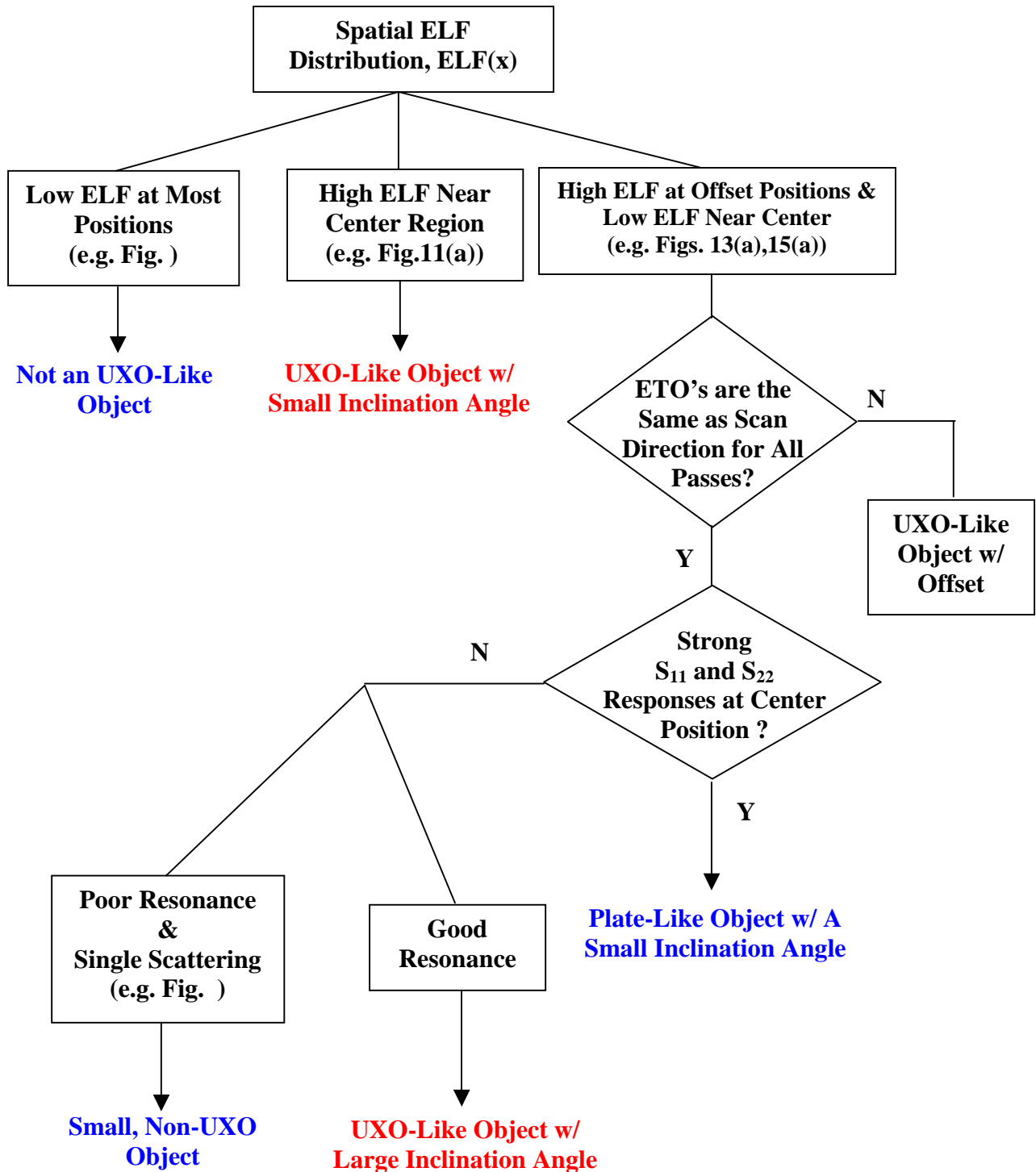
Figure 29.   Improved UXO classification flow chart.

Chapter 5 Blind Targets Classification Results Compared with Ground Truth

This section starts with the designation of UXO-like (or ordnance) and clutter (or non-ordnance) items. The overall classification performance will then be provided for both new and old lanes at the Blossom Point site. The whole target list is then broken down into three parts for further investigation: *correctly classified UXO-like items*, *missed UXO-like items* and *clutter items classified as UXO-like items*.

5.1 Designation of UXO-Like Items

Before we evaluate the classification performance, all the target items will be separated into UXO-like and clutter two categories. It should be noted that some non-ordnance items may have general elongated bodies like a typical UXO item regardless their different detail shapes, smoothness or curvature. Conductive cylinders or shrapnel strips are examples. This type of non-ordnance would show similar radar features under the practical frequency limitations and current classification criteria. Therefore, when an item has a length-to-diameter (L/D) ratio of three or greater, it is designated as an UXO-like item.

Table 4 lists the UXO-like/Clutter designation of the old Blossom Point items buried in lanes A~E, and Pictures of these items can also be found in Figure 30. Some "new" items were added to the site specifically for this demo, including standard ordnance and various odd pieces of scrap from exploded ordnance. These 11 scrap items are numbered here Sc1 through Sc11. Some of these bear cataloguing numbers from previous work, indicated on blue tags attached to each piece. One target (Sc4) consists of a cluster of pieces with tag numbers 12, 17, and 25. Vertical and horizontal views of these pieces are shown in Figure 31. Table 5 shows the UXO-like/clutter designation of the new Blossom Point items buried in the F~I lanes.

Table 4. UXO-Like/Clutter Designation of Old Blossom Point Items (Lanes A~E).

Item ID	Description	Classification	Reason
A	1.5"x3" solid steel cylinder	Clutter	L/D < 3
B	1.5"x 6" solid steel cylinder	UXO-Like	L/D > 3
C	1.5"x 12" solid steel cylinder	UXO-Like	L/D > 3
D	3"x6" solid steel cylinder	Clutter	L/D < 3
E	3" x 12" solid steel cylinder	UXO-Like	L/D > 3
F	3" x 24" solid steel cylinder	UXO-Like	L/D > 3
G	16 lb steel shotput	Clutter	Symmetric
H	4"x4"x0.25" steel plate	Clutter	Symmetric
J	8"x8"x0.25" steel plate	Clutter	Symmetric
K	1.5"x6"x0.25" steel plate	UXO-Like	L/D > 3
L	3"x12"x 0.25" steel plate	UXO-Like	L/D > 3
M	Mk 23 practice bomb	UXO-Like	UXO
N	81 mm Mortar	UXO-Like	UXO
P	BDU-33	UXO-Like	UXO
Q1	4"x 4"x0.25" Al plate	Clutter	Symmetric
Q2	2"x 8"x0.25" Al plate	UXO-Like	L/D > 3
Q3	Flattened Al soda can	Clutter	L/D < 3
Q4	Box fin (M 38)	Clutter	Not Linear
Q5	Box fin (M 38)	Clutter	Not Linear
Q6	Slip joint pliers	UXO-Like	L/D > 3
Q7	Al fins (2.75" rocket)	UXO-Like	L/D > 3
Q8	Shovel blade	UXO-Like	L/D > 3 (handle)
Q9	Banding material	Clutter	L/D < 3
Q10	Box fin assembly (M 38)	Clutter	Not Linear
Q11	Barbed wire	Clutter	Not Linear
Q12	Horseshoe	Clutter	Not Linear
Q13	8" round steel plate	Clutter	Symmetric
Q14	Twisted steel piece	Clutter	L/D < 3
Q15	Fence post cap	Clutter	L/D < 3
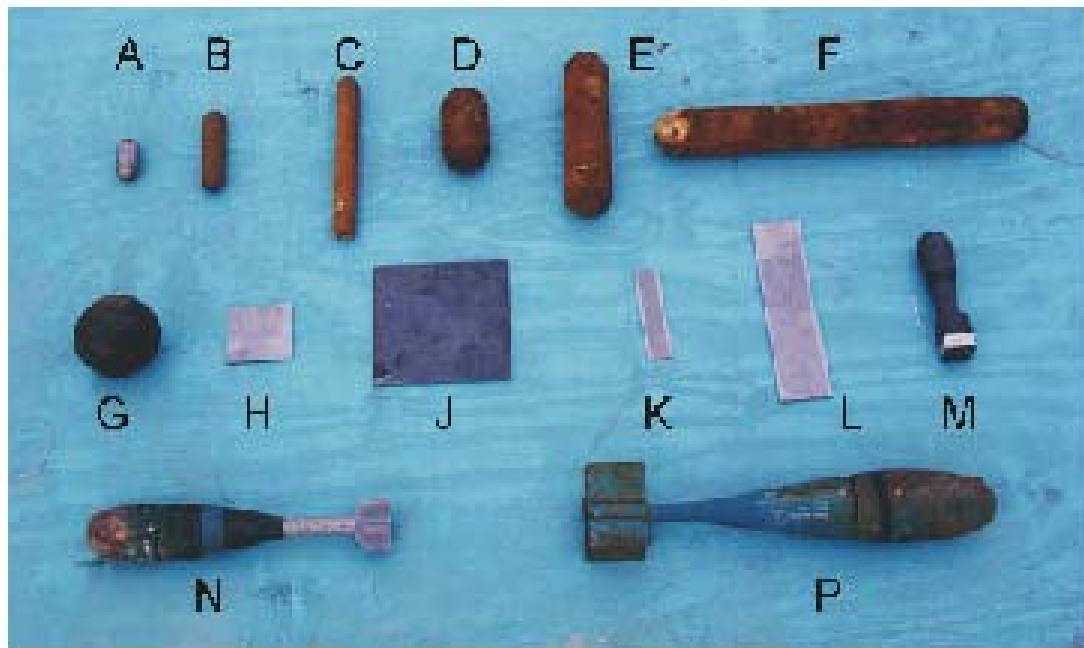
(a)

(b)

Figure 30. Pictures of the old Blossom Point items in lanes A~E. (a) calibration targets, (b) clutter items

Table 5. UXO-Like/Clutter Designation of New Blossom Point Items (Lanes F~I)

Item ID	Description	Designation	Reason
X1	60mm	UXO-Like	UXO
X2	60mm	UXO-Like	UXO
X3	60mm	UXO-Like	UXO
X4	60mm	UXO-Like	UXO
X5	60mm	UXO-Like	UXO
X6	2.75"	UXO-Like	UXO
X7	2.75"	UXO-Like	UXO
X8	2.75"	UXO-Like	UXO
X9	2.75"	UXO-Like	UXO
X10	81mm	UXO-Like	UXO
X11	81mm	UXO-Like	UXO
X12	81mm	UXO-Like	UXO
X13	BDU-33	UXO-Like	UXO
X14	120mm	UXO-Like	UXO
NX1	Steel Bar (L24"/D3")	UXO-Like	L/D > 3
NX2	Steel Bar (UXO Like L=same as 120mm, D1"	UXO-Like	L/D > 3
NX3	8"d steel plate	Clutter	Symmetric
NX4	8"d steel plate	Clutter	Symmetric
NX5	8"d steel plate	Clutter	Symmetric
Sc1	Whole crumpled box fin	Clutter	Not Linear
Sc2	box fin fragment	Clutter	Not Linear
Sc3	Projectile nose	Clutter	Not Linear
Sc4	Cluster of clutter items 25,17, &12	Clutter	Not Linear
Sc5	clutter Item #22	Clutter	Not Linear
Sc6	Clutter Item #3	UXO-Like	L/D > 3
Sc7	clutter Item #24	Clutter	Not Linear
Sc8	clutter Item #18	Clutter	Not Linear
Sc9	clutter Item #23	Clutter	Not Linear
Sc10	clutter Item #11	UXO-Like	L/D > 3
Sc11	clutter Item #16	UXO-Like	L/D > 3

Sc6, Sc10, and Sc11 are all clutter items that are designated as UXO-like because of their L/D ratio greater than three. Pictures of each item numbered Sc1 thru Sc11 can be seen below.

Figure 31   Pictures of the new Blossom Point items in lanes F~I.

5.2 Overall Classification Performance

The following three parameters are used to evaluate the overall classification performance. The **True-UXO-Rate (TUR)** is defined as

TUR = [Number of UXO-like items classified as UXO-like] **/** [Number of UXO-like items]

The False-UXO-Rate (FUR) is defined as

FUR = [Number of clutter items classified as UXO-.like] **/** [Number of clutter items]

The True-Clutter-Rate (TCR) is defined as

TCR = [Number of clutter items classified as clutter] **/** [Number of clutter items]

Notice that *FUR+TCR=100%* and TCR is directly related to the cost reduction for the clearance task. The risk factor, or the UXO-like that are not classified correctly can be obtained from *(1-TUR)*.

Figure 32 plots the TUR, FCR and TCR for three different thresholds based on the confidence levels (see Table 6) for all the targets measured at the Blossom Point site. These targets include the old items buried in lanes A thru E and the new items selected by CRREL/ OSU team buried in lanes F thru I. The leftmost group in the figure neglects of the confidence levels and is solely determined by whether the item is classified as UXO-like or not. The middle group includes only those UXO-like items that have moderate or high confidence levels as UXO-like items. All other items are classified as clutter items. The rightmost group includes only those UXO-like items that have high confidence levels as UXO-like items. Although more than 75% of UXO-like items were correctly classified as indicated by the (TUR), further improvement is needed. The number of clutter items that were classified as UXO-like is approximately 48% as indicated by FUR. Both TUR and FUR can be further improved as will be address in next section.

It was apparent during the data processing that the lanes containing the new targets suffered from much higher surface clutter caused by recent soil disturbance. It was also apparent during the demonstration that there were many parallel linear trenches running in the north-south and east-west directions. The trenches oriented in the north-south direction have a width of approximately 14 inches. The east-west trenches are narrower. These trenches could be caused by the extraction of previous drainage or irrigation pipes installed while the site was still a farmland. The new items also contain more target orientation variation. With these factors in mind, it is revealing to examine classification performance for old items and new items separately. Figure 33 plots the TUR, FUR and TCR for old Blossom Point items buried in lanes A thru E. All of these items are either horizontal or vertical. The classification results without using any threshold shows amazingly that only one UXO-like item is missed! The FUR is lower compared to the previous case but is still 45%. The classification results for the new target items alone are shown in Figure 34, indicating a much poorer performance. It should be noted that there are 39 UXO-like items and 22 clutter items in the old lanes. There are 19 UXO-like items and 11 clutter items in the new lanes. The following sections will investigate further the issues of high FUR and missed ordnance. These results include the known targets located at Rows 13~15 in Lanes A~E. During the classification, the operator did not pay any attention to whether a target was known or unknown and performed classification solely based on classification features. While inclusion of the calibration targets in the scoring may be regarded as suspect, note in Figure 33 and Figure 36 that the histograms for the old lanes are similar whether or not the calibration targets are included.   Note that the known targets are only located in the old lanes. Therefore the statistics for new lanes are not affected by inclusion or deletion of data from the cal lanes.
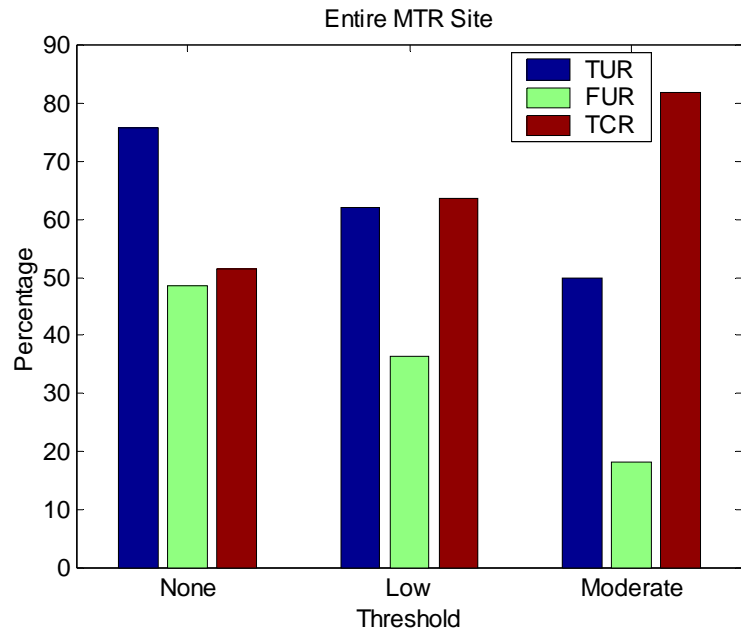
Figure 32. **The classification performance for all targets buried at the Blossom Point site considered together (old ones lanes A~E and new ones lanes F~I), including calibration targets treated as unknowns.**
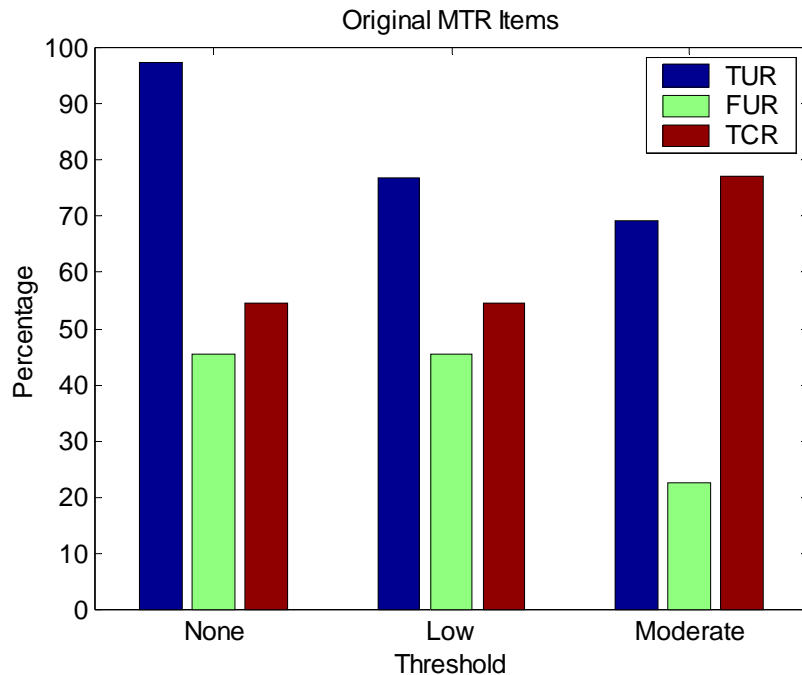
Figure 33 **Classification performance for the old targets alone (A~E lanes) buried at the Blossom Point site, including calibration targets treated as unknowns.**
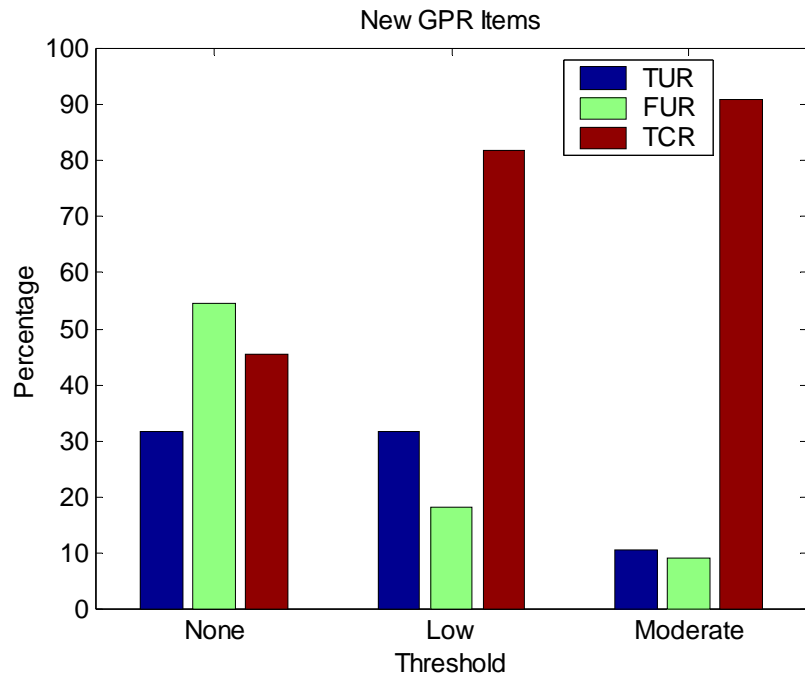
Figure 34. The classification performance for the new targets (F~I lanes) buried at the Blossom Point site.
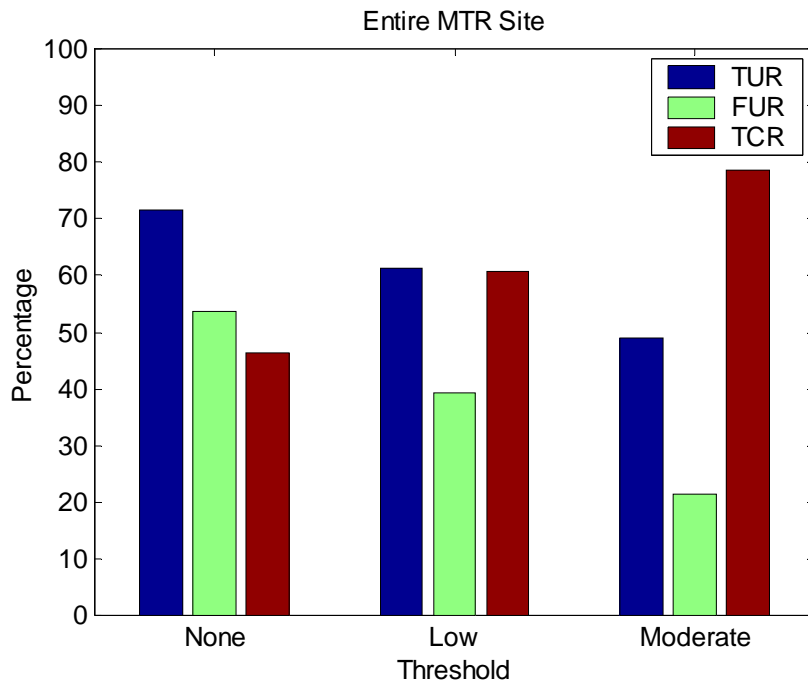
Figure 35. The classification performance for all lanes excluding the calibration targets.
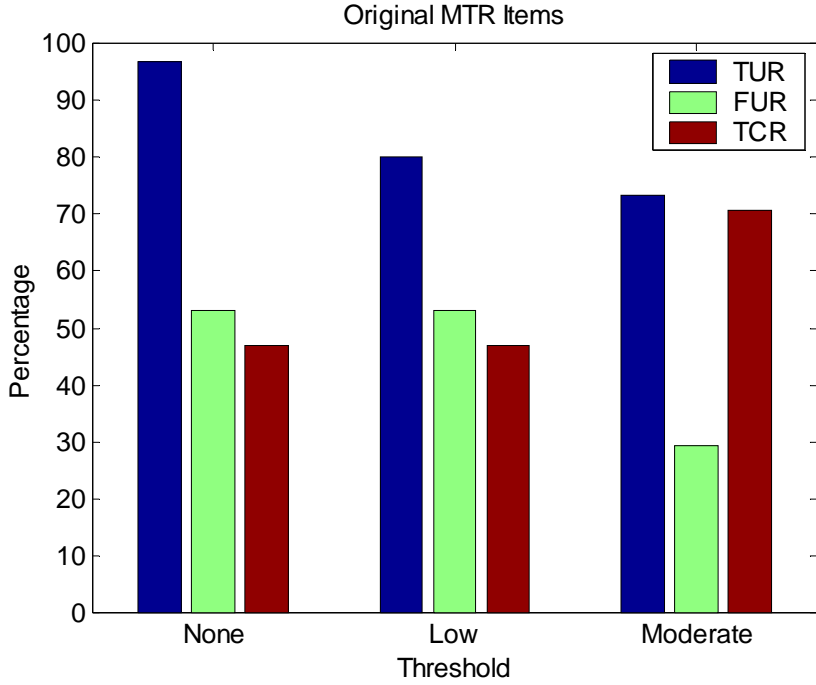
Figure 36.   The classification performance for the old lanes excluding the calibration targets.

5.3 Correctly Classified UXO-like Items

Table 6 lists the correctly classified UXOs, i.e. TUR items in comparison with the ground truth information provided by NRL. The last column indicates the signal-to-clutter ratio SCR obtained from the measured data. The signal level of the SCR was selected from the maximum eigenvalues associated with the selected target among different channels and positions. The clutter level was determined from the eigenvalues obtained from the empty-site data using exact the same processing procedures and parameters used in obtaining the signal level.

First, let's compare the estimated depths with their true values as shown in Figure 37. A general agreement for most targets is observed. Items A13, B7, C13, D4, D11 and I8 are the ones that have greater depth discrepancy. These are also highlighted in Table 6. Notice the large discrepancies

observed for items I8 and D4. Both items are vertical UXO-like items buried relatively deep (one meter). The combination of weak scattering from this orientation as well as the soil absorption caused the responses to be weak compared to the background clutter level. From the estimated depths (DEP), it is obvious that the processing actually picked up surface anomalies in preference to the target responses. At this particular target location, there was also a linear trench running approximately south-north, that was confirmed by the GPR data and a log taken at the site. This type of trench will give a stronger S22 response and result in a linear feature with an orientation perpendicular to the trench direction. This is confirmed by the estimated orientations (ETO) obtained from these two items. It is also interesting to notice that all of these targets have either low or moderate confidence levels and relatively low signal-to-clutter ratio (SCR). Thus, while erroneous classification results were obtained, the system indicated that the results should be regarded with suspicion. Further, while the processing missed targets that were present, it was correct in the sense that it classified signals from non-targets as non-UXO. This motivates us to believe that the results can be improved by integration of non-GPR data on depth estimations, so that selection of appropriate time regions is more likely to occur in the processing. In the least, it will be worth it to segregate cases such that deeper and shallower signals can be treated separately.

The estimated lengths are compared with true lengths in Figure 38. Recall that length estimation was obtained from the natural resonance frequency. The error sources of length estimation include incorrect resonant frequency estimation and soil property variation. The error in natural resonant frequency estimation could result from low signal to clutter ratio and selection of inappropriate time regions as "late-time."   The length estimations for most selected UXO-like items are close to their true values. The items that have greater length discrepancy are B7, B9, C13, D4, D11, D13, E2, E14 and I13 as also highlighted in Table 6. It is not surprising that B7, C13, D4 and D11 have larger length estimation errors as their depths were estimated incorrectly and they all have low confidence levels. Item D13 and E14 have similar lengths (~0.6m) and seem to have similar underestimation of the lengths. The lengths of items B7, C13, D4 and D13 are all greatly underestimated. This could be explained by the fact that they all had vertical orientations and the higher resonant modes were excited more strongly than the fundamental mode (half-wavelength mode used for length estimation) due to the oblique incidence. This resulted in overestimation of the resonant frequency, which in turn caused the target length to be underestimated. From examination of the scattering patterns over space, it appears that such an

underestimation is more likely for longer objects, as the incident angle gets closer to the ordnance axis direction. Therefore, it may not be practical to estimate the length of vertical ordnance accurately unless it is shallow and the soil is not too absorptive.

Figure 39 compares the estimated target orientations with the true orientations, for orientable targets. Since the orientation of a vertical item does not have much meaning, all vertical items have been excluded from this figure. An excellent orientation agreement is observed. Only item C8, D3. I5 and I13 show error greater than 15°.

Table 6 List of correctly classified UXO-like items.

TAR#	Confidence Level	Est. Length (m)	True Length (m)	Est. Depth (m)	True Depth (m)	Est. Angle (+/-180°)	True Azimuth (°)	True Dipping (°)	SCR
A1	H	0.536	0.51	0.297	0.35	-174	0	0	48.46
A2	H	0.371	0.25[1]	0.231	0.23	-177	0	0	64.40
A3	L	0.165	0.305	0.326	0.5	93	0	90	23.82
A4	H	0.540	0.51	0.398	0.5	-179	0	0	54.95
A5	H	0.276	0.305	0.348	0.35	180	0	0	39.52
A7	H	0.258	0.305	0.464	0.5	-176	0	0	30.52
A12	M	0.164	0.152	0.297	0.1	84	0	90	48.99
A13	M	0.448	0.6	0.246	0.75	12	0	90	21.80
B2	M	0.277	0.254	0.529	0.15	-173	0	0	43.57
B4	H	0.346	0.305	0.326	0.35	18	0	90	34.28
B7	L	0.255	0.61	0.246	0.75	-163	0	90	20.96
B9	H	0.750	0.305	0.260	0.35	176	0	0	65.17
B10	H	0.293	0.254	0.268	0.25	-175	0	0	35.12
B12	H	0.280	0.305	0.180	0.15	178	0	0	48.93
B14	H	0.197	0.254	0.202	0.25	-94	0	90	29.01
B15	H	0.381	0.305	0.289	0.25	-8	0	0	43.52
C1	H	0.190	0.305	0.406	0.5	11	0	0	36.75
C4	H	0.220	0.152	0.239	0.2	11	0	90	21.00
C6	H	0.183	0.152	0.151	0.1	7	0	0	38.82
C8	L	0.193	0.152	0.101	0.05	58	90	0	47.84
C13	L	0.137	0.305	0.195	0.5	-92	0	90	32.10
C15	H	0.152	0.152	0.253	0.2	0	0	0	43.33
D2	H	0.302	0.305	0.246	0.15	96	0	90	53.02
D3	H	0.325	0.305	0.231	0.25	-132	90	0	66.09
D4	L	0.174	0.61	0.021	1	95	0	90	17.03
D5	H	0.263	0.254	0.202	0.15	9	0	90	36.90
D7	H	0.350	0.305	0.326	0.25	43	0	90	79.78

[1] Handle part only.

D11	L	**0.303**	**0.61**	**0.667**	**1**	-175	0	0	31.45
D12	H	0.292	0.25	0.115	0.1	-177	0	0	73.96
D13	H	**0.116**	**0.51**	0.340	0.35	-87	0	90	32.61
D14	L	0.303	0.305	0.202	0.35	-91	0	90	22.05
E2	H	**0.363**	**0.6**	0.529	0.75	-175	0	0	45.50
E3	H	0.185	0.203	0.130	0.05	-171	0	0	68.51
E9	H	0.185	0.15	0.159	0.05	-172	0	0	53.05
E10	H	0.389	0.305	0.188	0.15	-127	90	0	53.18
E12	H	0.188	0.152	0.108	0.05	179	0	0	44.16
E14	H	**0.153**	**0.61**	0.631	0.75	-9	0	0	50.55
E15	L	0.243	0.152	0.246	0.08	-89	0	90	17.88
*I4	H	0.295	0.23	0.420	0.25	175	0	0	69.40
*I5	M	0.206	0.23	0.515	0.5	29	45	30	19.30
*I8	M	0.210	0.23	**0.057**	**1**	81	0	90	22.95
*I9	M	0.160	0.42	0.311	0.25	5	0	30	23.76
*I10	M	0.307	0.42	0.108	0.5	13	0	45	15.42
*I13	H	**0.364**	**0.51**	0.355	0.25	23	0	30	50.95

*F to I lanes are new sites containing new GPR targets.
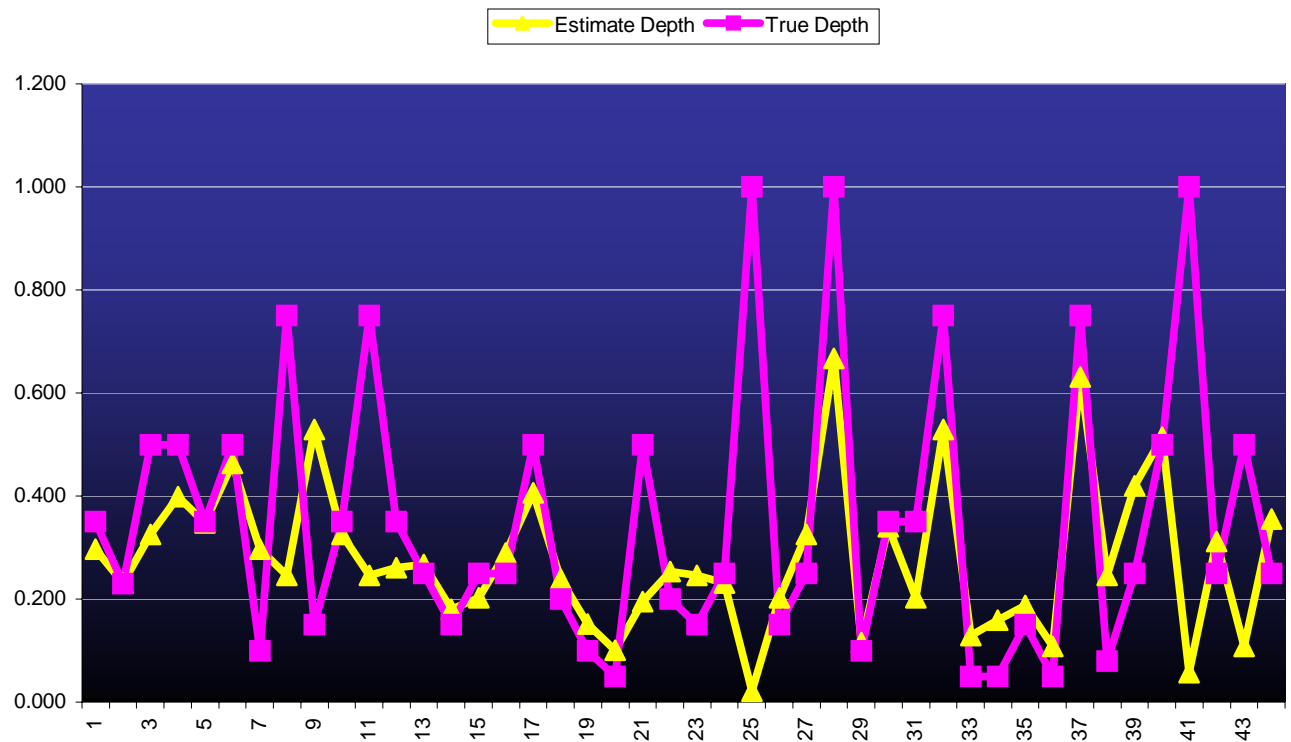
Figure 37.   Comparison of estimated depth and true depth of correctly classified UXO-like items.
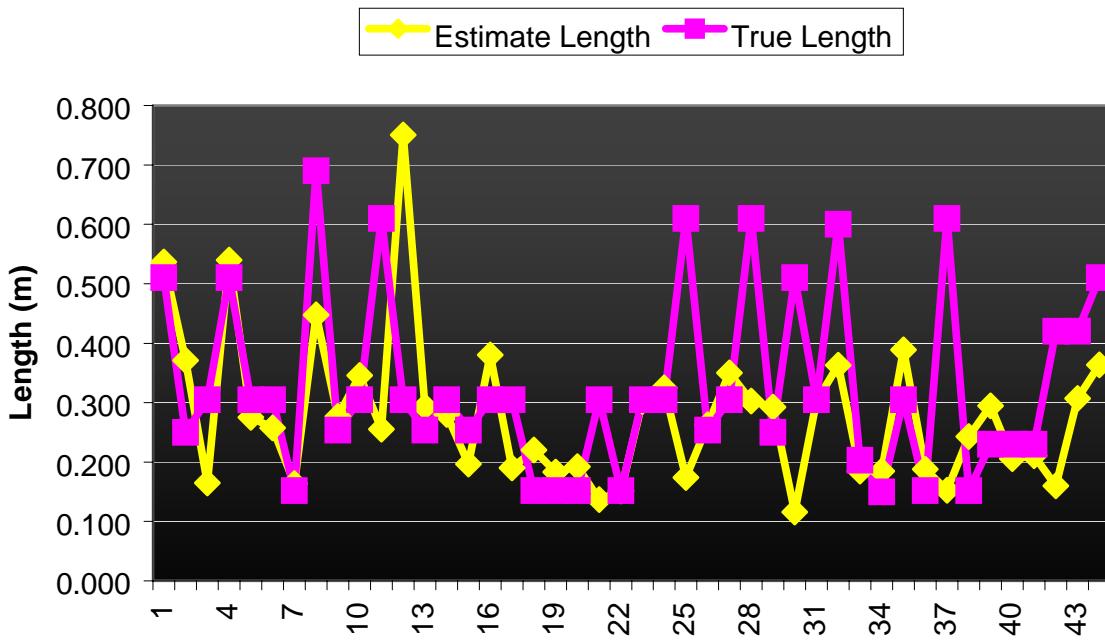
Figure 38. Comparison of estimated length and true length of correctly classified UXO-like items.
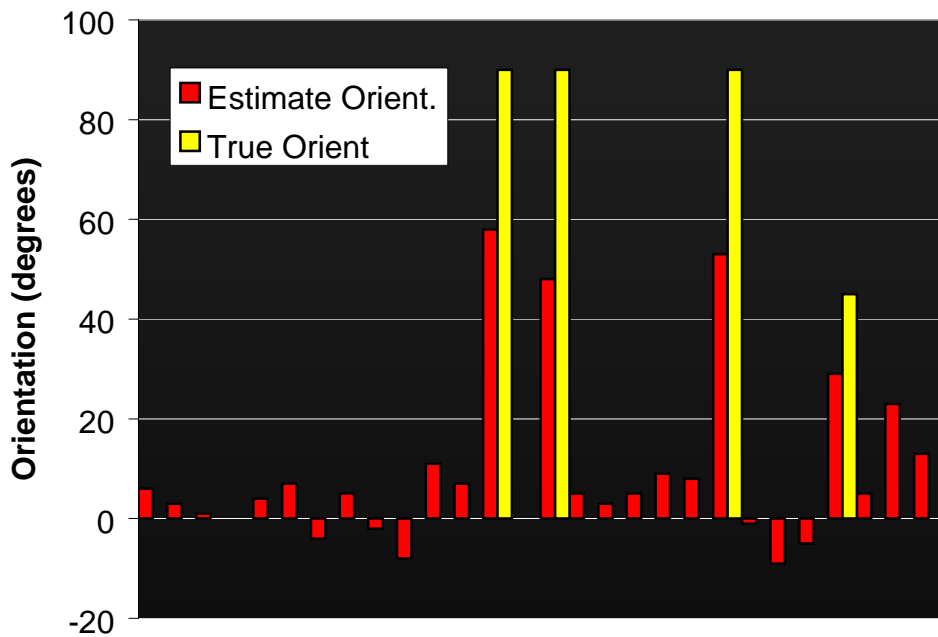
Figure 39. Comparison of estimated orientation and true orientation of correctly classified UXO-like items

5.4 Missed UXO-like Items

Table 7 lists the missed UXO-items to be analyzed in more detail. It is interesting to note that only one vertical UXO (B3) in old lanes was missed out of 39 UXO-like items and 22 clutter items. Also notice that the estimated depths for most of the missed UXO-like items are very close to surface. This is probably due to the weakness of the true target response so that the surface anomalies were mistakenly selected as the target responses. This certainly is the case for F6, F7, G7, I6, I7 and I12 (highlighted in Table 7) since they were all small items and were buried relatively deep. The responses of items H4 and H5 were virtually indistinguishable from the background clutter.

B3, I11 and I14 were found to show UXO-like features and should be reclassified as UXO-like items after choosing the correct time range corresponding to the true depth. The data collected from the new lanes at the Blossom Point site showed significantly stronger ground surface scattering compared to those collected at the old lanes. For several weak targets, the predicted depth clearly indicated that we have selected the surface clutter instead of the targets responses. In a sense, this is a "good" because we have classified this surface scattering as non-UXO!

Table 7 List of missed UXO-like items.

TAR #	Confidence Level	Est. Depth (m)	True Depth (m)	Est. Orient. (+/-180°)	True Azimuth (°)	True Dipping (°)	True Length (m)	Ground Truth ID	SCR
B3	H	0.035	0.5	92	0	90	0.66	N0305004	-8.69
*I11	H	0.071	0.5	-85	90	60	0.42	2.75"	12.24
*I14	H	0.028	0.5	4	45	45	0.51	81mm	12.86
*F6	M	0.057	0.5	175	45	60	0.3	clutter Item #11(Sc10)	8.14
*F7	H	0.079	0.5	5	45	45	0.4	clutter Item #16(Sc11)	-5.58
*G7	H	0.064	0.5	85	0	90	0.33	clutter Item #3 (Sc6)	-7.14
*I6	H	0.064	0.75	153	90	30	0.24	60mm	25.66
*I7	H	0.064	0.75	-1	90	45	0.24	60mm	-15.45
*I12	M	0.057	0.75	171	45	75	0.42	2.75"	5.32
*H4	H	0.057	1	127	45	30	0.69	BDU-33	0.65
*H5	M	0.159	1	84	45	60	0.75	120mm	10.33
*H6	H	0.086	0.75	42	0	30	0.61	Steel Bar (L24"/D3")	9.35
*H7	H	0.086	0.75	82	90	45	0.75	Bar L=same as120mm	23.21
*I15	H	0.064	0.75	-6	90	60	0.51	81mm	11.57

* New lanes.

5.5 Clutter Classified as UXO-like Items

A list of clutter items that were classified as UXO-like objects is provided in Table 8. Further investigations of these cases is summarized below.

Table 8   List of clutter classified as UXO-like items

TAR#	Confidence Level	Est. Depth (m)	True Depth (m)	Est. Orient. (+/-180°)	True Azimuth (°)	True Dipping (°)	Ground Truth ID
E8	H	0.035	0.08	-173	0	0	Q1500800(Fence Post Cap)
C2	H	0.057	0.10	-170	0	0	Q1101000 (Barbed Wire)
C11	M	0.457	0.10	7	0	0	Q0901000(Banding Material)
A9	H	0.166	0.25	-172	0	90	8"x8"x1/4" Plate
*H11	M	0.042	0.25	-151	Arbitrary	Arbitrary	crumpled box fin (Sc1)
C9	M	0.420	0.05	9	0	0	Horse Shoe
D1	H	0.558	0.10	119	0	0	Q0501000(Box Fin Piece,M38)
D8	H	0.558	0.15	103	0	0	Q1001500(Box Fin M38)
*H8	H	0.144	0.30	7	Arbitrary	0	8"d steel plate
*H12	L	0.042	0.50	-1	0	0	box fin fragment (Sc2)
*H9	L	0.050	0.50	89	Arbitrary	45	8"d steel plate
*F5	L	0.086	0.75	6	90	0	Bomb Shrapnel (Sc9)
*G9	L	0.057	0.50	177	90	0	Bomb Shrapnel (Sc8)
B13	M	0.137	0.10	-84	0	90	3"x6" Solid Cylinder
A6	M	0.071	0.03	-173	0	0	Side Crushed Coke Can
C10	M	0.079	0.05	11	0	90	4"x4"x1/4" Plate

*New lanes.

E8, C2 and C11 - UXO-like geometries. Figure 42 shows the classification features for Item E8. In this and the following figure, "transverse" indicates perpendicular to the survey pass direction, and "parallel" indicates aligned with it. All the features indicate an UXO-like item based on current classification rules. Although C2 (barbed wire) and C11 (banding material) do not appear to have a L/D ratio of three or greater from the picture, each individual thread does have a thin conducting body. Since they are bundled such that all threads have similar orientations, the radar responses show very good linear and resonant signatures.

A9 & H11 – New Classification Features

Figure 43 shows the classification features for Item A9, an 8"x8" vertical plate, when the scan direction is transverse to the top edge orientation. High ELF values were observed near the center location. However, unlike a true UXO-like item, the S11 responses are very weak near the center location. This feature apparently was not included in the existing classification rules shown in Figure 29. It should be noted that there was no vertical plate in the calibration lanes at the Blossom Point site. Near the center location the polarization of S11 is orthogonal to the edge and thus produces much weaker response than S22 channel. Furthermore, we expect the S11 responses at the offset positions to become weaker, for shallow burial, due to the cancellation between the diffraction from the top and the bottom edges. The intensity of the S22 response (parallel to the plate orientation) decreases in proportion to the narrowness of the target's top edge. Therefore, for a smaller vertical plate this pattern will be quite difficult to detect. Based on this finding, the classification rules shown in Figure 29 need to be modified as shown in Figure 40.

There were three passes collected for the target in cell H11. Two of the orthogonal passes showed no UXO-like features. The third pass showed features similar to a vertical plate as shown in Figure 44. Like A9, such features led to a UXO-like classification at the time of blind classification. On the basis of the modified classification rules below, H11 would have been classified as not UXO-like.
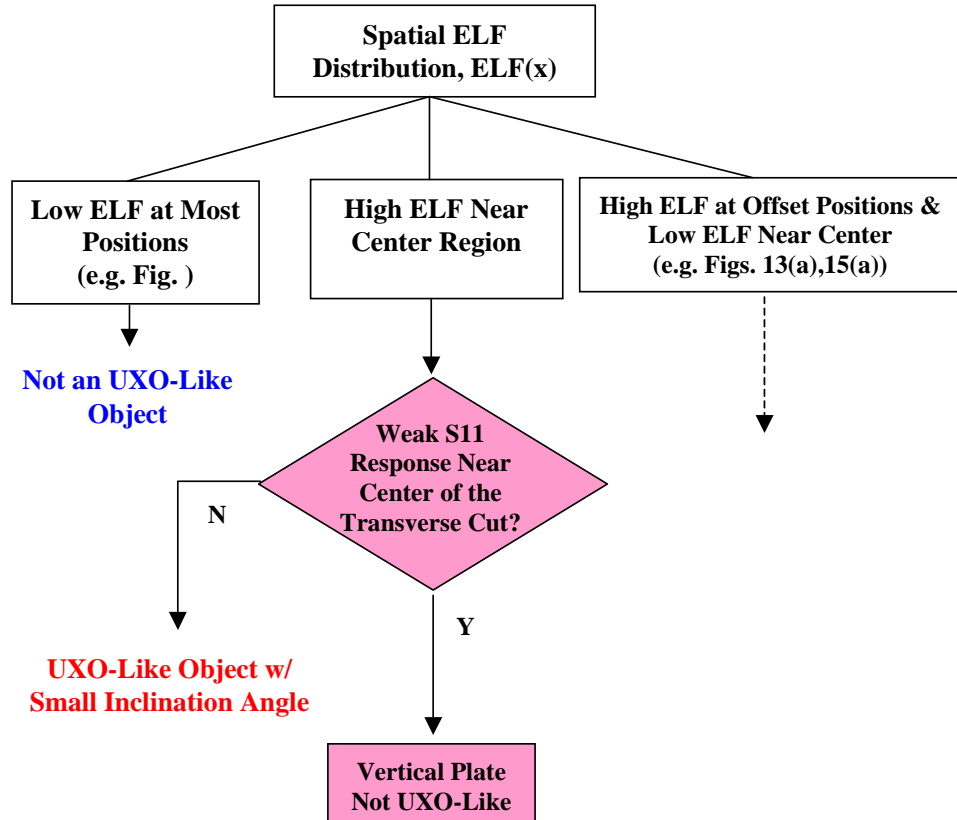
Figure 40. Modified classification rules to include features from vertical plates.

C9 – New Classification Features

Figure 45 shows the classification features (ELF and ETO) obtained from Item C9, a horseshoe. What is interesting about this item is that it is a good resonator regardless of excitation polarization. High ELF was observed as for an UXO-like item without a large depression angle. However, the ETO is always the same as the scan direction, which makes the inference of target linearity suspicious. Again, this peculiar feature was not included in the original classification features and led to UXO-like classification.
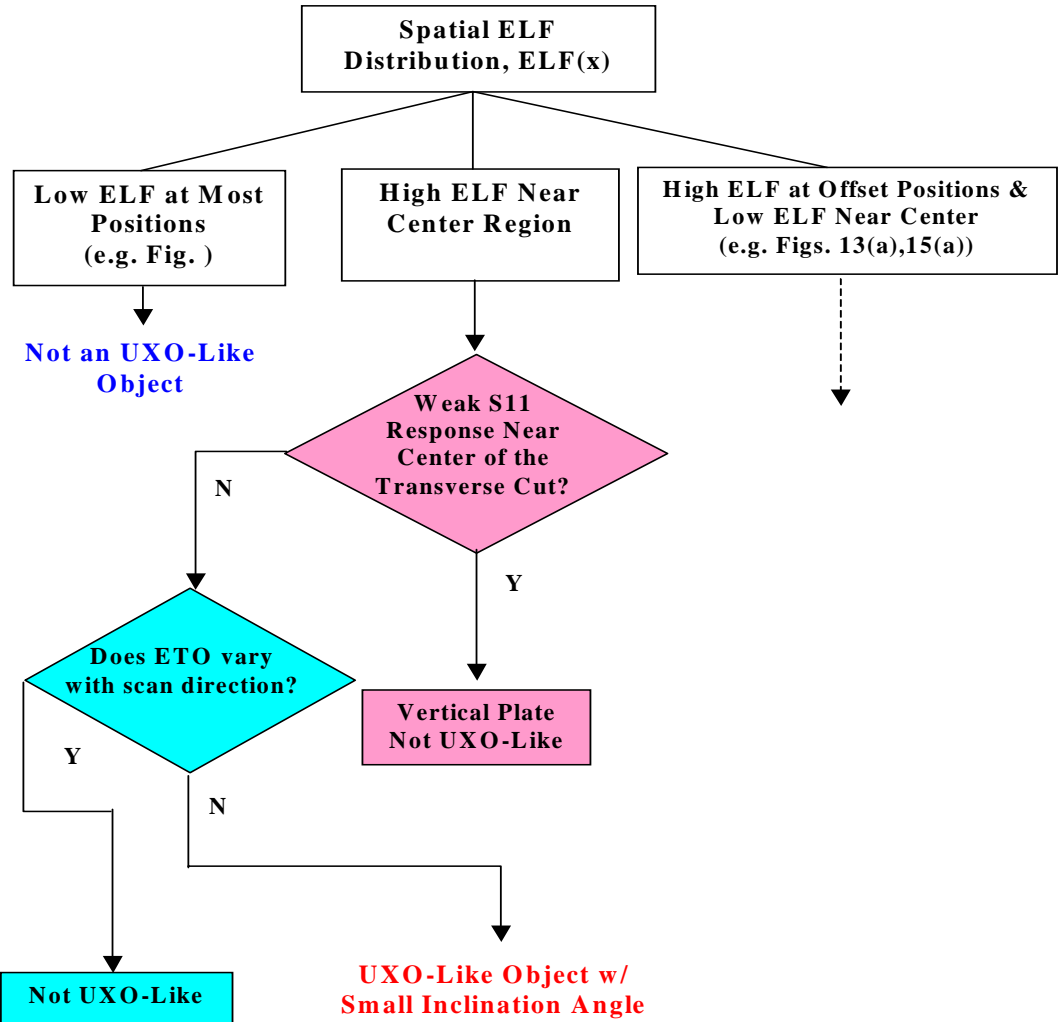
Figure 41.   Modified classification rules to include features from broken loops and vertical plates.

D1, D8, H8 and H12– Their classifications shown from

Figure 46 to

Figure **49** indicate horizontal plate features (See Section 3.2). The poor SCR of H12 resulted in a low

confidence level.

H9, F5, G9 and B13 – The classification features of these items show high ELF regions but cannot be

confirmed from spatial scattering pattern due to low SCR. Features of B13 provide Figure 50 as an

example. The other orthogonal cut is contaminated by a linear trench near the target location and could

not be used.

C10 & A6– Contaminated by linear trenches. A linear trench (near position –35 inches in Figure 51) located near the target makes the already weak target response even harder to discriminate. In fact, the trench was mistaken as the target and thus resulting in linear features.

In summary, 8 out of 17 mis-classifications of clutter items as UXO-like could have been avoided with the inclusion of the additional classification rules, shown in   Figure 41. This means a almost a 50% reduction of false-UXO-rate (FUR) in Figure 32.

(a)
Estimated linearity factor
ELF

(b) Parallel co-polarized responses.

(c) Transverse co-polarized responses
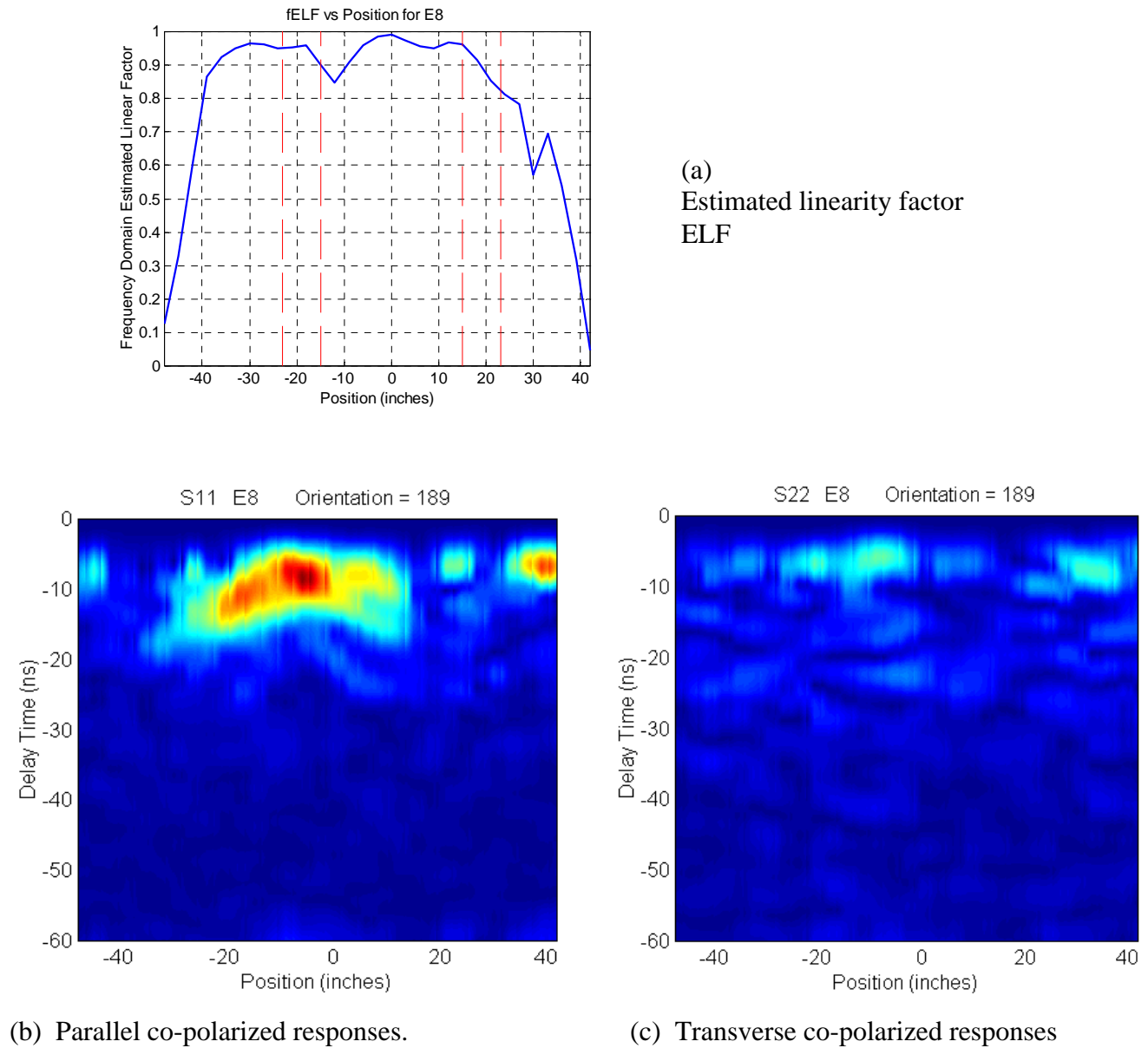
Figure 42.   Classification features for Item E8 (fence post cap) from survey line parallel to target orientation, for fence post cap.
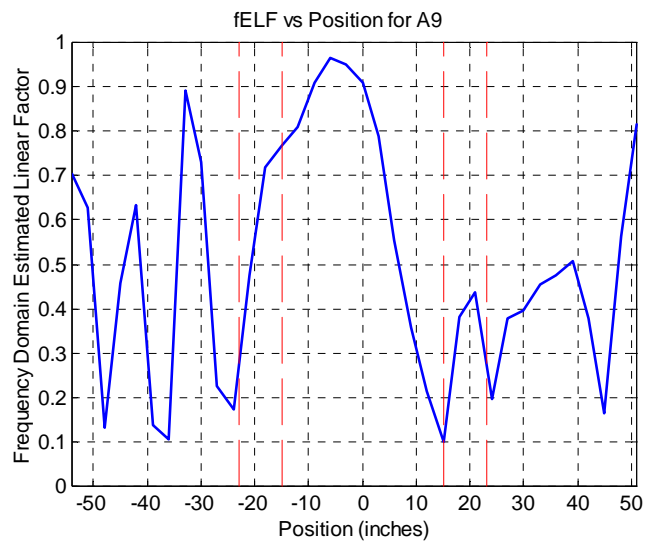
(a)
Estimated
Linearity
Factor
(ELF)
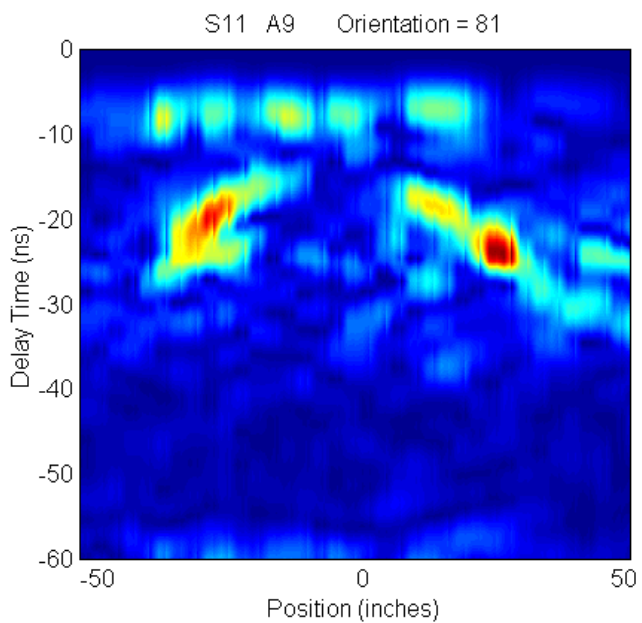
(b) S11 Response, perpendicular to plate orientation
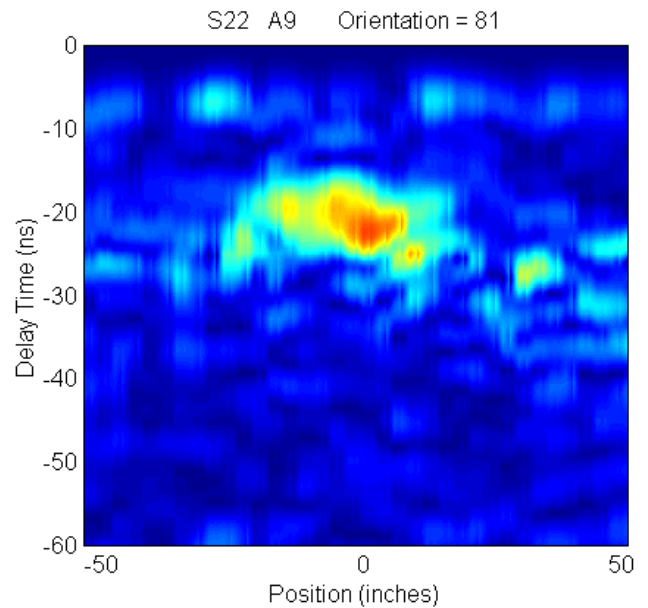
(c) Transverse Responses (S22 component, parallel to plate orientation)

Figure 43 **Classification features for Item A9 (vertical plate) obtained from a pass orthogonal to top edge direction of the plate.**

(a)
Estimated
Linearity
Factor
(ELF)

(b) Parallel co-polarized responses.

(c) Transverse co-polarized responses.
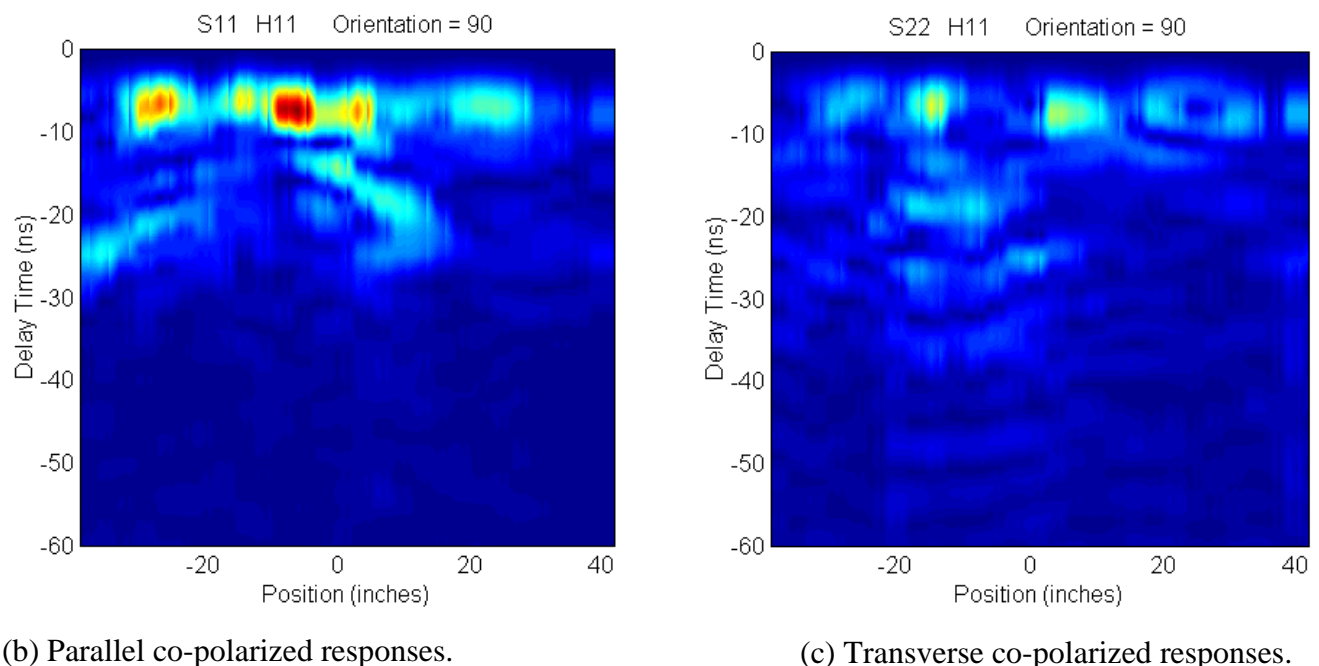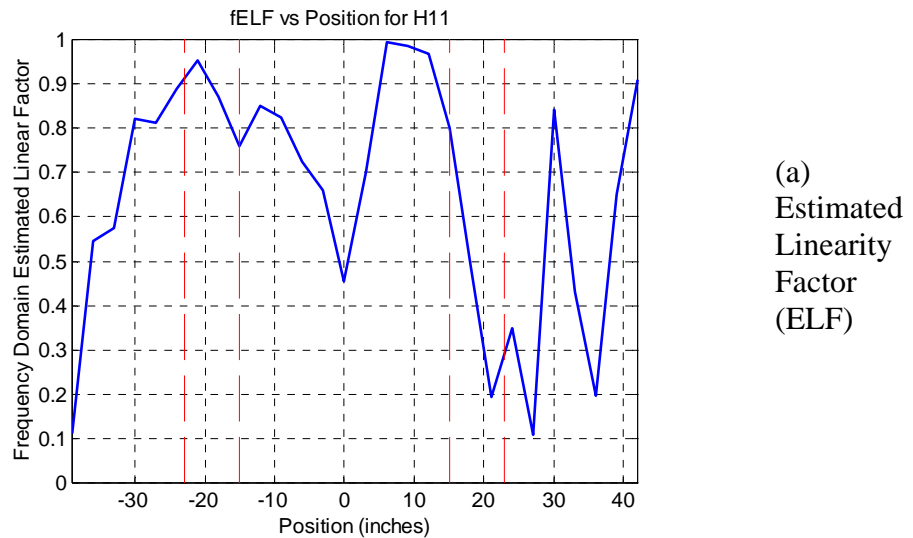
Figure 44   Classification features for Item H11 (crumpled box fin) from an offset cut.
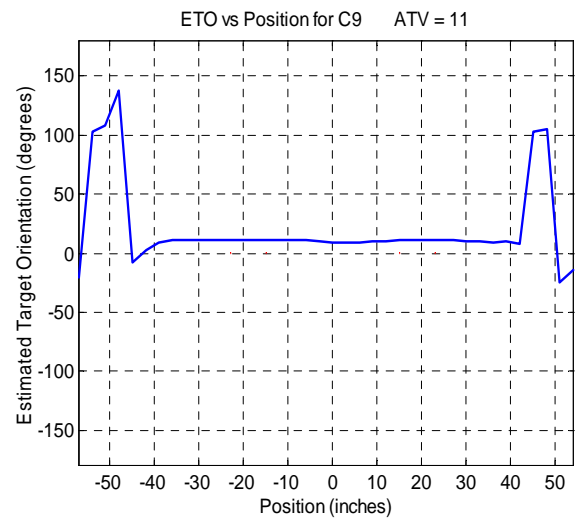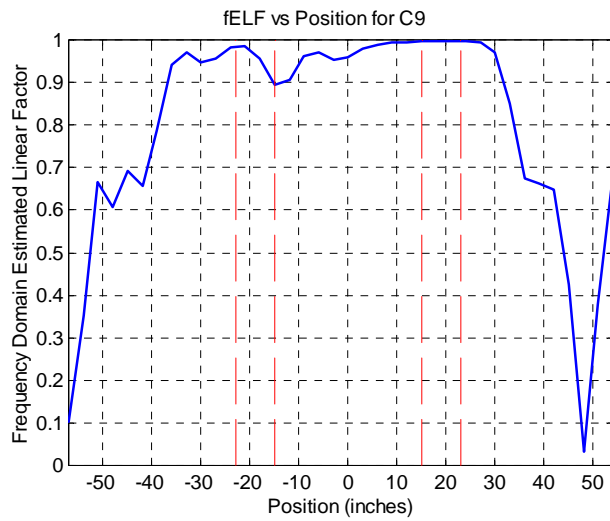
(b) Estimated target orientation (ETO) from parallel survey pass.
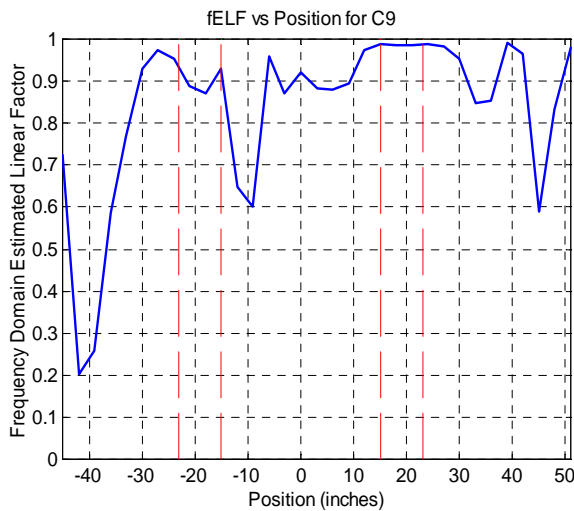
(c) ELF from the parallel survey pass.
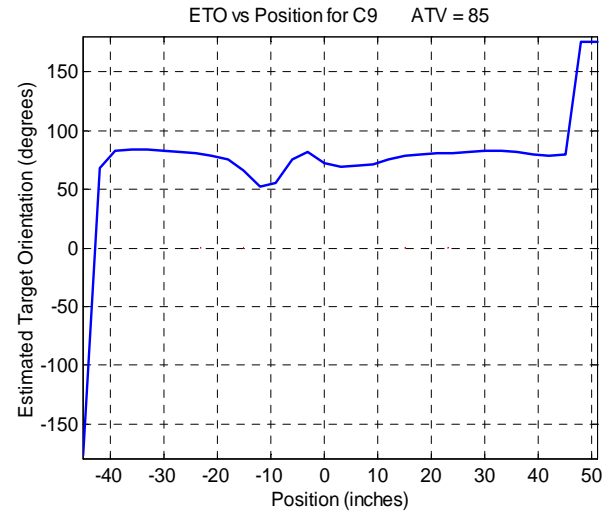
(d) Estimated target orientation (ETO) from the orthogonal survey pass.

Figure 45   Classification features for Item C9 (horse shoe).

(a) Estimated Linearity Factor (ELF)
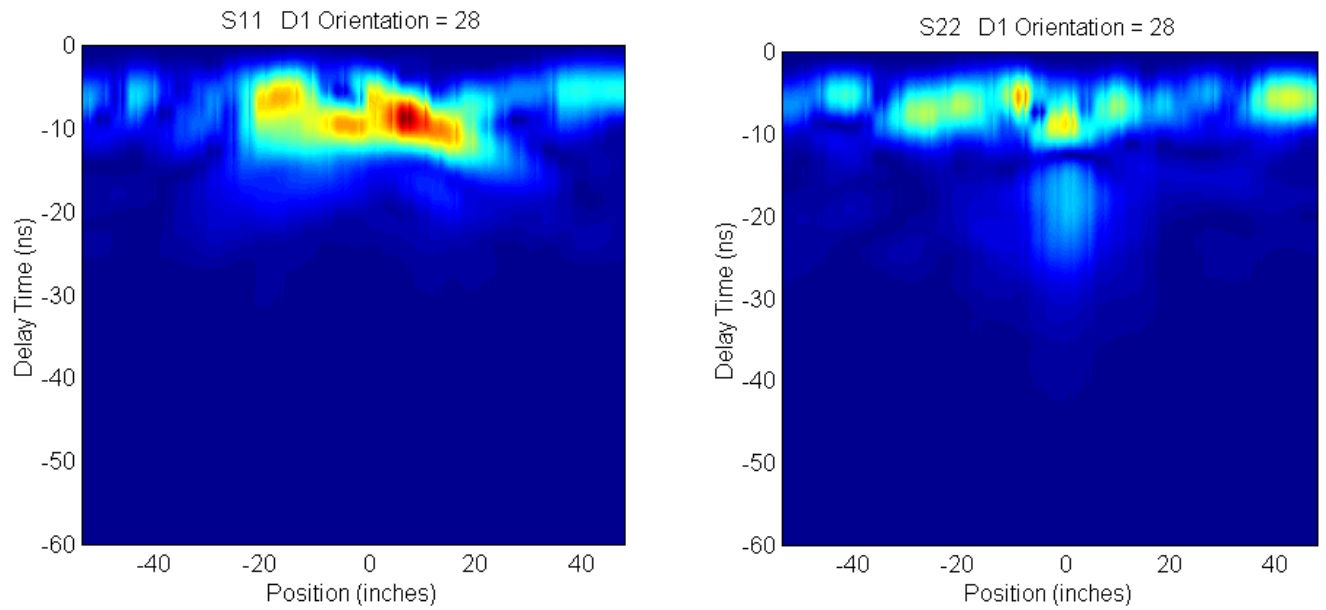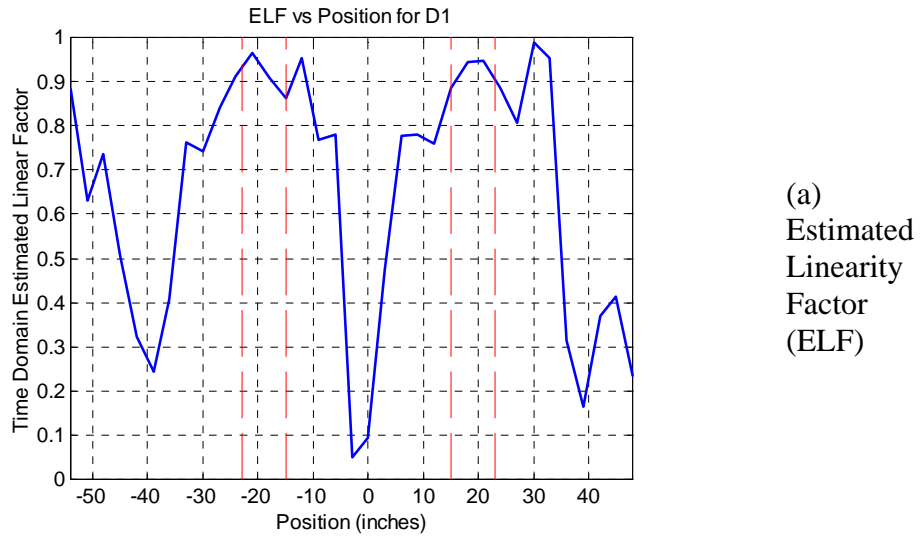
(b) Co-polarized response parallel to pass.

(c) Transverse co-polarized response.

Figure 46   Classification features for Item D1 (M38 box fin piece) from pass parallel to target orientation.

(a) Estimated Linearity Factor (ELF)

(b) Co-polarized response parallel to pass.

(c) Transverse co-polarized response.
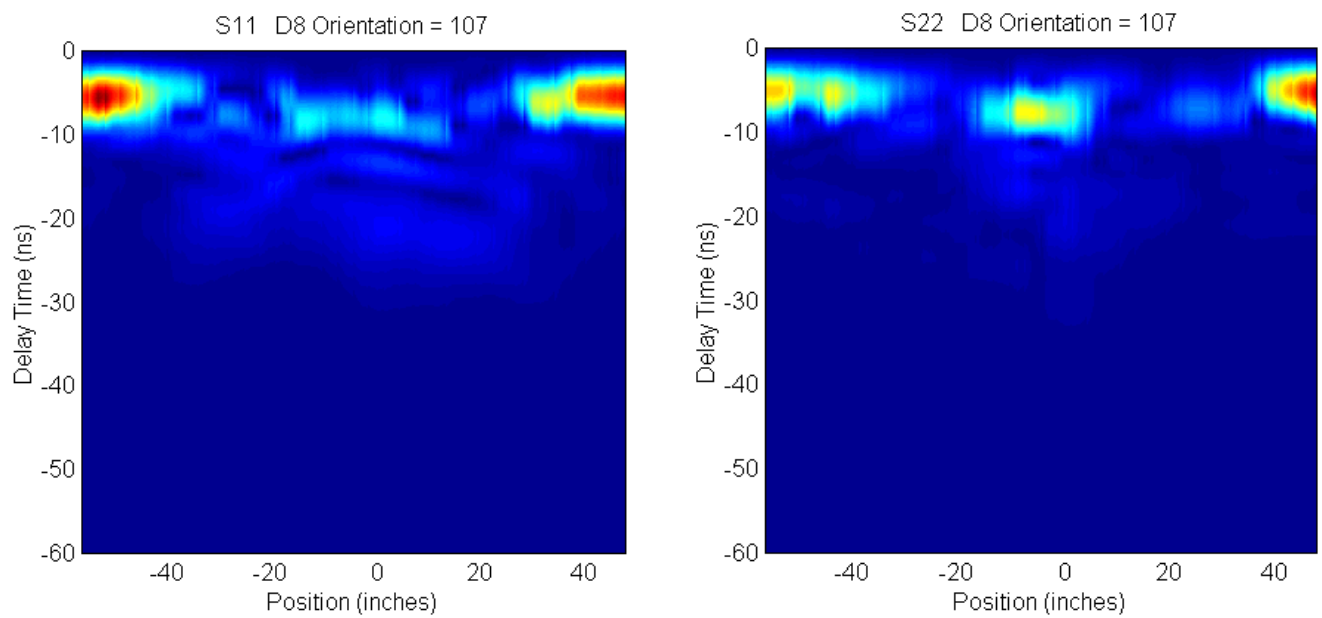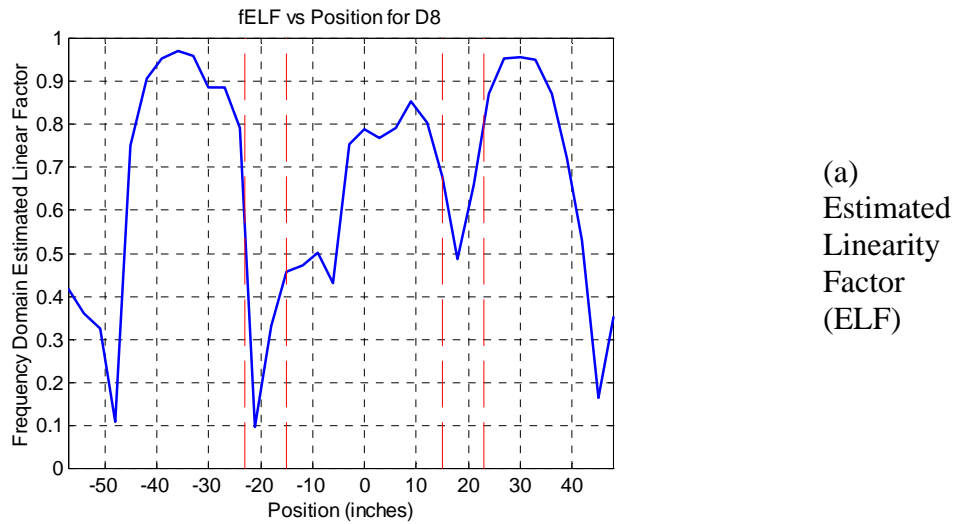
Figure 47   Classification features for Item D8 (M38 box fin)
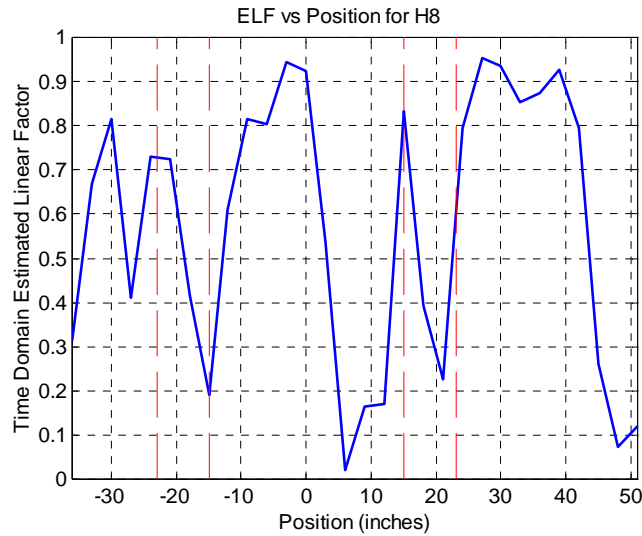
(a) Estimated Linearity Factor (ELF)
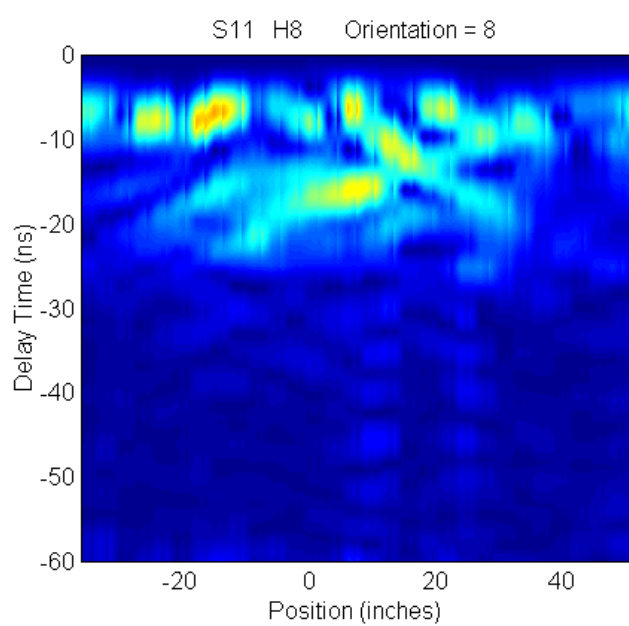
(b) Co-polarized response parallel to pass.
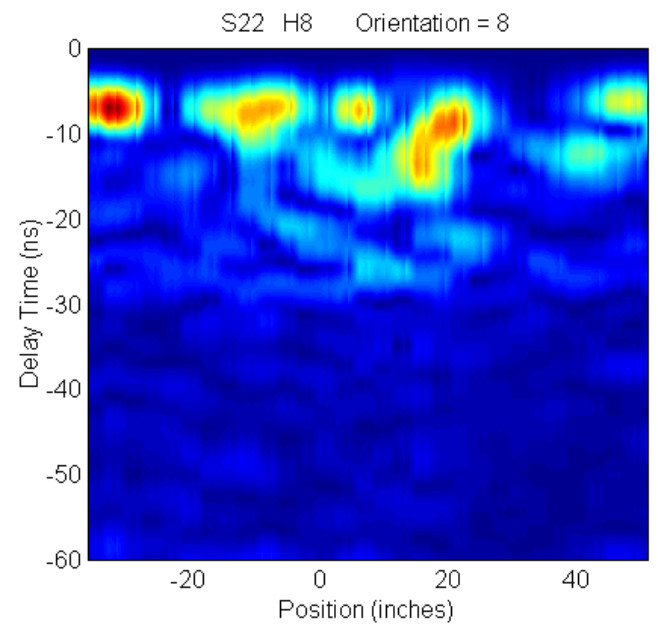
(c) Transverse co-polarized response.

Figure 48   Classification features for Item H8 (horizontal 8" dia. steel disk)
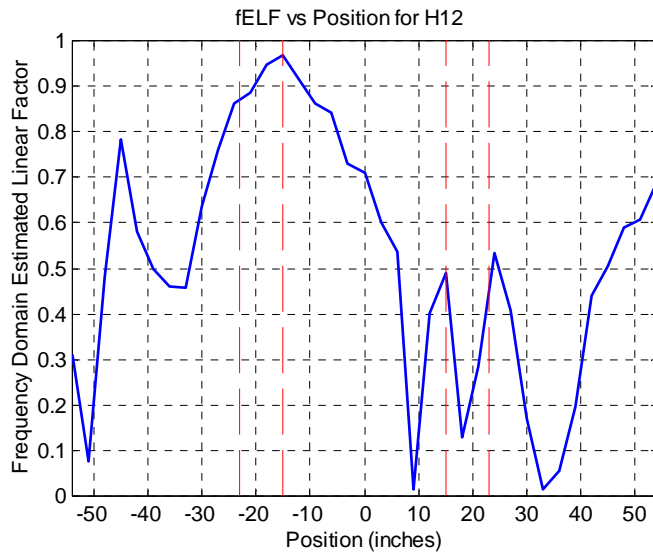
(a) Estimated Linearity Factor (ELF)
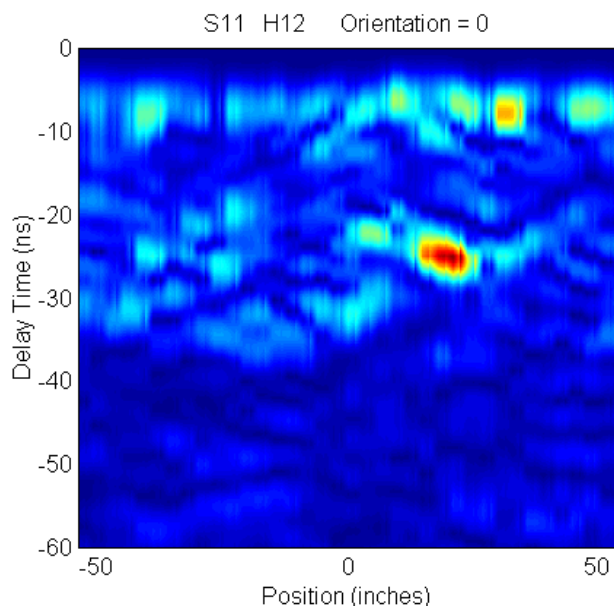
(b) Co-polarized response parallel to pass.
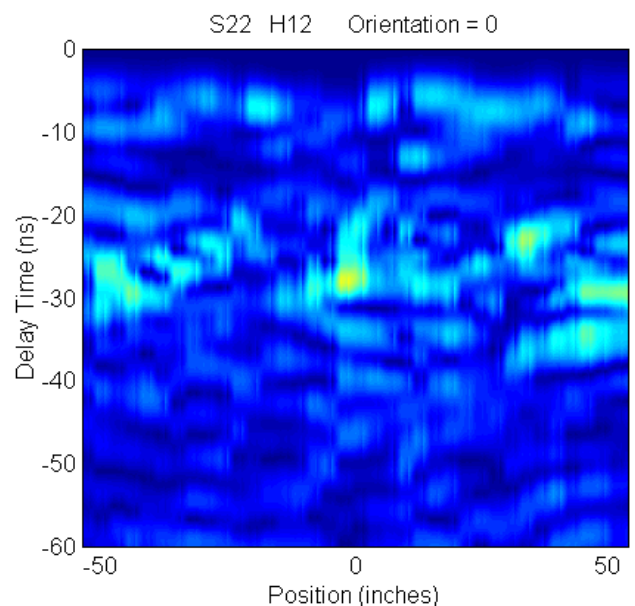
(c) Transverse co-polarized response.

Figure 49.   Classification features for Item H12 (box fin fragment) from pass parallel to target orientation.
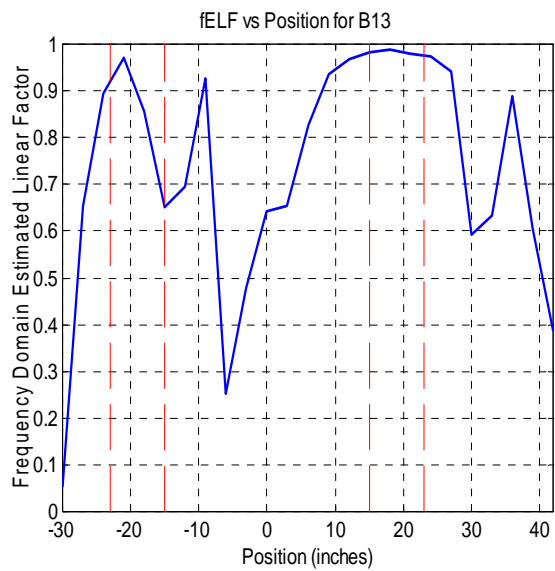
(a) Estimated Linearity Factor (ELF)
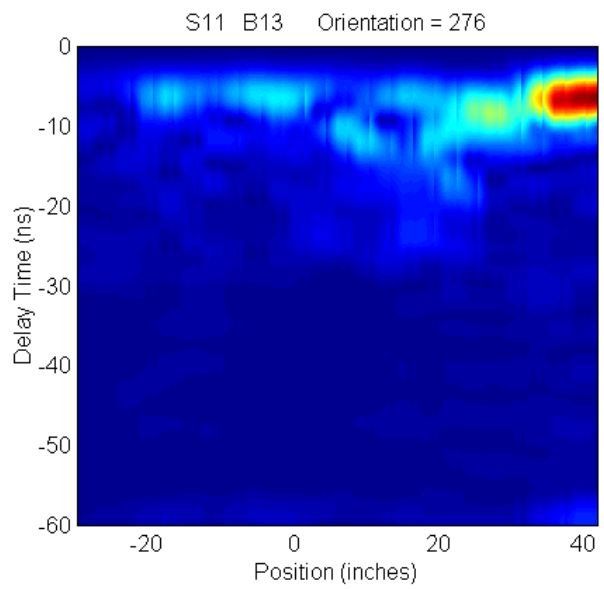
(b) Co-polarized response parallel to pass.

Figure 50   Classification features for Item B13 (vertical 3"x6" cyl.) from survey pass parallel to target orientation
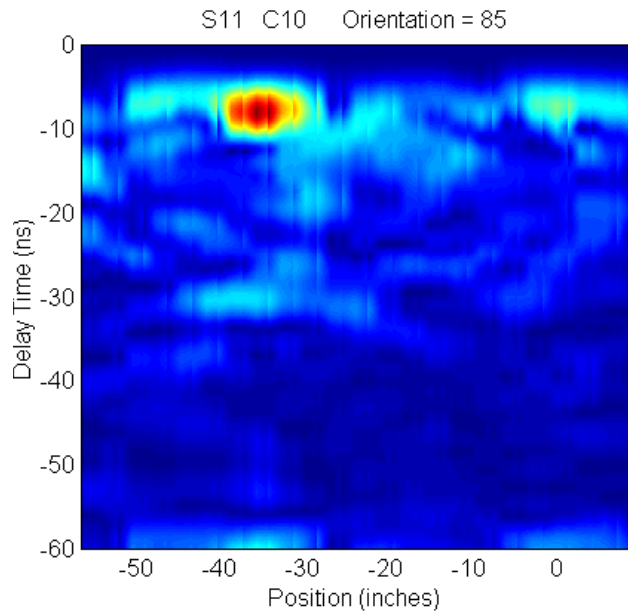
(a) Co-polarized response parallel to pass.
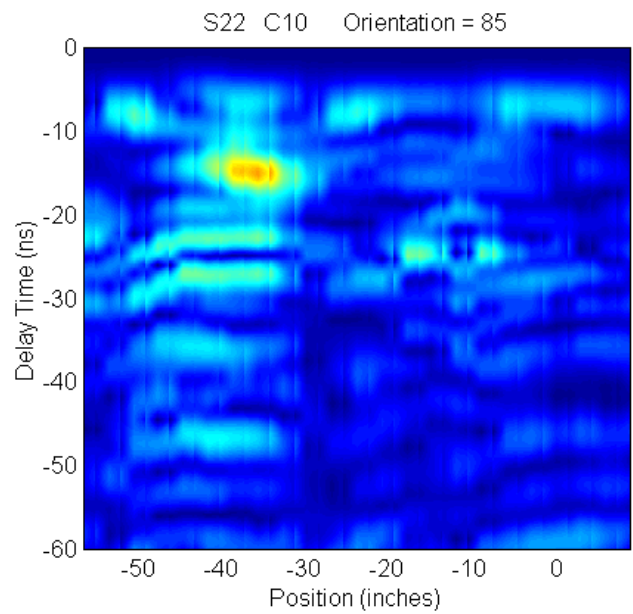
(b) Transverse co-polarized response.

Figure 51   Classification features for Item C10 (vertical 4"x4" plate) from pass perpendicular to target orientation.

5.6 Confidence Level and Signal-to-Clutter Ratio

   The confidence level was implicitly determined by signal intensity, signal-to-clutter ratio and consistency from multiple-pass data. Currently, the confidence levels: HIGH, MODERATE or LOW were entered subjectively by the person performing the classification process. This process started with viewing pictures of features similar to those shown in the previous section. Then the operator went through the classification rules shown in Figure 29 mentally for all passes available for the target. Later, it was found that the SCR and signal intensity have very good correlation with the confidence level set subjectively by operator's impression. This means that the confidence level can be determined more objectively and quantitatively from the signal intensity and SCR in the future. Figure 52 and Figure 53 plot the histograms of SCR's for combined LOW & MODERATE and for HIGH confidence levels, respectively.   These results clearly show the strong correlation between the confidence level and the SCR value. Note that SCR is a function of antenna and time positions. The highest SCR value among all positions for each item was designated as the SCR associated with that particular item. However, it should also be emphasized that the confidence level was not determined by the SCR level alone. Whether features obtained from both parallel and transverse pass showed consistent results (UXO or non-UXO) was also one of the factor in specifying the confidence level.
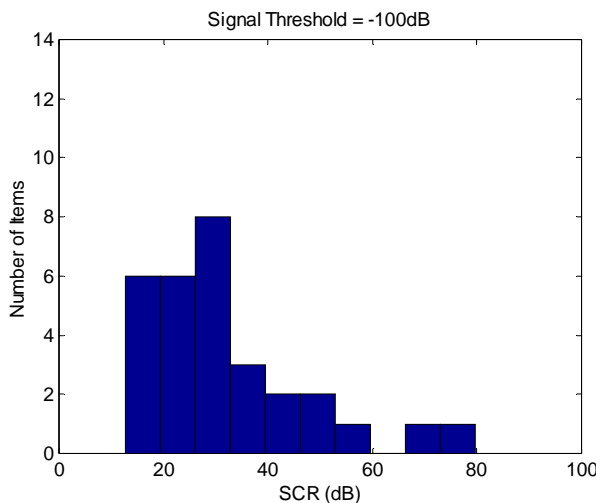

| Figure 52 | Histogram of the SCR associated with the low and moderate confidence level cases (signal level threshold = –100 dB after processing). | Figure 53 | Histogram of the SCR associated with the high confidence level cases (signal level threshold = –100 dB after processing). |
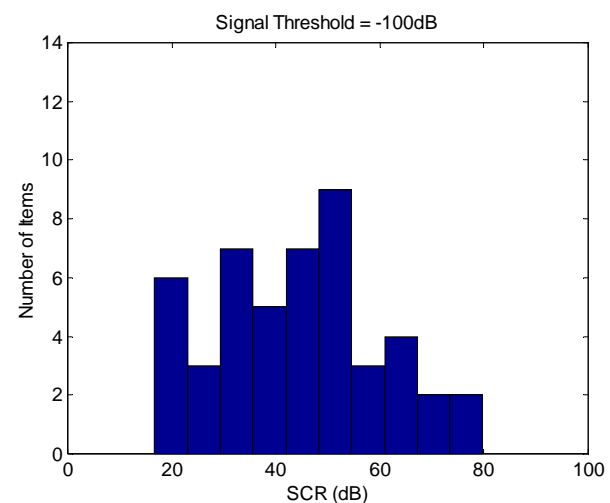
Chapter 6 Analysis of Noise and Clutter Effects on Extracted Parameters

6.1 Simulated Signal to Noise Ratio (SNR) Study

The study of SNR is important for determining the quality of the data collected, the robustness of the feature extraction, and the desirability of prospective system improvements. In this section we explore the effects of noise on the crucial parameters extracted from our GPR data.

There are many sources of noise in a radar system, such as noise from the electronics in the network analyzer, thermal noise in the cable, and ambient noise in the environment. Noise is most commonly observed as white noise, where the amplitude distribution at each frequency has a Gaussian shape. Signal to noise ratio, SNR, is typically measured in decibels (dB), a logarithmic scale value indicating the signal power relative to that of the noise

$$\text{SNR}\,(\text{dB}) \;=\; 10\,log\left(\frac{P_{\text{signal}}}{P_{\text{noise}}}\right) \tag{1}$$

where P_{signal} and P_{noise} are the respective powers of signal and noise. On this scale, a factor of 2 (or of one half) change in the power ratio implies a +(or -)3 dB change. In general, note that positive dB values imply a ratio greater than one, while negative values imply a ratio less than one.   The dB scale is also defined in terms of signal magnitude, instead of signal power.

$$\text{SNR}\,(\text{dB}) \;=\; 20\,log\left(\frac{A_{\text{signal}}}{A_{\text{noise}}}\right) \tag{2}$$

Because, generally speaking, power is proportional to amplitude squared, these alternative definitions provide the same results in terms of dB. Unless noted otherwise, we will use the definition in (2) in what follows. For reference, note that a factor of 10 in amplitude ratio corresponds to a change of $\pm$20 dB.   Measured SNR values

quantified in this manner are compared to desired values for assessing the feasibility of determining signal content.

6.1.1 ELF

In order to understand how ELF and ETO [***defined above,right? are affected by noise, the following idealized simulation based on an ideal linear (very elongated) object and a rotationally symmetric object are investigated. Scattering from these or other objects may be expressed through an eigenvalue matrix, the diagonal of which contains appropriately scaled, intrinsic scattering strengths of the object in its principal orientations, e.g. with polarization parallel to and perpendicular to its major axis. The scattering from an infinitely long thin wire may be represented in eigenvalue matrix, Λ, in which one eigenvalue is very much dominant, reflecting the fact that scattering from a polarization perpendicular to the long axis is negligible. This implies a unitary ELF.

$$\overline{\overline{\Lambda}} = \begin{bmatrix} \lambda_{//} & 0 \\ 0 & \lambda_{\perp} \end{bmatrix} = \begin{bmatrix} 1 & 0 \\ 0 & 0 \end{bmatrix} \Rightarrow ELF = 1 \tag{3}$$

Pre- and post-multiplication of $\overline{\overline{\Lambda}}$ by a rotation matrix $\overline{\overline{M}}$ expresses the results under various target orientations. $\overline{\overline{M}}$ is orthogonal, i.e. $\overline{\overline{M}}^{T} = \overline{\overline{M}}^{-1}$. For our test, Gaussian noise is added to the scattering matrix, $\overline{\overline{S}}$:

$$\overline{\overline{S}}_n = \overline{\overline{S}} + \overline{\overline{N}} = \overline{\overline{M}}^{T} \begin{bmatrix} 1 & 0 \\ 0 & 0 \end{bmatrix} \overline{\overline{M}} + \overline{\overline{N}} \tag{4}$$

$$\text{where } \overline{\overline{N}} = \begin{bmatrix} n_1 & n_3 \\ n_3 & n_2 \end{bmatrix} \text{ and } \overline{\overline{M}} = \begin{bmatrix} \cos(\beta) & \sin(\beta) \\ -\sin(\beta) & \cos(\beta) \end{bmatrix}$$

The matrix $\overline{\overline{S}}$ is the uncorrupted signal. In the matrix $\overline{\overline{N}}$, the components n_1, n_2 and n_3 are random numbers with a Gaussian distribution, scaled by a factor of $10^{(-SNR/20)}$. The components n_1 and n_2 represent both the internal system noise and the external ambient noise. The n_3 component represents mainly the internal system noise and the noise produced from antenna element coupling. Signal quantities are scaled relative to the maximum eigenvalue, i.e. 1. In the matrix $\overline{\overline{M}}$ the variable β is the angle of the target from a position with axis parallel to the signal polarization. Thus, altogether, the new scattering matrix $\overline{\overline{S}}_n$ is the fundamental scattering matrix $\overline{\overline{S}}$ with noise added. In any given test case, it is decomposed into its new eigenvalues, whereupon a noise-biased ELF is calculated from $\overline{\overline{S}}_n$.

Simulations for a thin wire were performed using the procedure described above, with 2000 Monte Carlo realizations. As the SNR is varied from -10 to 60 dB, the added noise causes bias and variation of the estimated features (Figure 54 and Figure 55). The rotation of the target, β, was fixed at 0, 15, and 45 degrees. Figure 54 illustrates SNR versus the biased ELF. As SNR declines to 0 dB (equal signal and noise power and amplitude), the biased ELF approaches 0.45 instead of its true value of 1. The possible percent error in the unbiased ELF can be calculated from this graph. For example, the figure shows that the SNR needs to be greater than approximately 20dB to produce a biased ELF greater than 0.85; that is, to obtain a biased ELF with less than 15% error.

The standard deviation of the biased ELF versus SNR is shown in Figure 55. Note that the target orientation has almost no effect on the biased ELF for all SNR values. Hence accurate biased ELF can be calculated for a target with complete disregard to the orientation of the target. An important revelation of this exercise is that a simulated scattering matrix made up of pure Gaussian noise has an average ELF of approximately 0.45. The value 0.45 shows the natural offset or bias of the ELF equation. This bias is due to the non-linear operations used in calculating the ELF.
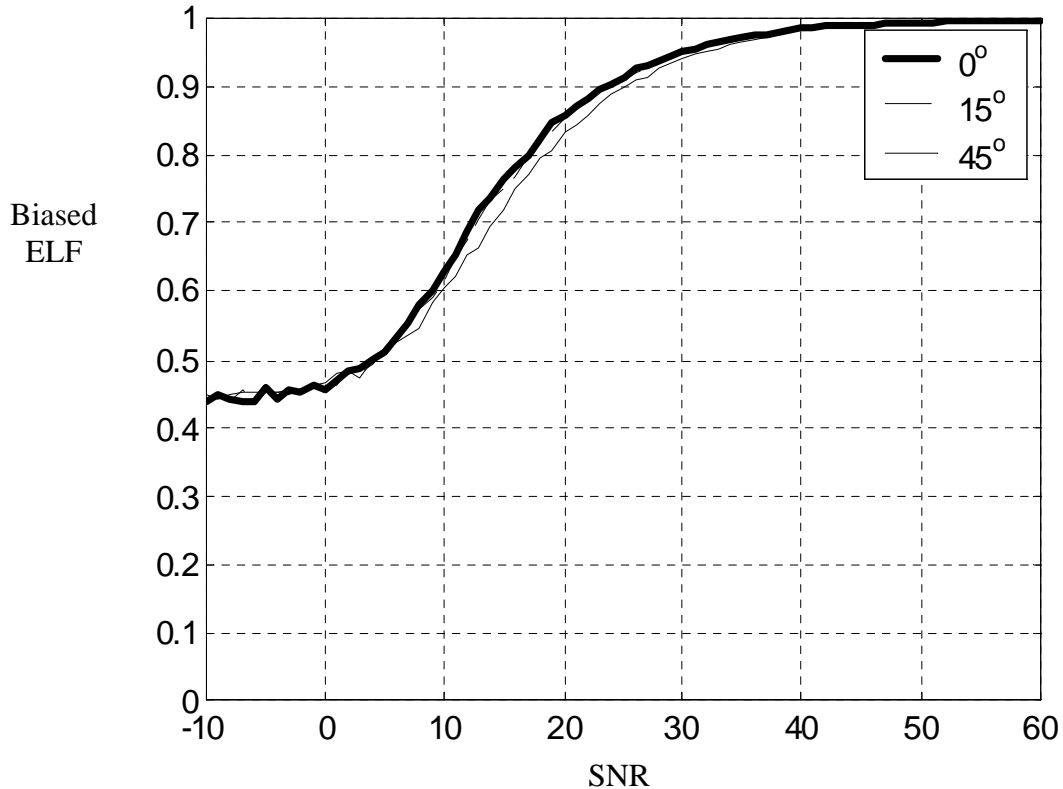
Figure 54 Biased ELF vs. SNR Plot for β = 0, 15, and 45 degrees.

Replacing the zero perpendicular eigenvalue, $\lambda_\perp$, with a one while retaining the unitary parallel eigenvalue (above), simulates the biased ELF for a sphere. The eigenvalue matrix becomes symmetric and the ELF becomes zero, as it should for a completely symmetric object:

$$\overline{\overline{\Lambda}} = \begin{bmatrix} \lambda_{//} & 0 \\ 0 & \lambda_\perp \end{bmatrix} = \begin{bmatrix} 1 & 0 \\ 0 & 1 \end{bmatrix} \Rightarrow ELF = 0 \tag{5}$$
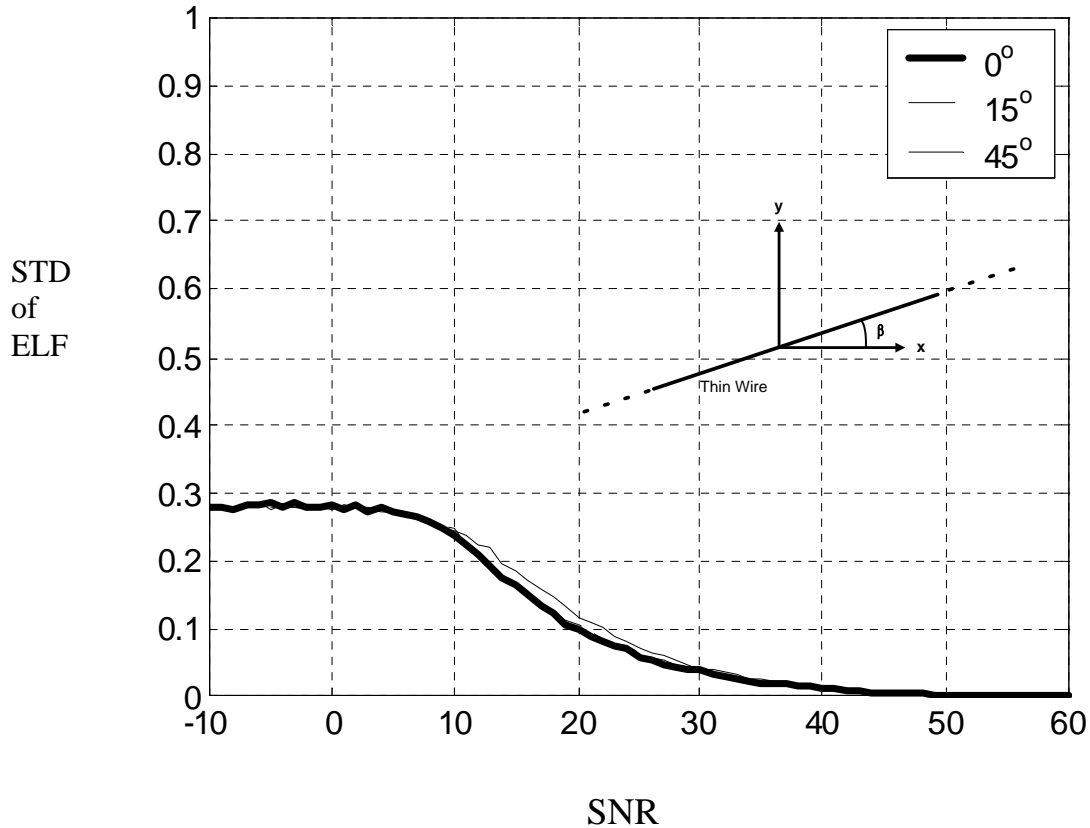
Figure 55 Standard Deviation (STD) of ELF vs. SNR for $\beta = 0$, 15, and 45 degrees.

The eigenvalue matrix, Λ, is not rotated in this test because there is no difference in the response from different target angles for a completely symmetric object. Gaussian noise is added to the scattering matrix in the same manner as for the wire case, with the biased ELF subsequently calculated from $\overline{\overline{S}}_n$.

The results of the symmetric object simulation are shown in Figure 56 and Figure 57. The former shows that the presence of noise causes the ELF to rise to a value of 0.53 when the SNR is around 0 dB. The standard deviation of ELF is plotted versus the SNR in Figure 57.
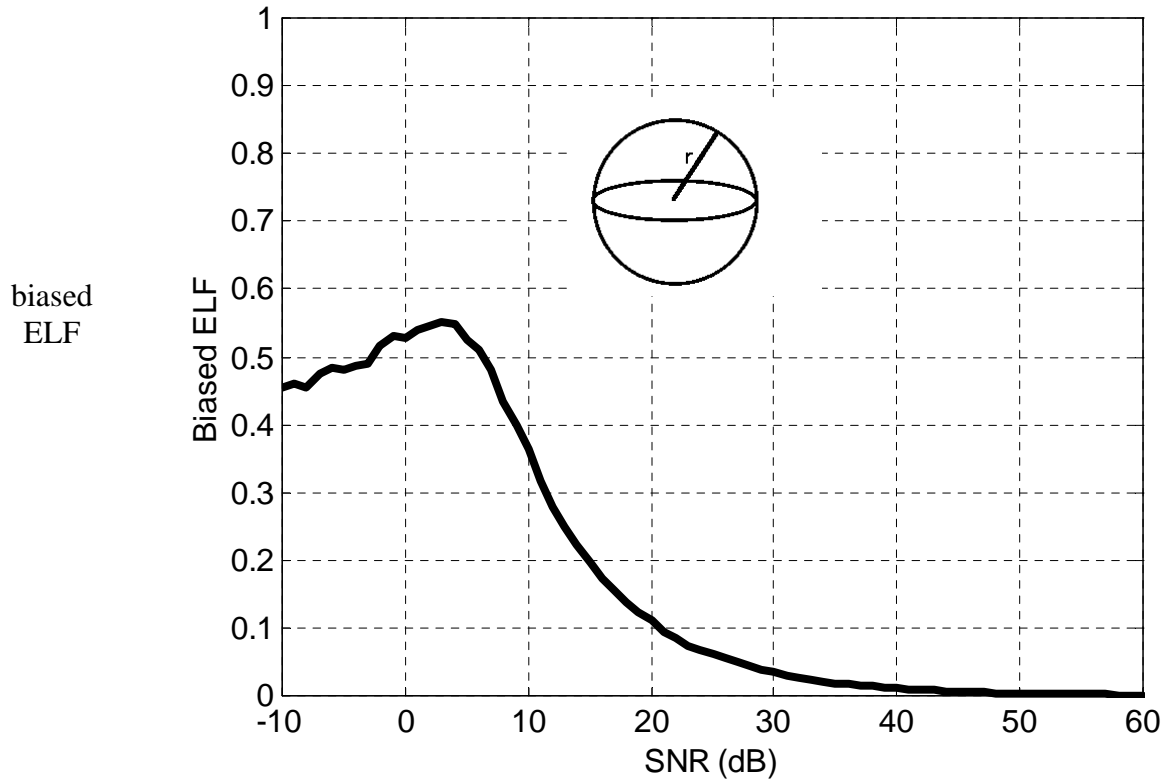
biased
ELF

Figure 56 Biased ELF vs. SNR for a simulated sphere

Figure 58 shows a comparison of the biased ELF for a simulated long wire and a simulated sphere. This graph shows that a target response with SNR below approximately 10 dB (the dark shaded region) would have an ambiguous ELF. This means that the biasing of the ELF has become so large that it would be very difficult to determine a linear target from a symmetric target. It appears that with a SNR above approximately 20 dB, there would be sufficient dynamic range in the ELF to determine the linearity of an object reliably. In the "twilight

zone" between 10 dB and 20 dB SNR, it should often be possible to determine the ELF, but possibly with some ambiguity or difficulty.
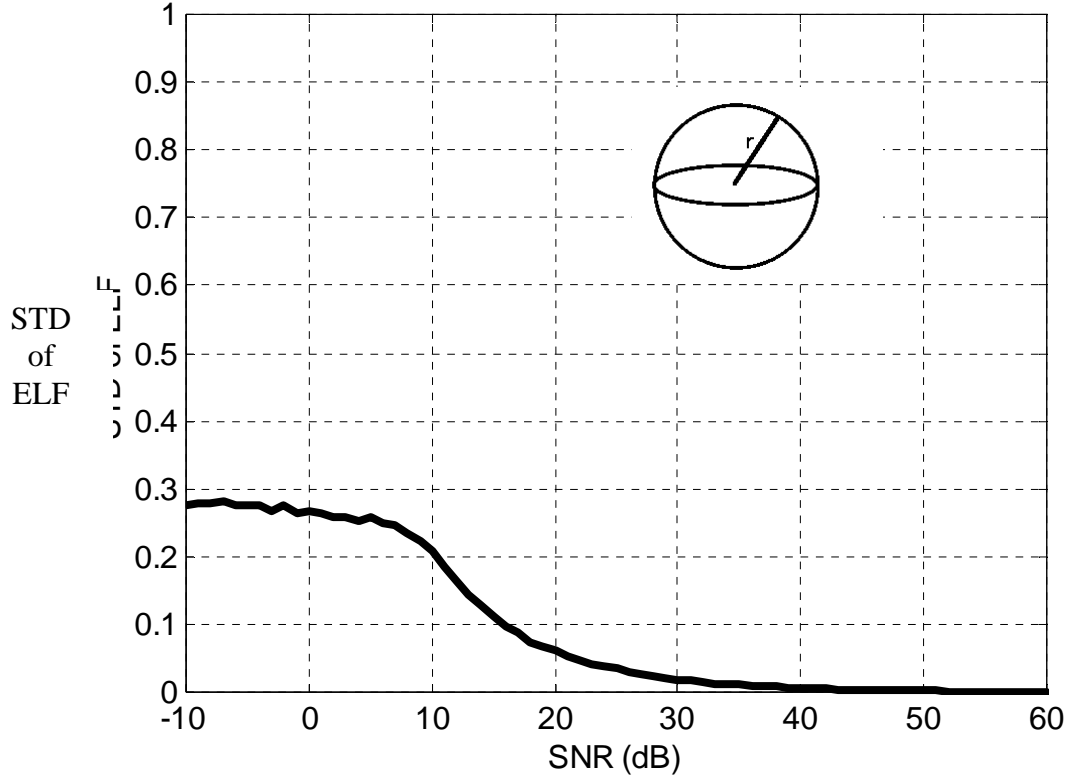
Figure 57 Standard Deviation (ELF) vs. SNR for a Simulated Sphere

The error in the biased ELF for the long wire and the sphere is shown in Figure 59. The error is calculated by subtracting the theoretical ELF value from the simulated biased ELF value. The graph shows that the error in ELF due to noise is very similar for both the wire and the sphere, despite their gross differences in geometry. This is quite useful for estimating the possible error in ELF for all measured targets based on their measured SNR. Next, we pursue a study of the effects of SNR on the ETO.
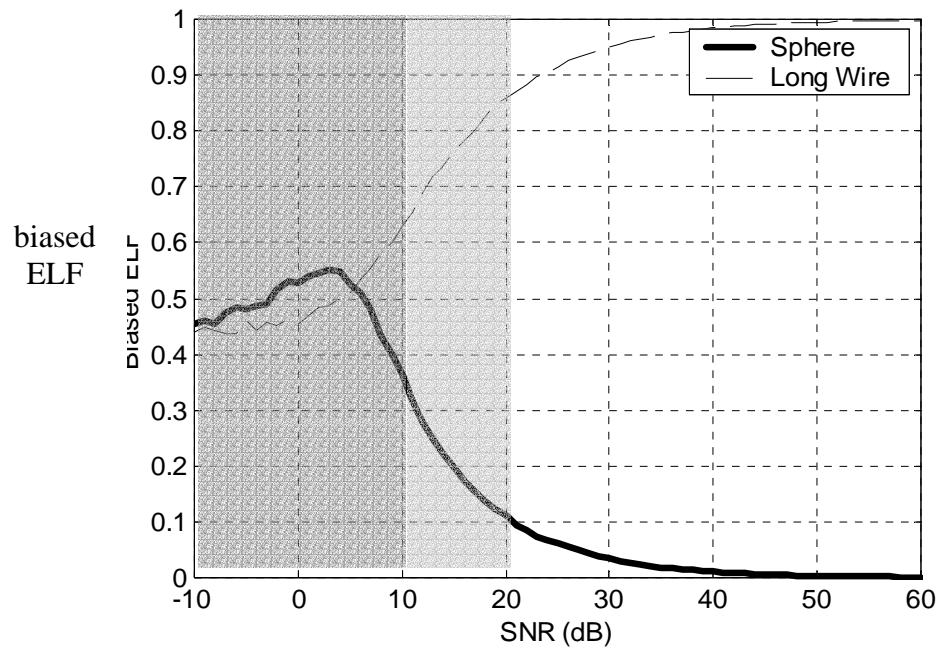
Figure 58 Comparison of biased ELF vs SNR for a simulated long wire and sphere
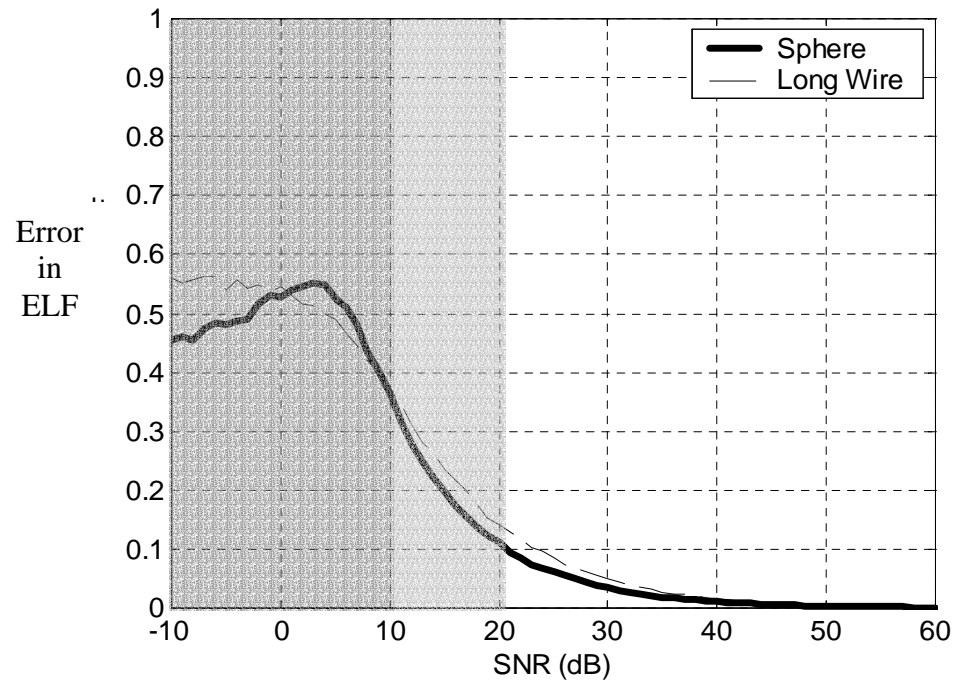
Figure 59 Comparison of error in ELF vs SNR for a simulated long wire and sphere

6.1.2 ETO

The effect of noise on the unbiased ETO is discussed in this section. The biased, i.e. noise affected, ETO for a wire is calculated from the $\overline{\overline{S}}_n$ of equation (4) as follows. The scattering matrix $\overline{\overline{S}}_n$ is decomposed into its eigenvalues and the associated eigenvectors are determined. The direction in which each eigenvector points is that associated with its corresponding eigenvalue. Thus, as for the actual field data, the ETO is calculated from the arctangent of the dominant eigenvector orientation angles. Comparison of the biased ETO to the actual target angle, β, reveals the biasing due to noise.

The biased ETO was calculated for various wire orientation angles and for SNR levels ranging from -10 to 60 dB. Figure 60 shows how the unbiased ETO feature is affected by the presence of noise for four target angles. At a target angle of zero degrees (i.e. perfect alignment with the radar polarization) the biased ETO shows almost no dependence on SNR, varying closely around the correct value of zero. At target angles of 45, 60, and 75 degrees relative to radar polarization the processing performance becomes worse, the greater the rotation. In reality, given the survey system using at a minimum two perpendicular passes above a target location, 45 degrees probably represents the worst case. Noting that for $\beta = 45^{o}$ reasonable ETO estimates appear for SNR less than 10 dB, we wee that this parameter is less sensitive to noise than the ELF. The plot of the standard deviation of ETO versus SNR is shown in Figure 61 for the four target angles. It illustrates that the "correct" values of ETO obtained at low SNR values under zero rotation do not really indicate that the system is performing well at that noise level. Rather, the system is relatively indiscriminate there and orientations simply tend to average out to a zero value, which happens to be correct.
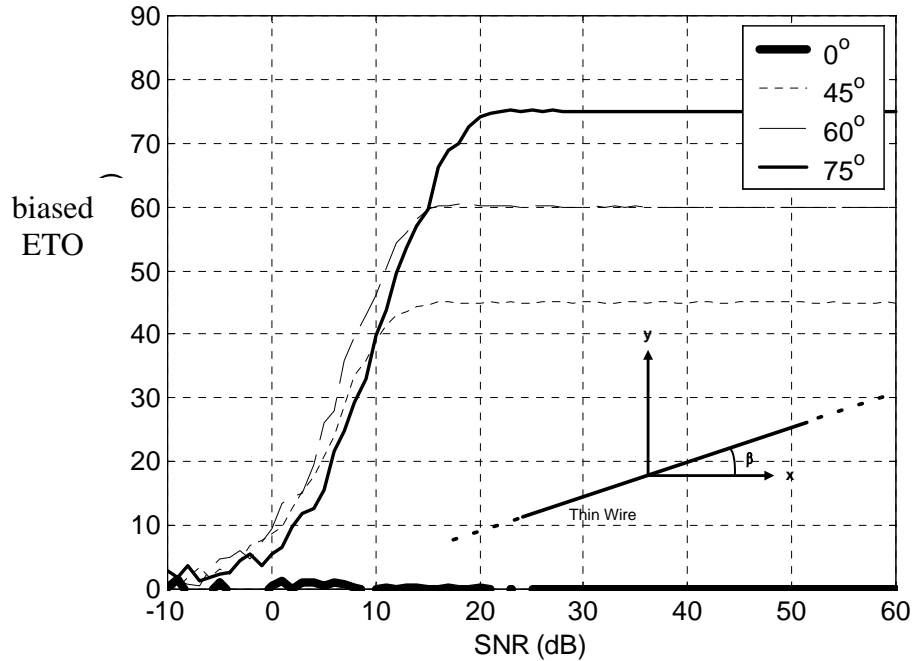
Figure 60 Biased ETO vs. SNR for β = 0, 45, 60, and 75°.
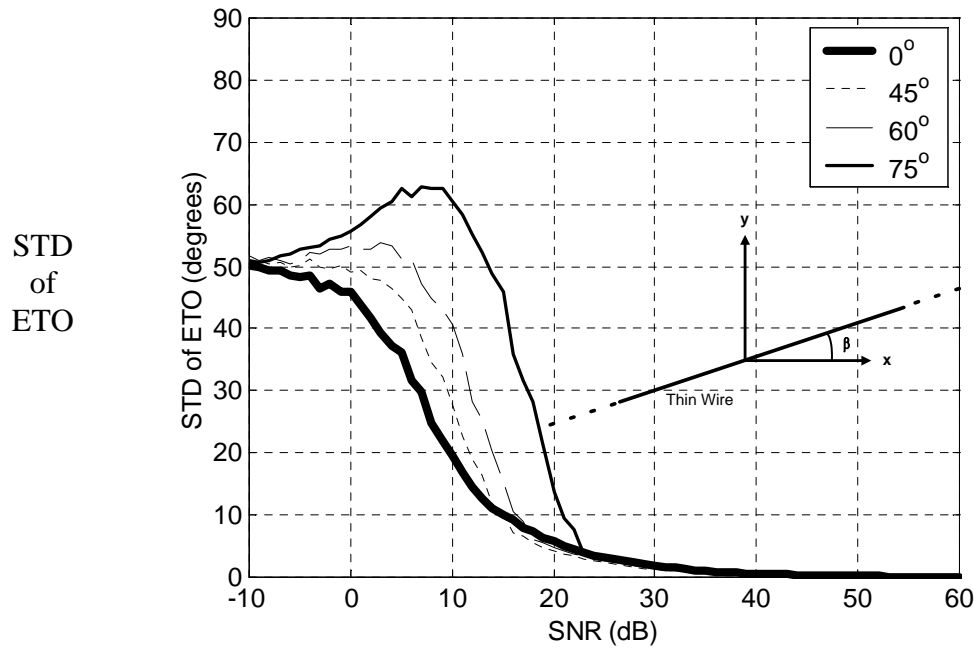
Figure 61 Standard deviation STD (deg) of ETO vs. SNR for β = 0, 45, 60, and 75°

These studies show how SNR can affect the ELF and ETO features. The processing depends
fundamentally on these features to estimate target linearity and existence of a dominant orientation, which are

clues to UXO-like geometry. The analysis provides the guidance that the measured data needs to have an SNR of at least 10 to 20 dB to produce tolerably accurate biased ELF and ETO values, with the latter being less sensitive.

6.2 Measured Signal to Noise Ratio (SNR)

The analysis above has suggested that a minimum SNR level of 10 to 20 dB is required if we are to determine fundamentally necessary signal and target features. The question becomes, how realistic is this SNR threshold? To answer this question two sets of data will be examined. First, the method of calculating the SNR from the measured data will be discussed. Then, the distributions of SNR for the measured data will be presented.

The SNR of measured data is estimated in the course of feature extraction. The magnitude of the maximum eigenvalue in the time-domain is determined and is then used as a representative true signal level, e.g. as $\lambda_{//}$ above. The noise level was found by averaging a segment of the negative-time region with the same duration as the signal's late-time region. The negative-time region was used because it *only* contains noise. The SNR was then calculated from this representative signal level and the noise level. For multi-point measurements the signal becomes a function of position, with the SNR calculated at each point in the same way as for the single-point measurements. The overall SNR value for a site was found by finding the maximum SNR for the multi-position scan.

Figure 62 shows the SNR values of every target measured in the previous Tyndall AFB demo, superimposed on the average error curve for the theoretical biased ELF vs SNR (Figure 59). Note that in this case each target's features were obtained using a single spatial point, because at the time of the Tyndall demo multi-position processing had not yet been implemented. For each target the SNR from the measured data was used to indicate the likely position on the theoretical error curve for that target. Each error vs SNR value is plotted on the curve by a black diamond marker for all 153 separate targets. Note that the SNR values were rounded to whole numbers for ease of plotting; therefore there are many overlapping black diamond markers. In any case, *all* of the target markers lie above the 20 dB threshold. In fact, all but two targets have SNR values greater than 30 dB, with correspondingly small associated error. This analysis strongly supports the inference that noise is not a limiting factor for this measurement set.
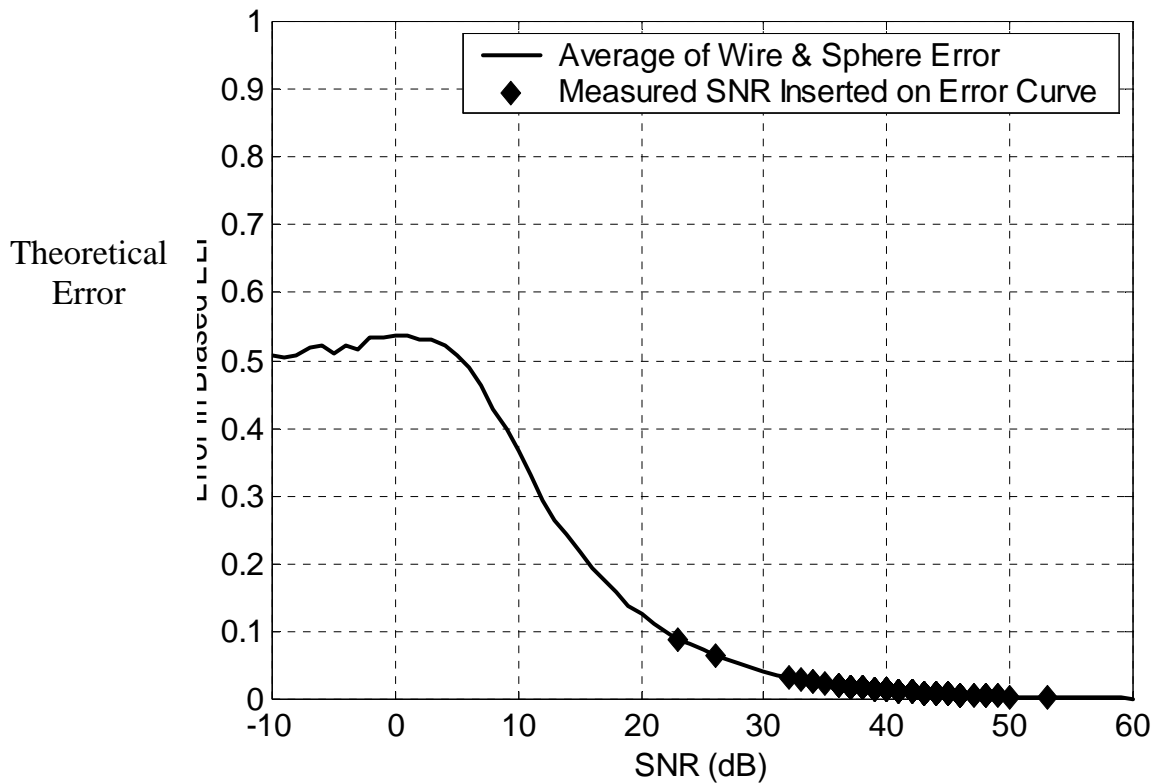
Figure 62 Tyndall AFB Demo estimated error vs measured SNR values for each target

In Figure 63 the SNR values for the multi-position measurements taken at Blossom Point are used to locate the targets on the same theoretical ELF error curve applied above. There were 91 separate targets. Again, most of the targets lie above the 20 dB threshold. Although at least four targets show a likely SNR value less than 20 dB, once again noise does not appear to be a limiting factor for this measurement set. The analysis allows us to identify those targets with a SNR less than 20 dB, which required more careful examination and are noted to produce less confident classification.
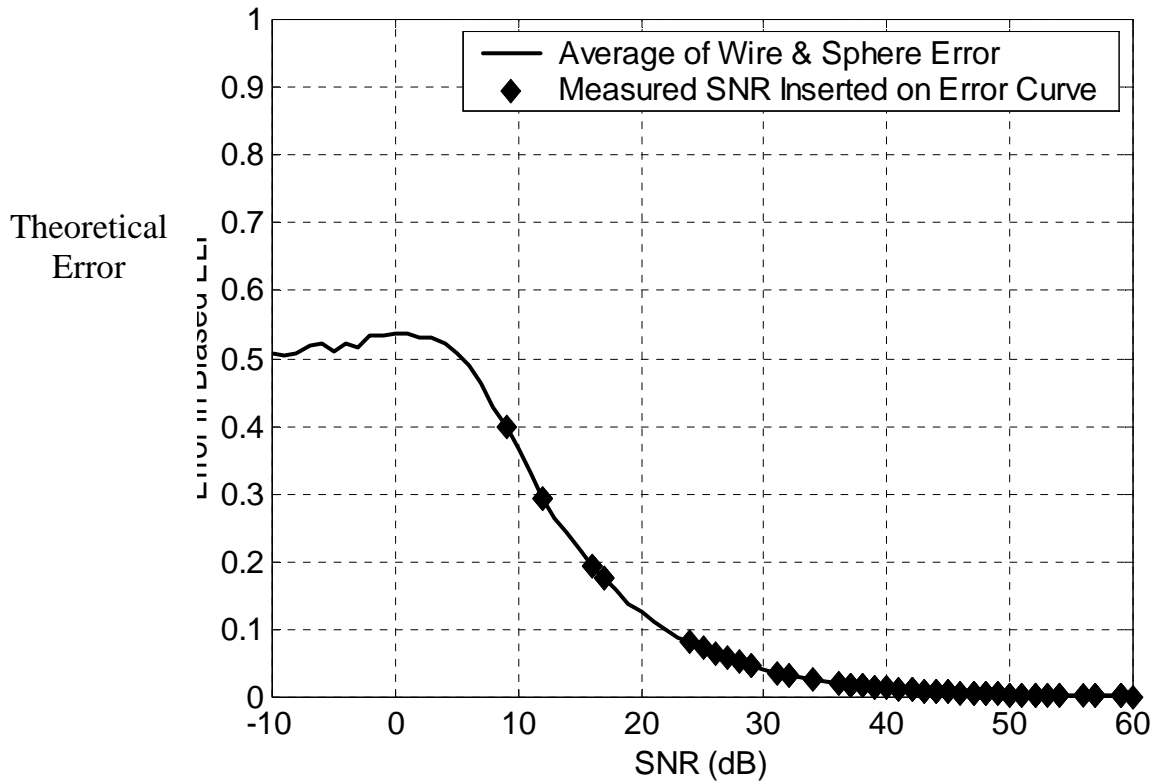
Figure 63. Blossom Point estimated error vs measured SNR values for each target.

Figure 64 shows a histogram of the SNR occurrences for the single point measurements at the Tyndall site. A majority of the SNR values are grouped around 40 dB, showing a very good SNR level for the entire site. Figure 65 shows a histogram of SNR occurrences for the multi-position measurements of the Blossom Point site. Here the SNR values are more evenly distributed between about 35 to 60 dB. However, there are 8 targets with SNR levels less than 20 dB. These 8 targets account for less than ten percent of the total targets. Again, it appears that noise is not a limiting factor for the entire site, but could be for a few individual targets, which the analysis duly identifies. The other source of interference is clutter, which will be discussed in the next section.
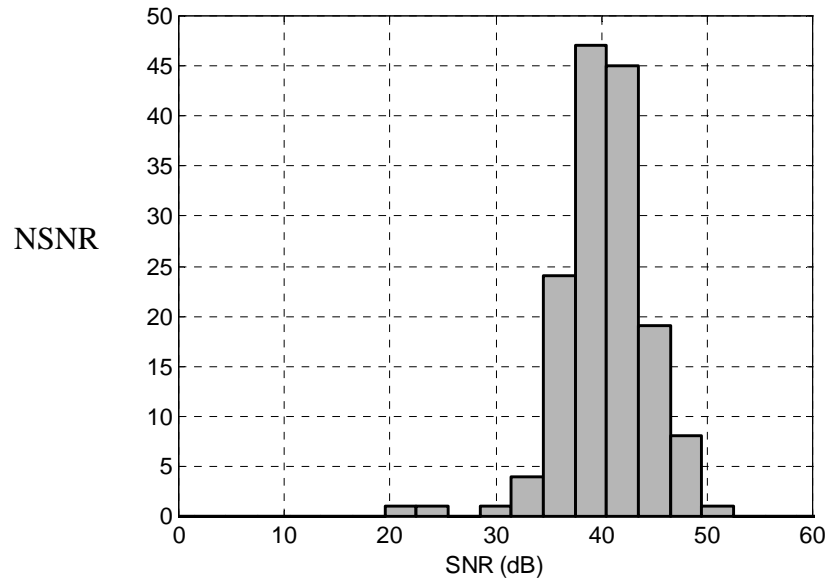
Figure 64. Distribution of occurrences of SNR values (NSNR) for the Tyndall Data
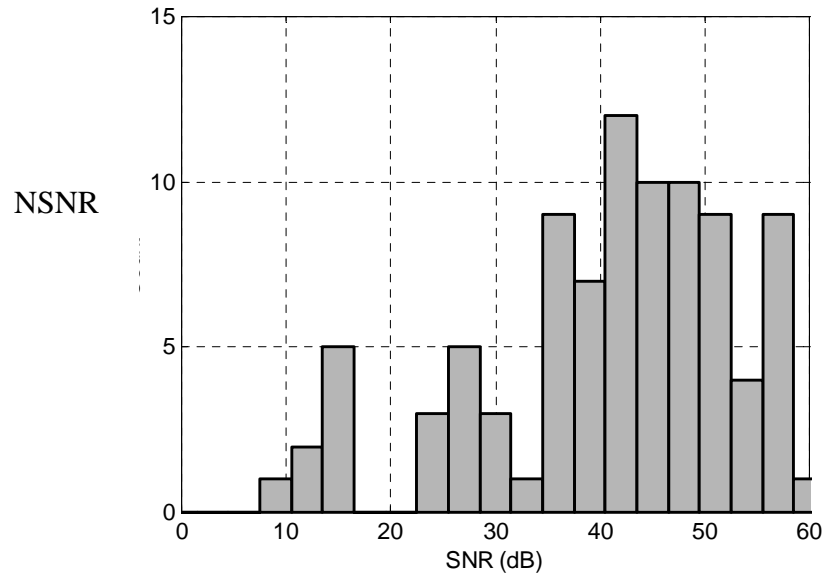
Figure 65. Distribution of occurrences of SNR values (NSNR) for the Blossom Point Data

6.3 Simulated Signal to Clutter (SCR) Study

The study of SCR (dB) is also important for determining the quality of the data collected, the robustness of the feature extraction, and the desirability of various system improvements. In this section we explore the

effects of signal clutter on the crucial parameters extracted from our GPR data. Clutter will be defined as any undesired signal that affects the signal produced by the target of interest. Note that we use the term "signal" as opposed to noise. While clutter responses may be complex and varied, they are not random in the sense that system noise is, as pursued in the previous section. Clutter responses are simply those reflections produced by objects of no interest for UXO discrimination, such as rocks, roots, cavities, soil inhomogeneities, and widespread small metallic scrap. Individually, these signals are coherent in the same way that the desired signals are. In most ground conditions, the average clutter levels in co-polarization channels, S_{11} and S_{22}, are approximately the same and much higher than that in the cross-polarization channel, S_{21} (by the principal of reciprocity, S_{21} equals S_{12}, so we only define values for one of the cross polar channels).

In order to study clutter effects on the extracted feature parameters, simple simulations are performed in which clutter responses are added to the underlying target signal. Then the ELF and ETO for an ideal linear object and an ideal rotationally symmetric object are obtained and evaluated.

6.3.1 ELF

In the previous section, biased ELF, ETO, and the scattering matrix were defined. In order to understand how ELF is affected by clutter, one may begin with a perfect linear scattering object, i.e. an infinitely long thin wire. Then, as above, the target's eigenvalue matrix, $\overline{\overline{\Lambda}}$, is rotated by matrix $\overline{\overline{M}}$ to simulate various target orientations. Clutter is added into the scattering matrix:

$$\overline{\overline{S}}_c \;=\; \overline{\overline{M}}^{\,T}\,\overline{\overline{\Lambda}}\,\overline{\overline{M}} \;+\; \overline{\overline{C}}$$

(6)

$$\text{where } \overline{\overline{C}} = \begin{bmatrix} c & c/10 \\ c/10 & c \end{bmatrix} \text{ and } \overline{\overline{M}} = \begin{bmatrix} \cos(\beta) & \sin(\beta) \\ -\sin(\beta) & \cos(\beta) \end{bmatrix}$$

In the matrix $\overline{\overline{M}}$ the variable β is the angle of the target from an alignment parallel to the incident polarization. In the matrix $\overline{\overline{C}}$, c is a positive real number scaled by a factor of $10^{(-SCR/20)}$. Note that c is simply a magnitude, not a random variable. We do not apply assumed distribution to c, nor require many Monte Carlo realizations for the analysis. The off-diagonal terms of matrix $\overline{\overline{C}}$ were also scaled by 1/10 to simulate a typical ratio between the co-pol and cross-pol channels. Varying the SCR from -10 to 60 dB produced different values of c. The signal eigenvalue matrix was either that for the long wire or sphere:

$$\overline{\overline{\Lambda}} = \underbrace{\begin{bmatrix} 1 & 0 \\ 0 & 0 \end{bmatrix}}_{wire} \quad or \quad \underbrace{\begin{bmatrix} 1 & 0 \\ 0 & 1 \end{bmatrix}}_{sphere} \tag{7}$$

After the clutter signal was added to the system, the new scattering matrix, $\overline{\overline{S}}_c$, was decomposed into it's eigenvalues and the ELF determined.

Figure 66 and Figure 67 show that the added clutter causes a bias in the estimated features. For the wire (Figure 66), equal signal and clutter magnitudes (0 dB SCR) produce a biased ELF of only 0.33, relative to the "true" value of one. Overall, the SCR must reach about 20 dB before the biased ELF error is only 20% or less. Interestingly, there was almost no discernable difference in the biased ELF curves for various target angles, β, therefore only the zero degree case is shown. This supports the position that accurate ELF can be calculated for a target with complete disregard to the orientation of the target, as observed above in the SNR analysis.

For the sphere, the ideal, noise and clutter-free ELF is zero. Figure 67 shows that the biased ELF rises to a value of 0.05 when the SCR declines to 0 dB. This shows that the ELF estimation for a symmetric object is not effected by the presence of symmetric clutter. Figure 68 shows the error in biased ELF for both the sphere and the long wire. The two error curves will be used below in discussion of measured targets.
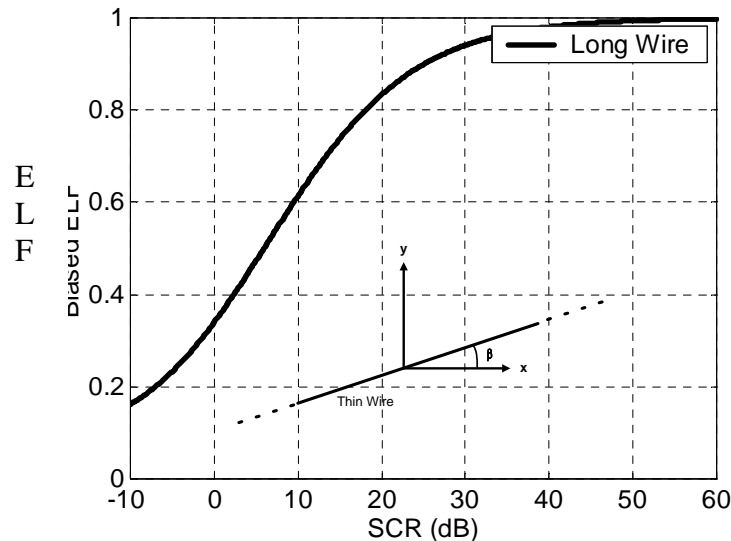
Figure 66. Biased ELF versus SCR for a simulated long wire
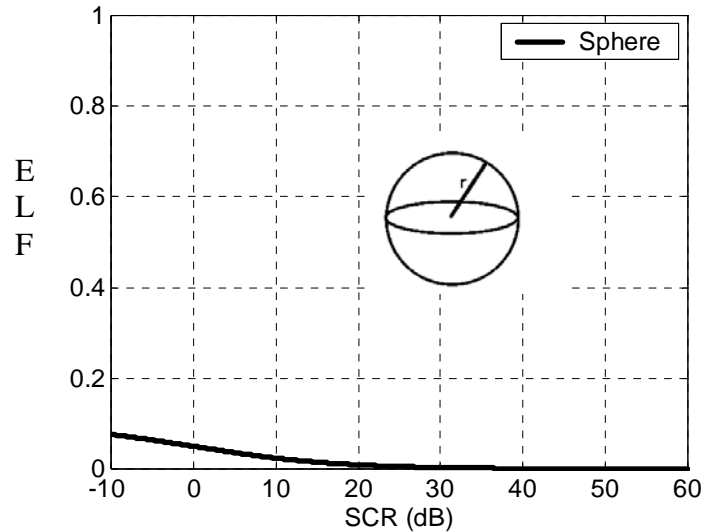
Figure 67. Biased ELF versus SCR for simulated sphere
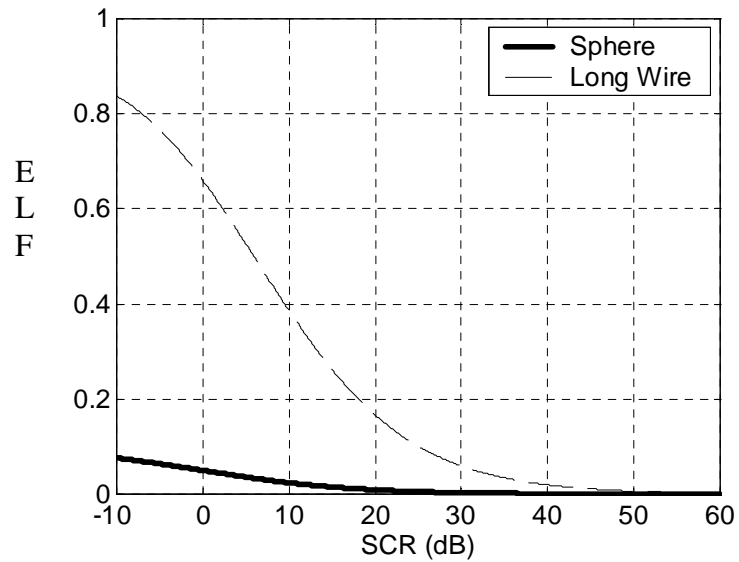
Figure 68. Comparison of error in ELF for simulated long wire and sphere.

6.3.2 ETO

The effect of simulated clutter on the unbiased ETO is discussed in this section. As before, the biased ETO is calculated from $\bar{\bar{S}}_c$ in equation (6). The scattering matrix $\bar{\bar{S}}_c$ is decomposed into its eigenvalues and eigenvectors; then the ETO is calculated as the arctangent of the eigenvector angles. The difference between the biased ETO and the target angle, β, is the biasing due to clutter.

The biased ETO was calculated for a long wire with various rotation angles relative to alignment with the transmitted polarization. The SCR level ranged between -10 to 60 dB. Figure 69 shows how the unbiased ETO feature is affected by the presence of clutter for four target angles, by plotting the error in biased ETO versus SCR. At a target angle of 45 degrees the ETO shows no dependence on SCR. At target angles of 0 (upper curve), 75, and 90 degrees the ETO error does not become entirely negligible until the SCR is approximately 10 dB. However, the ETO error is tolerable at an SCR level of about 0, and is only 15% for an SCR at the worst value of –10 dB. That is, the ETO error is in general not significant.
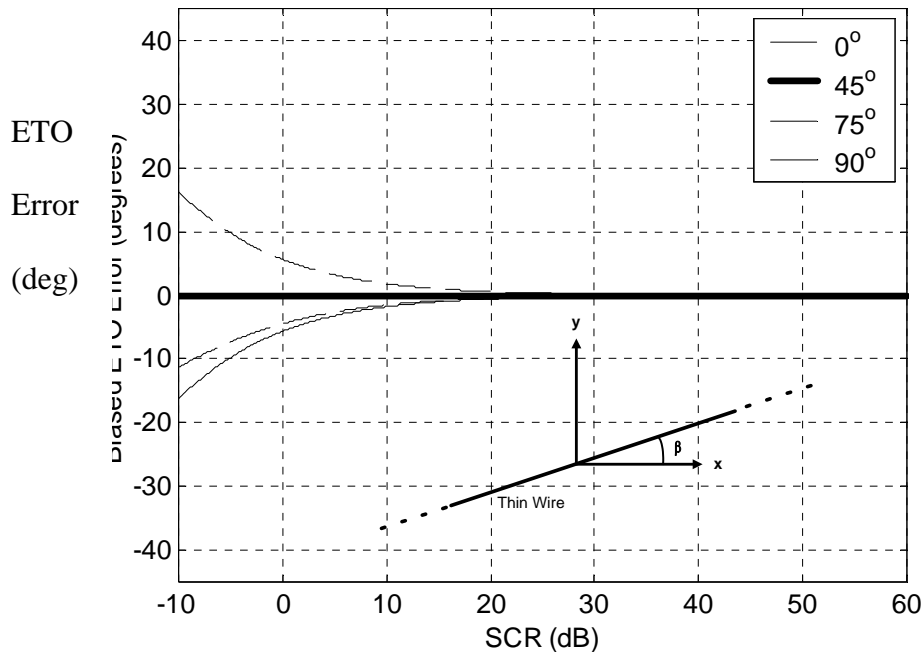
Figure 69 ETO error in degrees vs SCR.

These calculations support the view that the measured data needs to have an SCR greater than about 20 dB in order to produce a valid estimate of the ELF. The ETO is much less sensitive, with very small clutter-generated error overall. Thus, as above in the examination of SNR effects, the signal contamination is most likely to limit determination of ELF but not ETO.

6.4 Measured Signal to Clutter Ratio (SCR)

The signal to clutter ratio (SCR) for the measured data from the Tyndall and Blossom Point sites will be presented in this section. First, the method of calculating the SCR from the measured data will be discussed. Then, the distributions of SCR for the measured data will be presented.

The SCR of the measured data was calculated after the feature extraction. The magnitude of maximum eigenvalue in the time-domain was found from the measured data. The eigenvalue was used for the signal level. The clutter level was found by using the response of an empty site and extracting the eigenvalues from its late-time region. The empty site late-time region was set equal to the late-time region of each target. This ensured corresponding late-time regions, with similar depths. The maximum empty site eigenvalue was set as the clutter level. The SCR was then calculated from the signal level and the clutter level of each site.

Figure 70 shows a single position time-domain response for a measured target. The highlighted region is the selected late-time region (12 – 26 ns) used for feature extraction and the calculation of the signal level. Figure 71 shows a single position time-domain response for a measured empty site. The highlighted region corresponds to the late-time region (12 – 26 ns) selected for the target in Figure 70 and is used to calculate the clutter level.
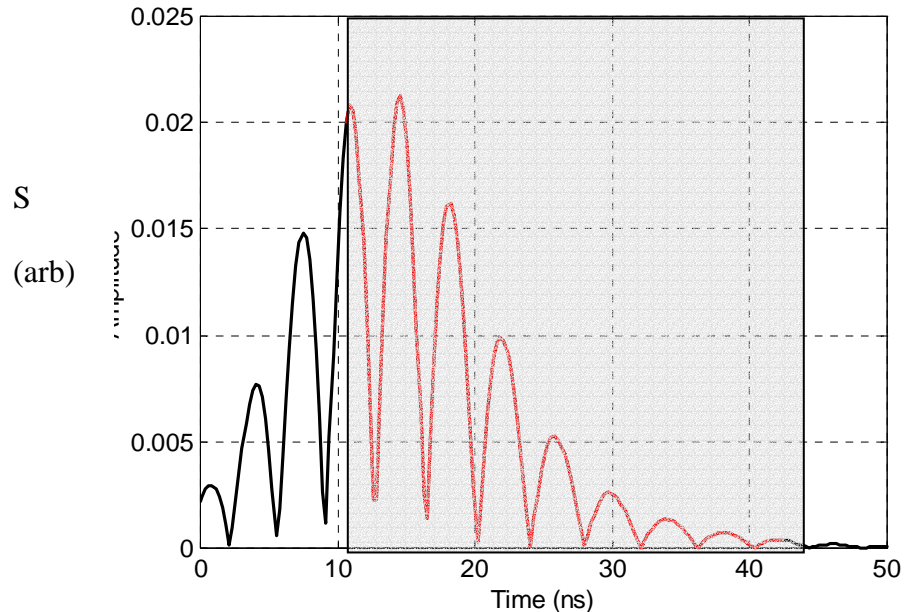
Figure 70 Target response S and selected late time region (signal)
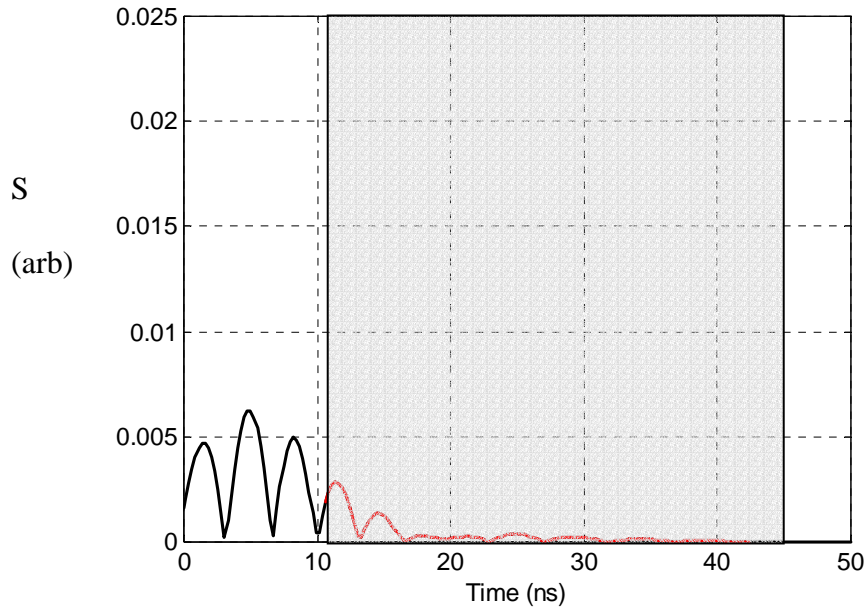
Figure 71 Empty site response and corresponding selected time region (clutter)

For multi-point measurements the SCR became a function of position. The SCR is calculated the same as in the single-point measurements for each antenna position. The overall SCR value for a site was found by finding the position with the maximum clutter signal level.

Figure 72 shows the "waterfall" plot of a target measured using the multi-position survey method at Blossom Point. The two white lines superimposed on the plot represent the selected late-time region for the given target. This region was used to calculate the signal level for this target. The same late-time region lines are superimposed on Figure 73, the waterfall plot of an empty BP site. This region was used to calculate the clutter level. The empty site has the same frequency filtering and smoothing windows applied to it as the target response had. This is done to try to calculate a fair representation of the clutter level.
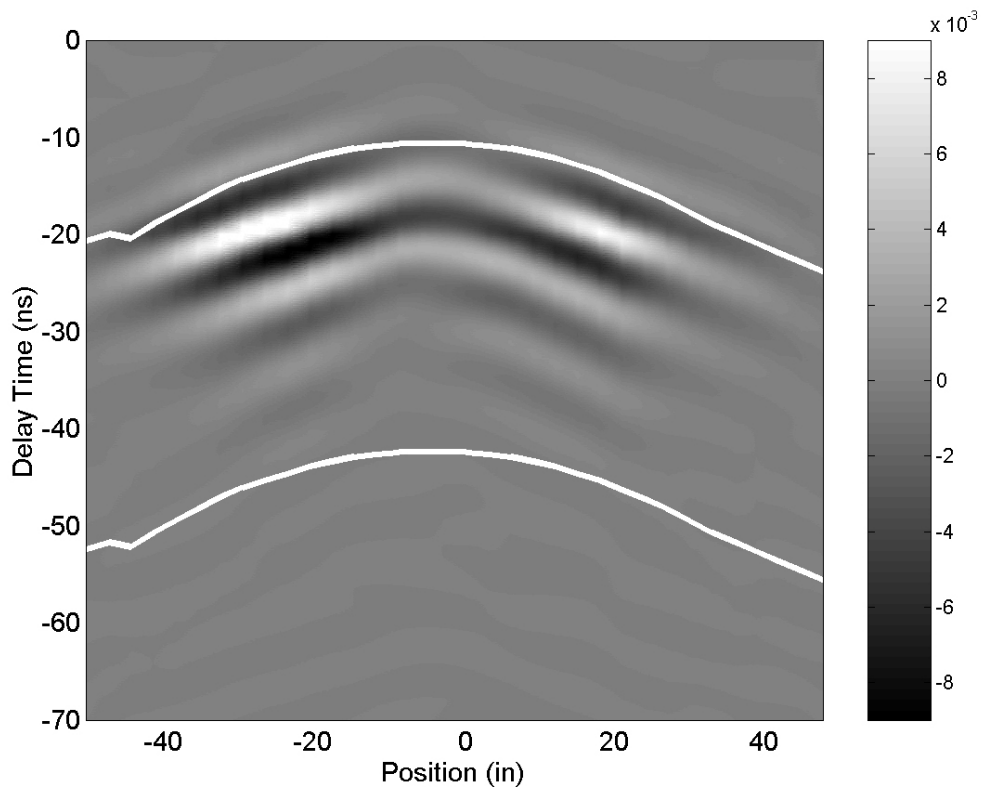
Figure 72 Target (MK-23) site (B2) waterfall plot (signal)
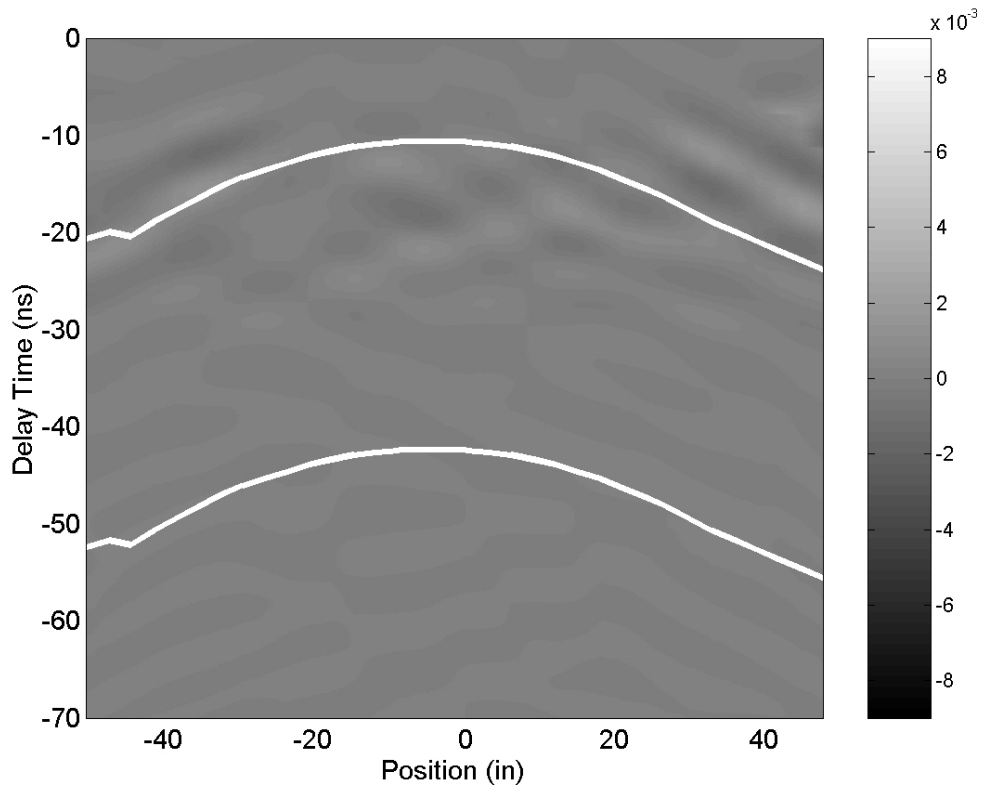
Figure 73 Empty site waterfall plot (clutter)

In Figure 74 the SCR values of every Tyndall demo target, measured using the single point method, are superimposed on the two theoretical biased ELF error discussed above. That is, each SCR value is plotted on the ELF curve with a black diamond marker on the long wire error and a black filled circle for the sphere error. There were 153 separate targets measured at Tyndall AFB (Appendix A). It should be noted that the SCR values were rounded to the nearest one tenth for ease of plotting; therefore there are many overlapping black diamond and circle markers. One can see that all of the targets lie between 5 and 25 dB. A majority of the targets lie below the 20 dB threshold discussed earlier. This shows that there will possibly be errors in the ELF and ETO parameters due to clutter.
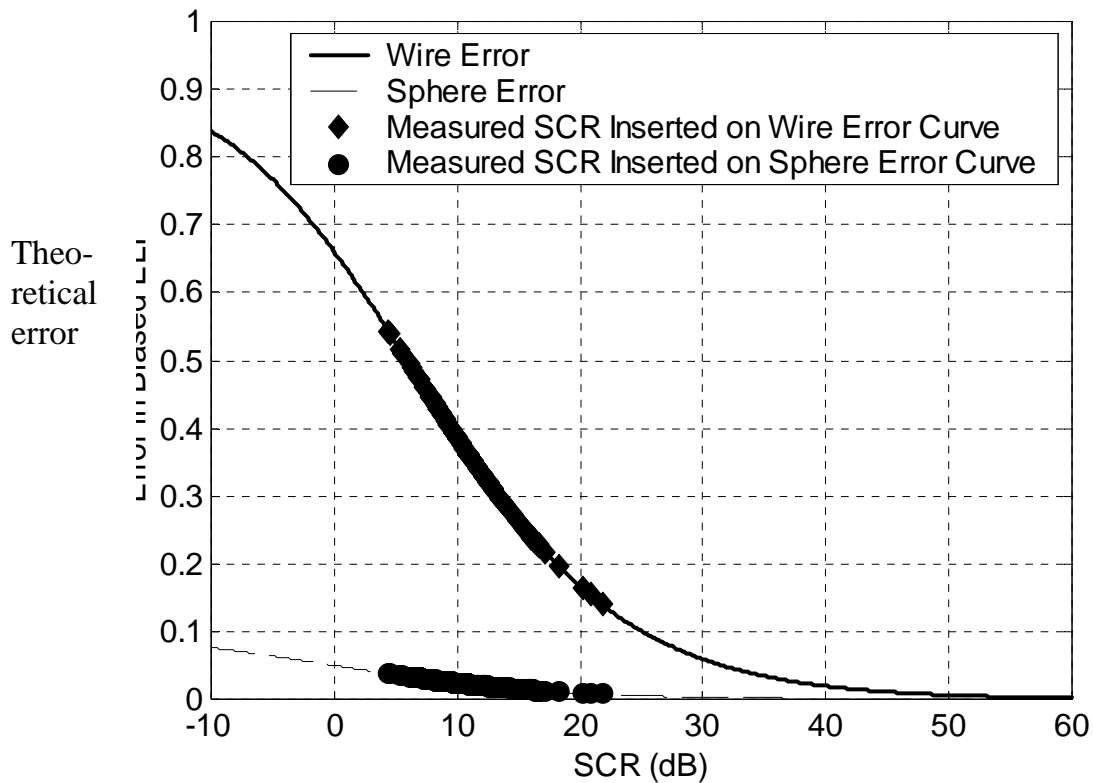
Figure 74 Theoretical error vs SCR for each target in the Tyndall data

A histogram of the measured SCR for the single point measurements at the Tyndall site is shown in Figure 75. It can be seen that a majority of the measured SCR values are grouped around 10 dB, showing a moderately poor SCR level for the entire site. It appears that clutter is a limiting factor for this entire site. The question becomes, "How do we reduce clutter?" One possible answer can be seen in the multi-position measurements taken at Blossom Point.
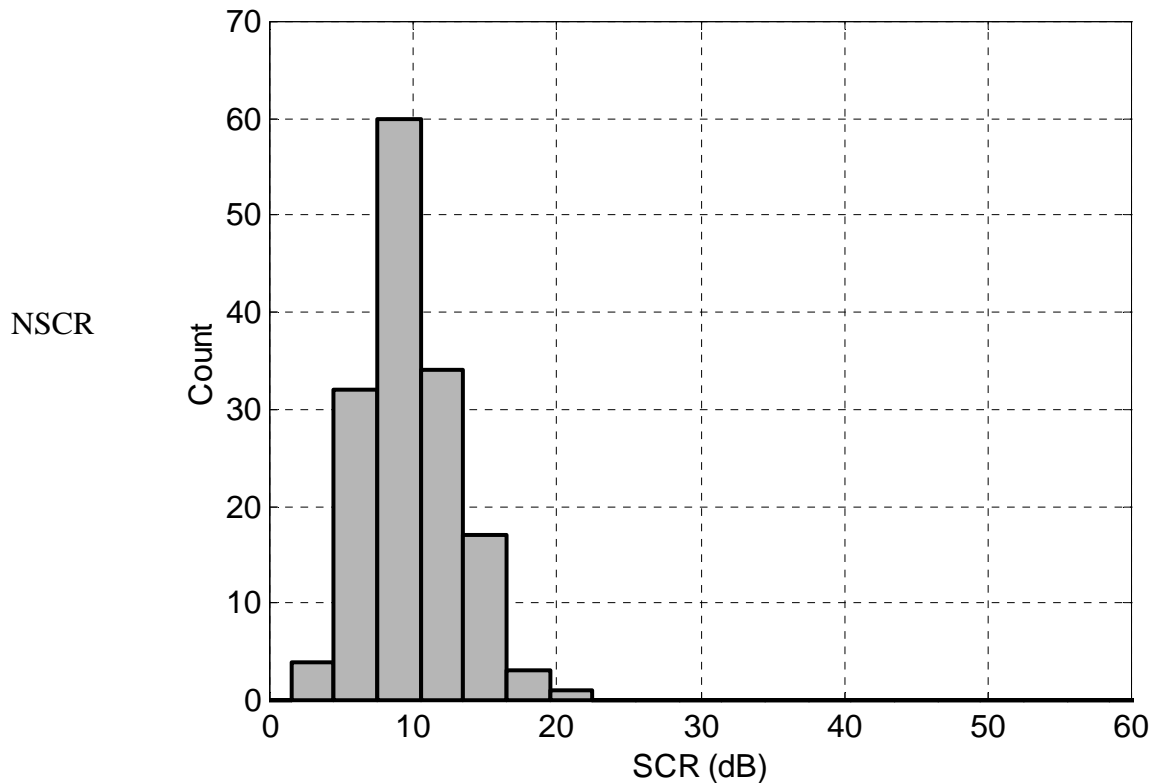
Figure 75. Number of SCR values (NSCR) vs SCR for Tyndall data

In Figure 76 the measured SCR values for the multi-position measurements taken at Blossom Point Proving Grounds are superimposed on the theoretical biased ELF plot. These SCR values were calculated using the same procedure used to calculate the single point SCR from the Tyndall site. The SCR levels for the targets range from -10 to 20 dB. It appears that all of the targets lie below the 20 dB threshold that was discussed previously. This allows an apples-to-apples comparison with the Tyndall data, strongly suggesting that there is an overall lower SCR level for the Blossom Point site. A histogram of the SCR for the Blossom Point site is shown in Figure 77, with SCR values clustered between mainly 0 to 10 dB. It appears that clutter is limiting factor for the entire site.
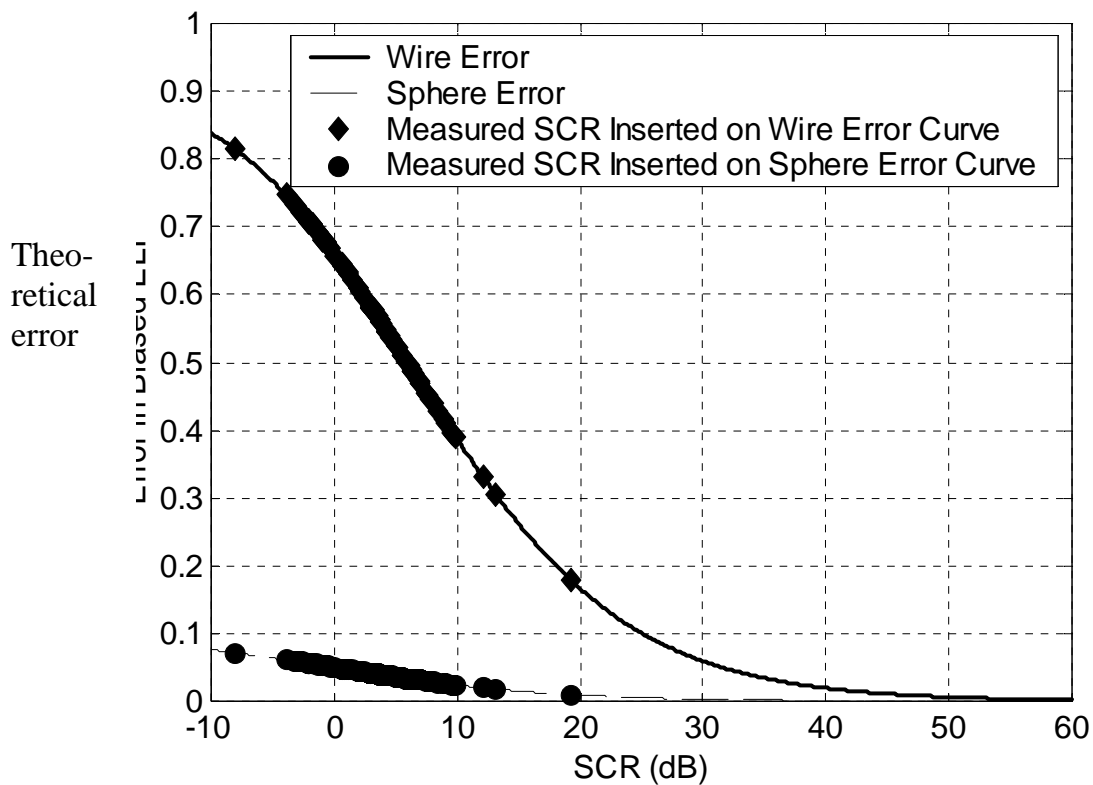
Figure 76 Theoretical error in Blossom Point Data vs SCR values for each target; SCR calculated using same method as at Tyndall for each antenna position.
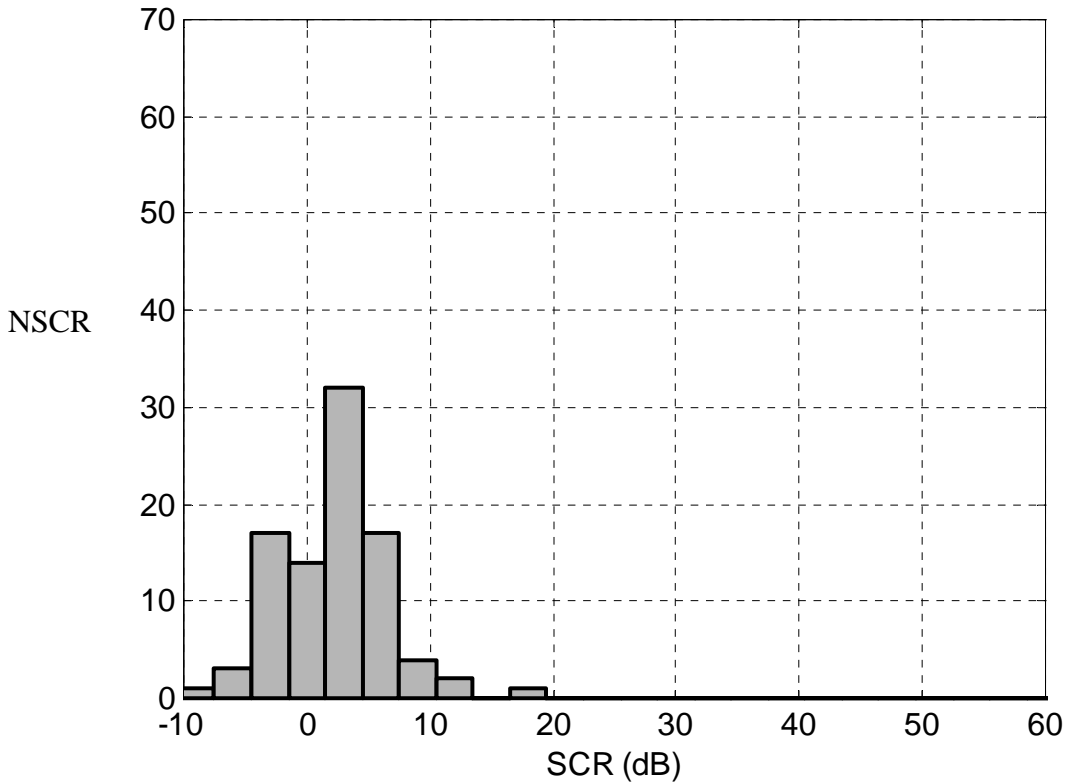
Figure 77 Number of SCR level occurrences (NSCR) for Blossom Point Data, vs SCR, calculated using same method as at Tyndall, for each antenna position.

Now let's look at the measured SCR values, when calculated using the multi-position processing method, for the multi-position measurements taken at Blossom Point. Values are superimposed on the theoretical biased ELF plot in Figure 78. One can see that the SCR levels for the targets range from 5 to 60 dB. It appears that a majority of the targets lie above the 20 dB threshold that was discussed previously. Furthermore, this plot shows that there are several targets with a SCR value less than 20 dB. A histogram of the SCR for the multi-position measurement Blossom Point site is shown in Figure 79. Relative to the distribution in Figure 77 the SCR values are much more evenly distributed, now between about 15 to 55dB. However, there are approximately 19 targets with a SCR levels less than 20 dB. These 19 targets account for 20 percent of the total targets. It appears that clutter is not a limiting factor for the entire site, but it is still a concern. This demonstrates, in part, one of the advantages of multi-position measurements over the single-point measurements. The main difference was the background subtraction. Single point background subtraction is performed by selecting one position as target location and another as background. While multi-position background subtraction uses every position as the target and uses an ensemble average of all the positions as a background.
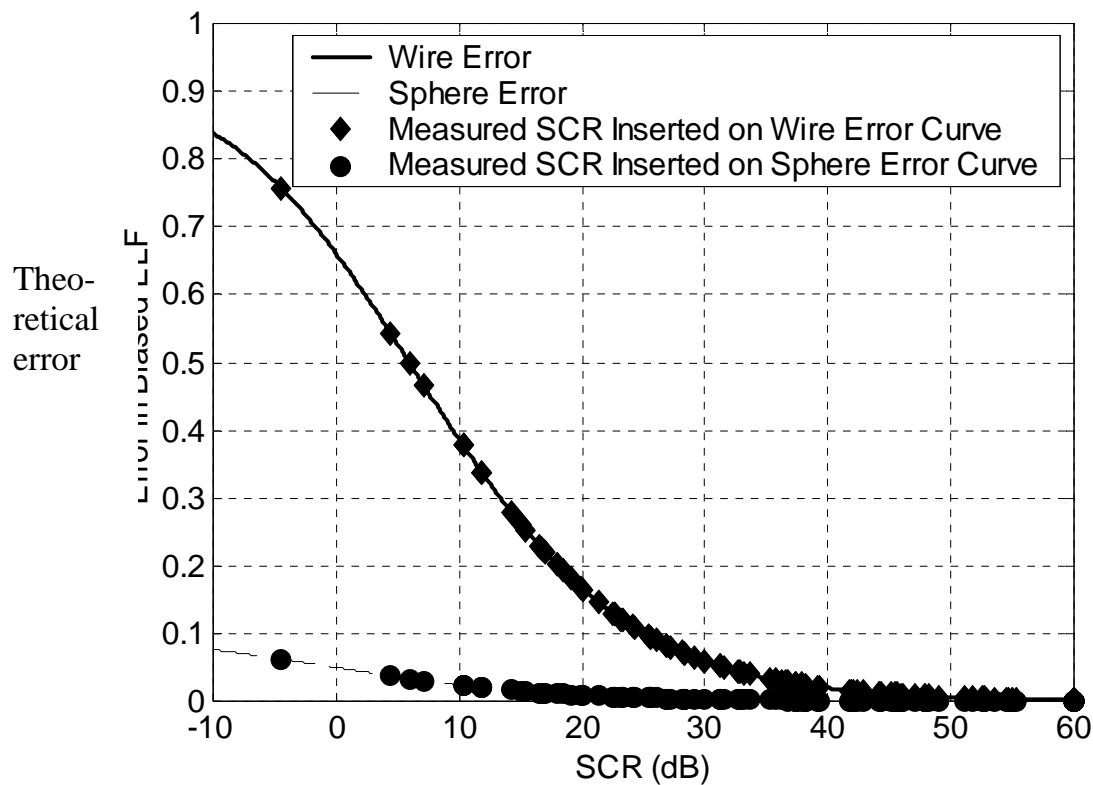
Figure 78 Theoretical error in Blossom Point data vs SCR values for each target.
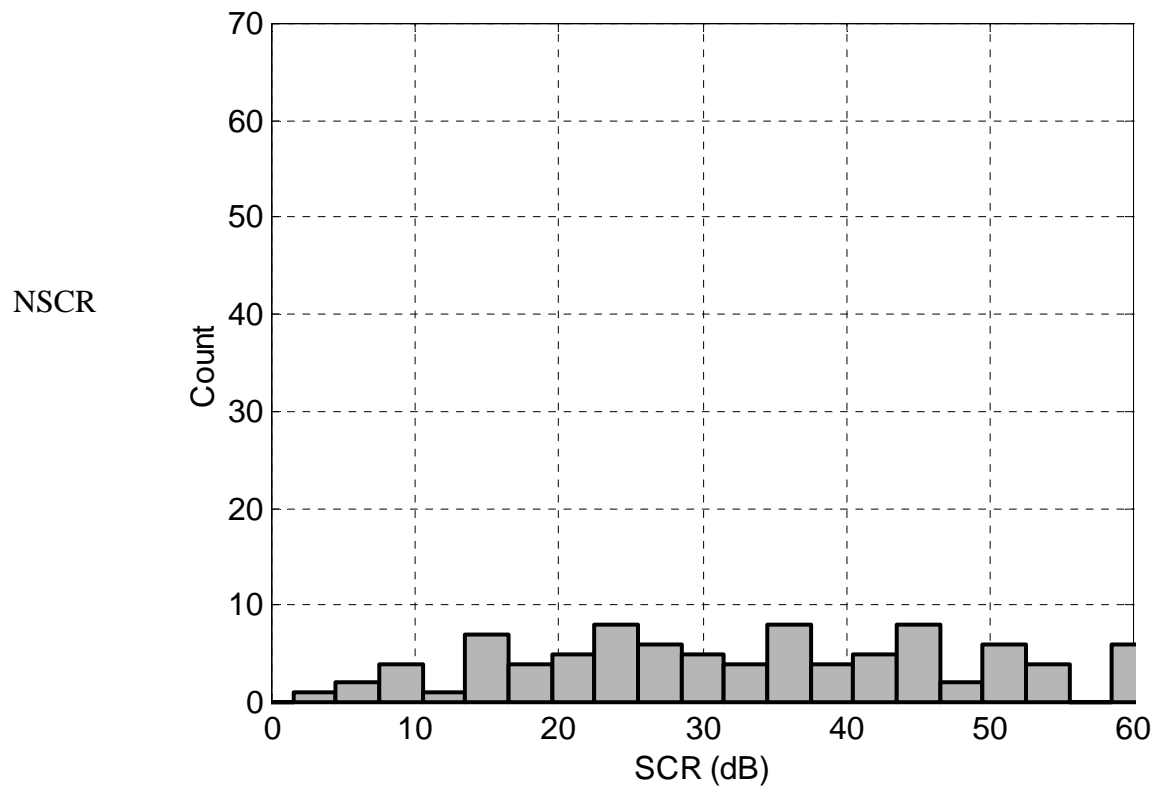
NSCR

Figure 79 Number of occurrence of SCR levels (NSCR) for multi-position treatment of Blossom Point Data.

Chapter 7   Conclusions

The old lanes at the Blossom Point site contain many vertical UXO-like items. This ordnance orientation is in general very difficult for GPR operations. First, a radar directly above the target excites only weak scattering. Although the scattering can be enhanced by offsetting the radar to provide oblique subsurface incidence, a longer propagation path results in more soil absorption. During the Demo I in this project (Tyndall AFB), it was already determined that the classification performance for UXO-like items with large inclination angles was poor. Therefore, the fact that only one vertical ordnance item was missed during the blind test at Blossom Point is indeed a remarkable improvement. Such improvement was achieved for two reasons. First, the comprehensiveness of the target set at Tyndall provided invaluable lessons as far as finding out the sources of missed UXO and false classification. Secondly, based on the Tyndall's findings and the radar knowledge of our team, effective improvements in system configuration, measurement approach, feature extraction algorithms and classification criteria were made before the Demo II at Blossom Point Demo. In part the new approach involved making multiple passes, in different directions, over essentially all targets. Single passes over some targets were associated with poorer performance in the previous demo.

The new multiple-position, multiple pass approach proved to be useful in discriminating UXO-like items from clutter items for ordnance with large inclination angles, by providing spatial variation of target features and temporal-spatial scattering patterns. Canonical scattering-pattern features for conducting spheres, plates and UXO-like items were defined and applied for classification. Some unique site-specific clutter items such as horseshoes and barbed wire bundles also showed interesting linearity and scattering features that are different from a UXO-like item. Classification rules that utilize estimated linear factor (ELF), estimated orientation (ETO) and scattering patterns were developed and refined based on these canonical objects. Currently, the classification procedure was performed by training an operator to recognize visuals in executing the classification rules. While requiring "human

in the loop" processing, the training required is not formidable. Automatic classification can be implemented with further development.

The classification performance on the new lanes at Blossom Point was much poorer than on the old lanes. We conclude that this was related to three facts: (1) Many small items were buried at much greater depth than the similar items buried in the old lanes; (2) The trenches caused by the burial of the targets were more prominent than on the old lanes. There were also visible linear trenches existing in the whole Blossom Point site, perhaps caused by previous burial or extraction of drainage or irrigation system; (3) more inclination variations in the new lanes. Overall, one notes that UXO-like items with a large depression angle ($> 45^{o}$) and depth greater than 0.75 meters showed poor signal to clutter ratio and were much more difficult to classify, under the soil conditions at the site. The combination of weak scattering and greater soil absorption resulted in weaker radar response. The sensitivity of the radar itself is greater than 90 dB and is capable of detecting such weak responses. However the clutter level (approximately 70dB below the input power) resulting from ground scattering (surface & subsurface) is a major limitation. Increasing transmitted power will only increase both the signal and clutter levels and does not improve the SCR. In the very least, it may be advisable in some circumstances to segregate signal regions for processing so that near-surface and deeper reflections are treated separately, each ear-marked so that confidence can be assigned accordingly.

Some possible approaches for improving the SCR include: (1) bistatic measurement configuration that uses separate transmitting and receiving antennas; (2) further clutter reduction using signal processing methods; (3) smart radiation pattern control of the antenna; (4) smoothing the ground surface. The effectiveness of the Approach (1) depends on whether the ground clutter scatters more weakly into the bistatic direction compared to the backscattering direction. This is yet to be evaluated, and may depend on the type of clutter. Similar to the adaptive smoothing algorithm that was developed here to greatly improve the SCR utilizing the different propagation delays between the desired target and undesired clutter sources, other processing algorithms can be developed to utilize other distinguishing features between the target and different types of clutter. A majority of the clutter is caused by ground surface, not only from the spot underneath the antenna but also from spots near the antenna. Current antenna design has a relatively broad radiation pattern in order to have effective illumination at the target from offset positions. This design also makes it vulnerable to the scattering

from the ground surrounding the antenna. A more desirable design is to have a narrow radiation pattern but with controllable beam direction as illustrated in Figure 80. Although this is a very sound design conceptually, it is a big challenge for GPR antenna design due to the frequency range and limited antenna size. A related alternative is to use (perhaps in combination with the system already deployed) a special purpose antenna, with fixed beam orientation but narrower beamwidth and oblique subsurface direction. Development of an antenna with such a design has been proposed for a SERDP project. Approach (4) might seem unrealistic, however at present it may be the most effective way of reducing the surface clutter.

Air

Soil
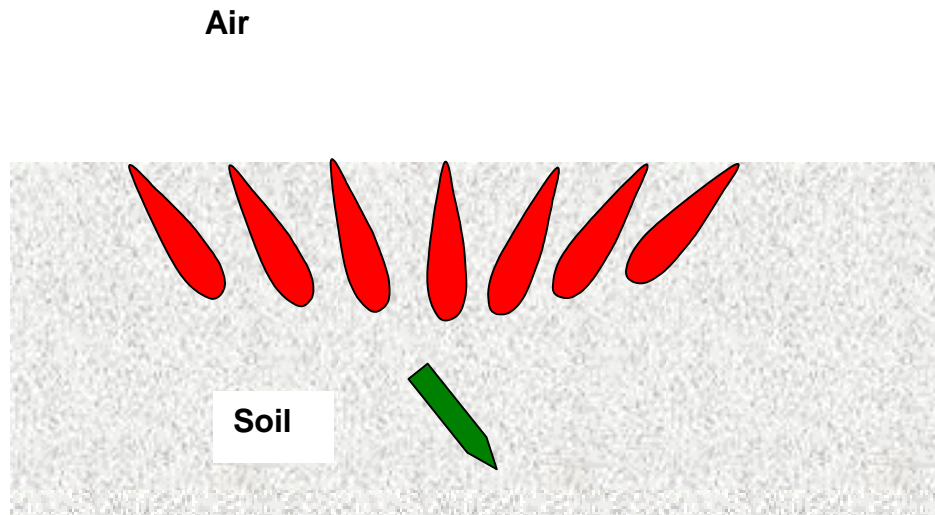
Figure 80   Conceptual smart antenna design with narrow beam patterns (red) and controllable beam direction, shown oriented in selected directions.

The Blossom Point Site data indicated that signals collected from a transverse (second) pass centered at target location were not useful for ordnance with a significant inclination. A more useful transverse pass would be collected from the offset position. Figure 81 and Figure 82 give two examples of buried UXO's that have depression angles of 30 degrees. The data were collected along a UXO direction centered at target locations with the antenna polarized parallel to the UXO's azimuthal angle (horizontal orientation). Both data clearly show the depression angle from the tilted reflection responses that are offset from the center, associated with strong backscatter along the incident angles shown in Figure 83. The previous approach collected the transverse-pass (out of paper) data centered at

the target, i.e. through position 0. As one can see, the responses observed at the center position are actually quite weak. If one selected the center position of the transverse pass based on the parallel-pass data, e.g. the position at 30 inches in Figure 81, then a better responses can be obtained from the transverse pass with a likely improvement in classification capability. This new approach is being tested at the OSU/ESL test field.

Targets contained in Tyndall and Blossom Point sites represent only a small portion of real-world items. Therefore, conducting more measurements at different sites containing different ground conditions, UXO types, and clutter items is very important.   This is underscored by the lessons learned and improvements in survey approach and processing that were developed in response to each of these Demos.
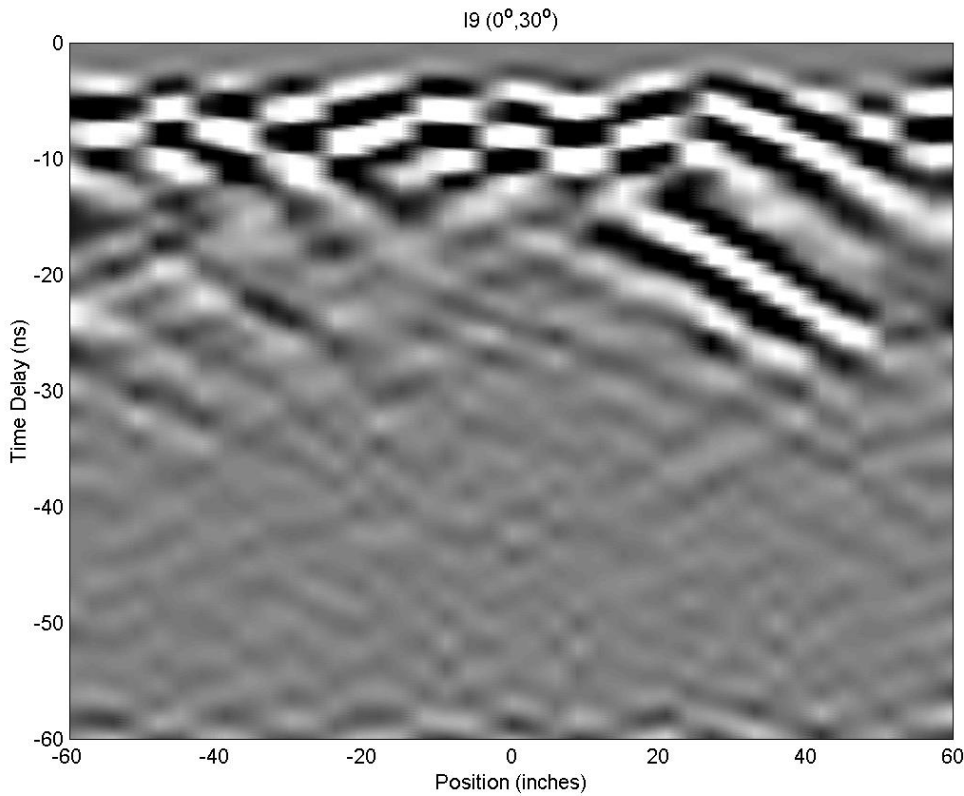
Figure 81   GPR data collected parallel to the UXO (2.75", Position I9) orientation that has a 30-degree depression angle.
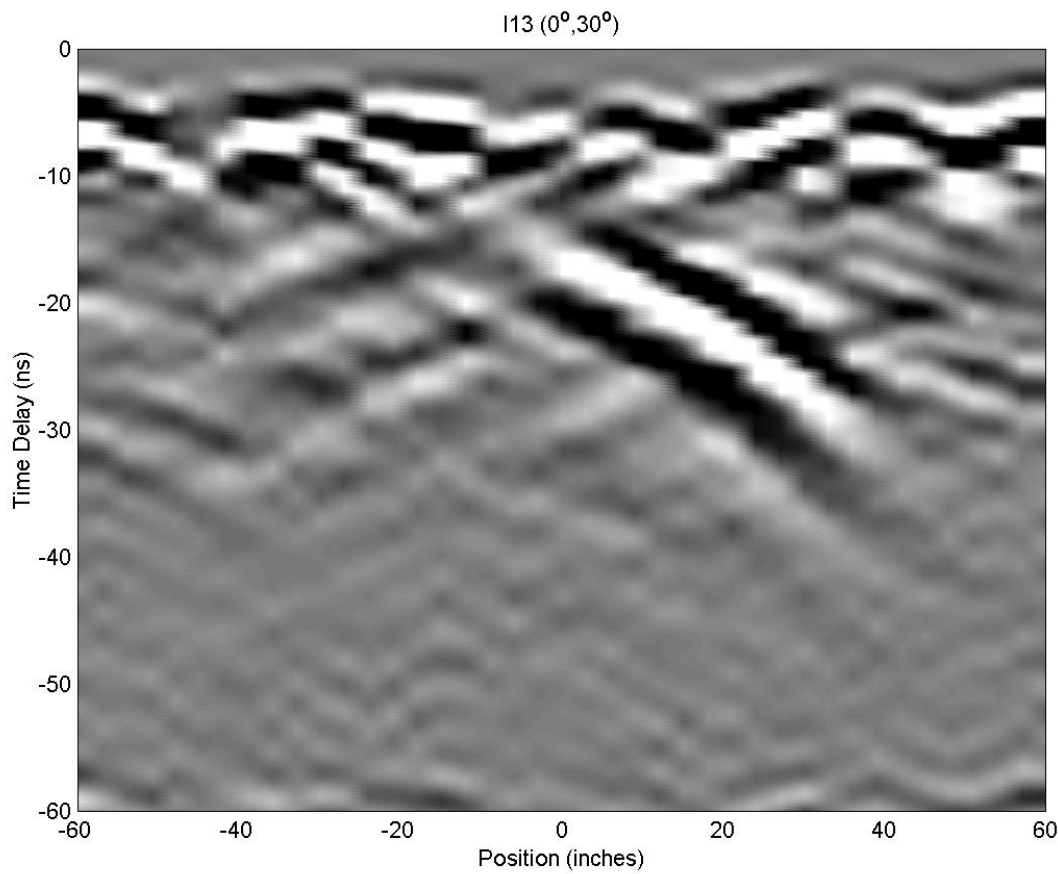
Figure 82 GPR data collected parallel to the UXO (81mm, Position I13) orientation that has a 30-degree depression angle.
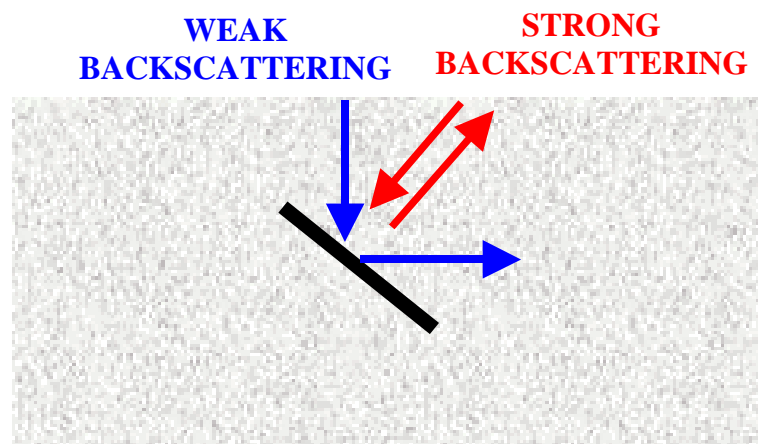
Figure 83   Stronger scattering for a tilted UXO from offset position.

Appendix A   Archiving

All the raw and processed data will be submitted in a self-documented CD-ROM. A couple of MATLAB programs that allow the user to read the data (time and frequency) and view the classification features will also be provided.

A.1 GPR Data Files – *.cdt

The data for system-calibrated frequency-domain radar data was stored in Binary-format files called "**aydddaa.cdt**", where "a" is from A to Z for file ordering.   The letter "y" indicates the last digit of the year. For example, "0" represents the year of 2000.   The three-digit number, "ddd" , indicates the Julian date when the data was stored. Each file contains a two-dimensional data taken at multiple target locations. The first frequency (10 MHz) data was stored in the first row, the second frequency (12 MHz) data was stored in the second row, …, etc. Table 9 illustrates the new format of multiple GPR data. Data collected at each position is contained in one vertical block that is compose of six columns corresponding to the real and imaginary parts of S11, S21 and S22, respectively, as illustrated in Table 10. For each radar file, '*.cdt", there is an associated comment file called "*.txt" to store the system information and comments. There is also an associated processed file called "*.mat" file that stores the processed results and all processing parameters. All of these files will be available in a CD-ROM after this submission of this report.

Table 9 Format for multiple-position GPR data.

Data(f_1,X_1)	Data(f_1,X_2)		Data(f_1,X_n)
Data(f_2,X_1)	Data(f_2,X_2)		Data(f_2,X_n)
Data(f_m,X_1)	Data(f_m,X_2)		Data(f_m,X_n)

An example of data format for Data(f_m,X_n) is shown below.

Table 10 Data format for a single frequency at a single position.

Re(S$_{11}$)	Im(S$_{11}$)	Re(S$_{21}$)	Im(S$_{21}$)	Re(S$_{22}$)	Im(S$_{22}$)

"Re()" and "Im()" indicate the real and imaginary parts, respectively (combined, these provide the amplitude and phase).

A.2 Comment Text Files - *.txt

The comment text files contain information about measurement conditions (i.e. position, direction, etc.) and any comments the user entered during the measurements. For example, the comment file a0348ag.txt is printed below:

Start Time: 511/Stop Time: 519/Target #: A2/Start f: 10/Stop f: 410/Num of Points: 201/Antenna Orientation: 92/Num of Scans: 41/Antenna Position: xstart: -60/delta x: 3/yoffset: 0/Relative Permitivity: 20/User Comments: /$

This is a typical comment file. It contains the time, in minutes from midnight, at which the scan was started and finished. It also contains the information necessary to recreate the frequency vector and the position vector, i.e. number of positions of data taken and the spacing between them.

A.3 Processed Files -*.mat Files

The processed data is saved in *.mat format (a Matlab file format), in which the following variables are saved.

```
Variables of Processed Data Results

ELF  –     Estimated Linear Factor vs. position
fELF –     Frequency Estimated Linear Factor vs. position
melf –     Mean of ELF and fELF
ETO  –     Estimated Target Orientation vs. position
CNR  –     Complex Natural Resonance and Damping vs. position
ETL  –     Estimated Target Length vs. position
Y1a  –     Position vector
SNR  –     Estimated Signal to Noise Ratio vs. position
SCR  –     Estimated Signal to Clutter Ratio vs. position
ATV  –     Antenna Orientation
```

Variables of How Data was Processed

SELECTION –Data Channel used for CNR extraction
ftype –   Type of frequency domain filter
ucfreq2 – User Centered frequency for the adaptive bandpass filter
npoint –   Number of points in the adaptive bandpass filter
nx –   Position vector for late-time region selection
ntmax –   First Time position for late-time region vs. x-position
numTdiff – Number of points in late-time region vs. x-position
T0 –   Variable for slope gain
TM –   Variable for slope gain
gainfac – Variable for slope gain
imgT –   Variable for adaptive smoothing
imgindT - Variable for adaptive smoothing
imgindx - Variable for adaptive smoothing
imgN –   Variable for adaptive smoothing
SIDE -   Variable for adaptive smoothing

Appendix B Electrical Properties of the Blossom

Point Soil

The soil electrical properties, permittivity and conductivity at 40 MHz and 60 MHz, were measured at different depths using the OSU/ESL soil probe as shown in Figure 84

Figure 84 OSU/ESL soil probe for permittivity and conductivity measurement at 40 MHz and 60 MHz.
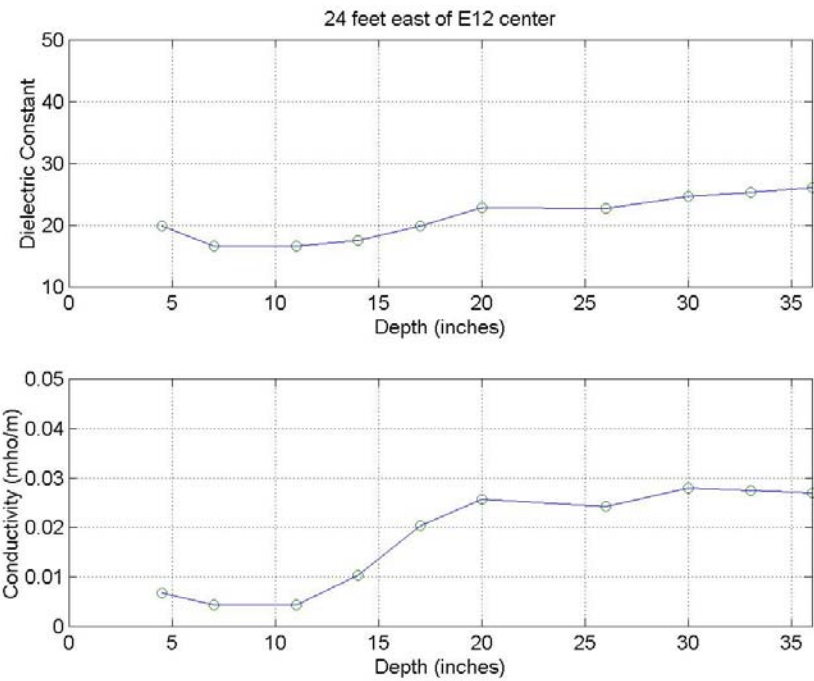
Figure 85 Soil electrical property measured on 12/10/2000 at 40 MHz.
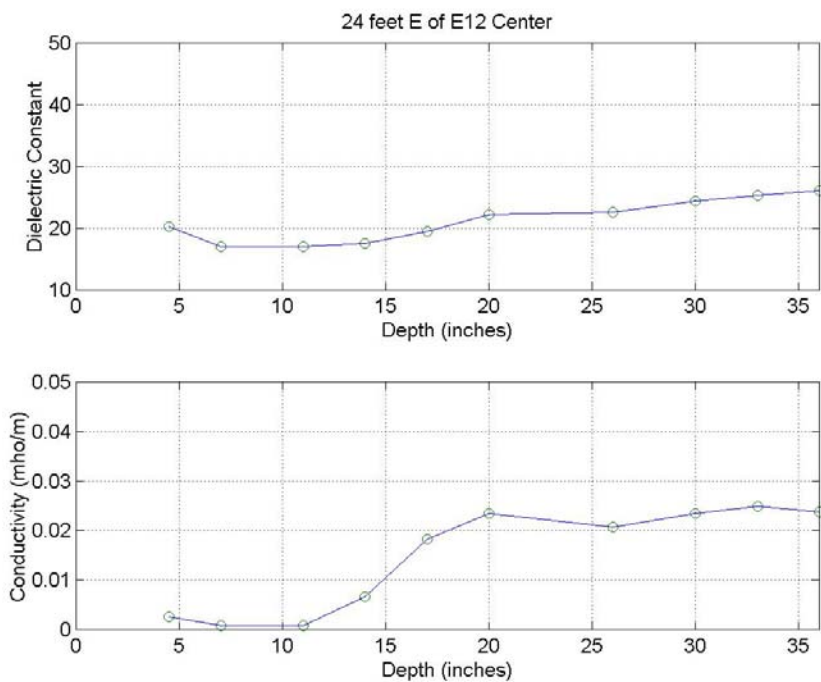
Figure 86 Soil electrical property measured on 12/10/2000 at 60 MHz.
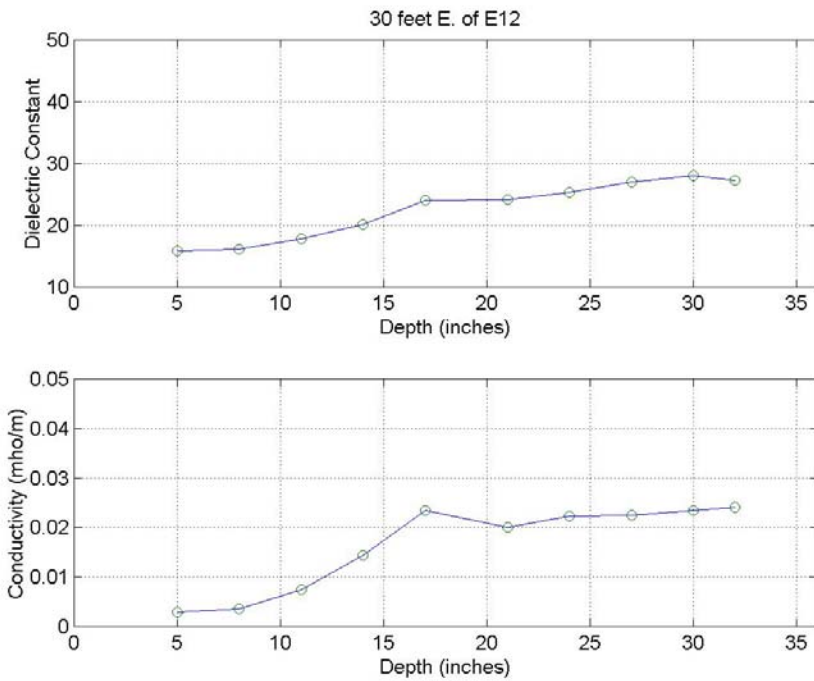
Figure 87 Soil electrical property measured on 12/11/2000 at 40 MHz.
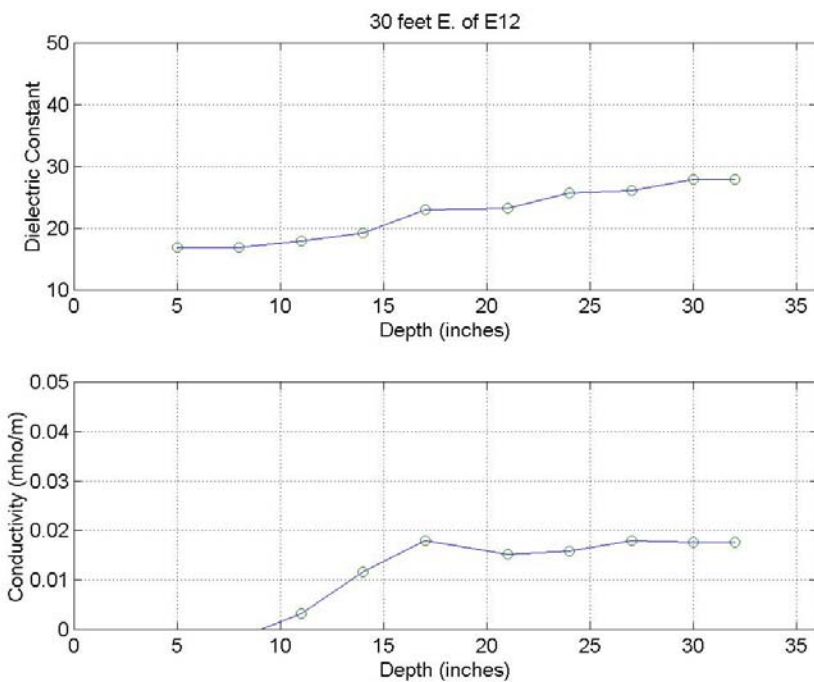
Figure 88 Soil electrical property measured on 12/11/2000 at 60 MHz.
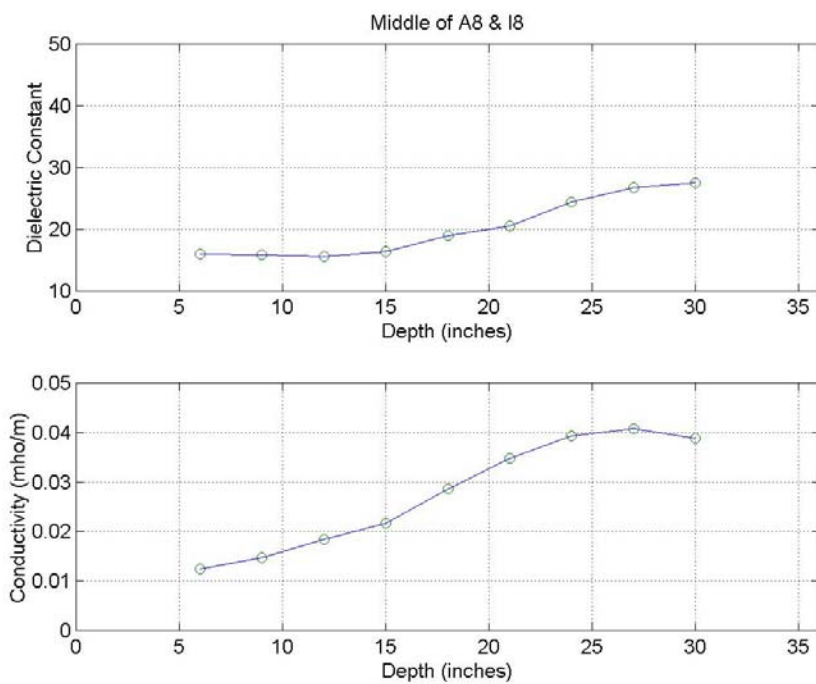
Figure 89 Soil electrical property measured on 12/12/2000 at 40 MHz.
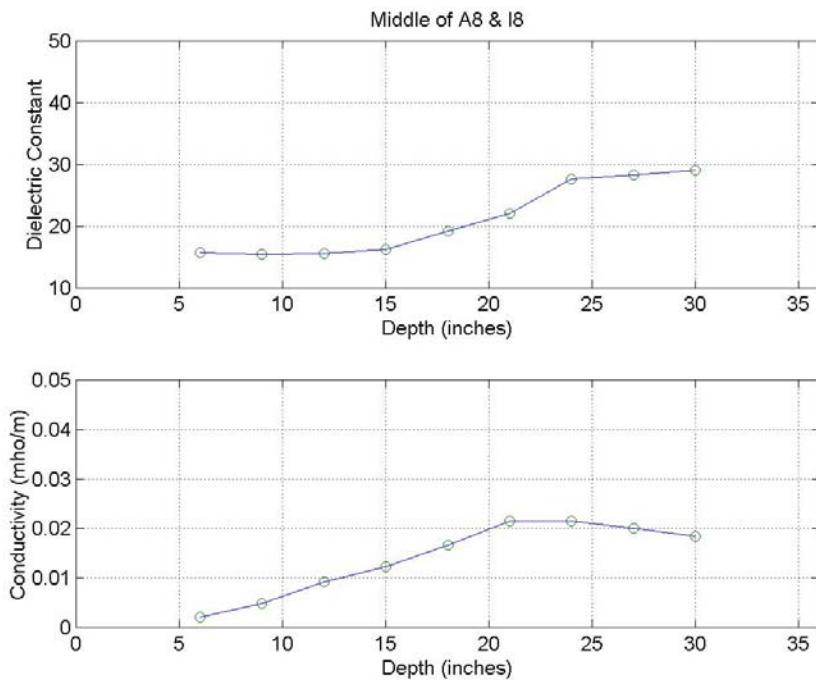
Figure 90   Soil electrical property measured on 12/12/2000 at 60 MHz.

Appendix C BLOSSOM PT DEMO LOG Excerpt

North ↑

BLOSSOM POINT, 12/13-14/2000, SET 1 SCHONSTEDT INFO

|				
15 A - the reference	15 B - dipole N-S	15 C - ~ shallow, dip on re-examination, S	15 D - shallow dip ~ NW - SE	15 E - very shallow
14 A - shallow N-S dip	14 B - shallow	14 C - shallow, N-S dipole	14 D - shallow, symm	14 E - broad, south
13 A - strong	13 B - shallow	13 C - C (missed shallow?)	13 D - C	13 E - X
12 A - very shallow	12 B - dipole, Nal	X	12 D - NR	12 E -shallow dip slight indic of Nal
11 A - strong shallow dip, aligned with marked directions	11 B - shallow, strong dip ~ N-S	11 C - shallow, dip, aligned	11 D - weak, S	11 E - X
X	10 B - shallow N-S dipole	10 C - very shallow	10 D - X	10 E - S/SE
9 A - very shallow	9 B - shallow	9 C - shallow, dip ~ aligned	9 D - C	9 E - shallow
8 A - very shallow	X	8 C - shallow, aligned dipole	8 D - strong, sombrero?	8 E - shallow, slight indic of dip
7 A - C	7 B - shallow	X	7 D - C	7 E - centered
6 A - NR	X	6 C - shallow, some dipole	X	6 E - X
5 A - fairly shallow, S	5 B - a bit shallow, S	X	5 D - shallow	5 E - X
4 A - South	4 B - C	4 C - shallow	4 D - broad	4 E - X
3 A - C	3 B - C	3 C - NR	3 D - broad, south	3 E - NR
2 A - strong dipole in all directions	2 B - shallow, South, slight dipole	2 C - dipole, N-S	2 D - shallow, sombrero	2 E - broad, south
1 A - shallow	X	1 C - weird, heterogeneous, S	1 D - shallow, dip	1 E - shallow, dip

C = centered, azimuthally symmetric, positive;   dip = dipole (sign change)
S, NE etc = south, northeast etc offset   NR = no significant signal
Nal = not aligned with marked principal directions   X = no target
highlight = calibration targets;   NOTE: The flag for 13 A was put on 12 A by mistake for at least part of the time.

110

BLOSSOM POINT, 12/13/2000, SET 4 SCHONSTEDT INFO

North	↑

			15 I - C, broad
			14 I - South
			13 I - a bit shallow, South
		12 H - SE	12 I - C, broad
		11 H - C	11 I - C, broad
		10 H - broad	10 I - C, broad
	9 G - faint	9 H - SW	9 I - C
	8 G - NR	8 H - South	8 I - NR
7 F - C	7 G - C	7 H - C	7 I - NR
6 F - C	6 G - broad, faint	6 H - South	6 I - NR
5 F - NR	5 G - moderately broad	5 H - shallow, NE	5 I - NR
	4 G - NR	4 H - South	4 I - C

C = centered, azimuthally symmetric, positive;
dip = dipole pattern (sign change)
S, NE etc = signal center offset south, northeast etc
NR = no significant signal
Nal = not aligned with marked principal directions
blank cell = no target

Appendix B: Ground Truth Data

The following information about the ground truth data for the Blossom Point site was provided by NRL after the submission of the processing results to ESTCP. Figure 91 shows the location designation of the targets buried at the Blossom Point site. Only the targets buried in lanes from A thru I were measured by CRREL/OSU team. The new GPR targets were buried in lanes from F to I. The ground truth of these targets are shown by the target ID shown in Table 11 and Figure 92.

	F	G	H	I		K	L	M		A	B	C	D	E
13				15 I						15 A	15 B	15 C	15 D	15 E
14				14 I						14 A	14 B	14 C	14 D	14 E
13				13 I						13 A	13 B	13 C	13 D	
12			12 H	12 I				12 M		12 A	12 B		12 D	12 E
11			11 H	11 I				11 M		11 A	11 B	11 C	11 D	
10			10 H	10 I				10 M			10 B	10 C		10 E
9		9 G	9 H	9 I				9 M		9 A	9 B	9 C	9 D	9 E
8		8 G	8 H	8 I		8K	8 L	8 M		8 A		8 C	8 D	8 E
7	7 F	7 G	7 H	7 I		7 K	7 L	7 M		7 A	7 B		7 D	7 E
6	6 F	6 G	6 H	6 I		6 K	6 L	6 M		6 A		6 C		
5	5 F	5 G	5 H	5 I		5 K	5 L	5 M		5 A	5 B		5 D	
4		4 G	4 H	4 I			4 L	4 M		4 A	4 B	4 C	4 D	
3								3 M		3 A	3 B	3 C	3 D	3 E
2								2 M		2 A	2 B	2 C	2 D	2 E
1								1 M		1 A		1 C	1 D	1 E
	F	G	H	I						A	B	C	D	E

Figure 91 Location designation of the Blossom Point site. Only lanes A~I were measured by OSU/ESL GPR.

Table 11 The target ID (Ground Truth) of the targets buried in Lanes A~E.

	A	B	C	D	E
15	G010250	L010250	B010200	A010050	K010080
14	H010052	M01025	J010252	C010350	F010750
13	P010750	D010100	E010500	N010350	
12	B020100	L020150		Q070100	K020050
11	Q040030	D040100	Q090100	F021000	
10		M02025	H020050		L030154
9	J020250	E020350	Q120050	D020250	Q060050
8	A020100		K030054	Q100150	Q150080
7	C030500	F030750		L040250	D030250
6	Q030030		B030100		
5	C030350	Q140230		M03015	
4	N040500	E030350	B040200	F041000	
3	C040500	N030500	Q010050	L050254	Q020050
2	Q080230	M04015	Q110100	L060150	P020750
1	N040350		E040500	Q050100	Q130150
	A	**B**	**C**	**D**	**E**

Item Designations are of the form AxxDDDAI where A = Item Designator, xx = Serial Number, DDD = depth in cm, A = azimuth in 1/16 of a circle (0 = 0 deg , 2 = 45 deg, etc.), and I = inclination in the same units (0 = parallel to the surface, 4 = 90 deg nose down, etc.)

GPR Targets
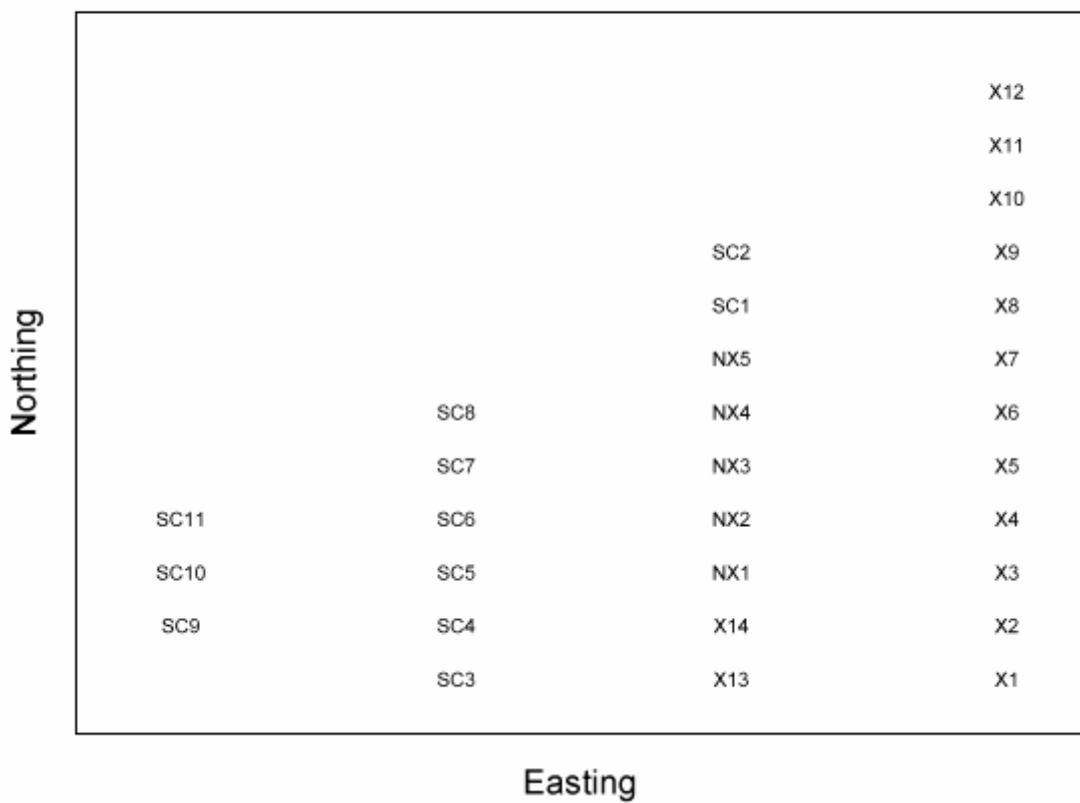
Figure 92 Target ID of the new GPR targets buried in lanes F~I.

Table 12 Description of the targets buried in lanes A~E.

I	Descript.	I	Descript.	I	Descript.	I	Descript	I	Descript.
A	1½"x3" steel	B	1½"x6" steel	C	1½"x12" steel	D	3"x6" steel	E	3"x12" steel
F	3"x24" steel	G	16 lb shotput	H	4"x4"x¼" steel plate	J	8"x8"x¼" steel	K	1½"x6"x¼" steel
L	3"x12"x¼" steel plate	M	Mk 23	N	81-mm mortar	P	BDU-33	Q	Clutter
R	60-mm mortar	S	20-mm	T	30-mm	U	50-cal		

114

Table 13 Description of target buried in lanes F~I.

ID #	Item	Depth	Azimuth	Inclination
X1	60mm	0.25	0	0
X2	60mm	.5	45	30
X3	60mm	.75	90	30
X4	60mm	.75	90	45
X5	60mm	1	0	90
X6	2.75"	.25	0	30
X7	2.75"	.5	0	45
X8	2.75"	.5	90	60
X9	2.75"	.75	45	75
X10	81mm	.25	0	30
X11	81mm	.5	45	45
X12	81mm	.75	90	60
X13	BDU-33	1	45	30
X14	120mm	1	45	60
NX1	Steel Bar L24"/D3"	.75	0	30
NX2	Steel Bar	.75	90	45
NX3	8"d steel plate	.3	Arbitrary	0^3
NX4	8"d steel plate	.5	Arbitrary	45^3
NX5	8"d steel plate	.75	Arbitrary	90^4
Sc1	Whole crumpled box fin	.25	Arbitrary	Arbitrary
Sc2	box fin fragment	.5	0	0
Sc3	Projectile nose	.75	0	$0^{1,3}$
Sc4	Cluster of clutter items 25,17, &12	$.5^2$	0,120,240	45^3
Sc5	clutter Item #22	.75	0	$30^{1,3}$
Sc6	clutter Item #3	.5	0	90^3
Sc7	clutter Item #24	.75	45	$30^{1,3}$
Sc8	clutter Item #18	.5	90	0
Sc9	clutter Item #23	.75	90	$0^{3,5}$
Sc10	clutter Item #11	.5	45	60^4
Sc11	clutter Item #16	.5	45	45^4

1. Curved side down
2. Depth .5 m to upper tip of each item, tips not touching
3. No twist about axis after inclination
4. 45 deg twist after inclination
5. Curved side up

Bibliography

[1] M.B. Higgins, C-C. Chen, K. O'Neill and R. Detsch, "Tyndall AFB Measurement Results of UXO Characterization Using Full-Polarimetric, UWB GPR", *USA UXO/Countermine Forum*, May, 2000.

[2] C-C. Chen, M.B. Higgins, K. O'Neill and R. Detsch, "UWB Fully-polarimetric GPR Classification of Subsurface Unexploded Ordnance", accepted for publication, *IEEE Transactions on Geoscience and Remote Sensing*.

[3] H.H. Nelson, J.R. McDonald and R. Robertson, "Design and Construction of the NRL Baseline Ordnance Classification Test Site at Blossom Point," Naval Research Laboratory Report NRL/MR/6110—00-8437, March 20, 2000.

[4] M.B. Higgins, C.-C. Chen and K. O'Neill, "Demo II ESTCP Technology Demonstration Plan - Application of Fully Polarimetric Ground Penetrating Radar for Subsurface UXO Classification: Blossom Point Test Site", November 17, 2000.